Waves in disordered and nonlinear mechanical structures

Arnold Ngapasare

DOCTORAT BRETAGNE LOIRE SCIENCES POUR L'INGENIEUR

Le Mans Université

THÈSE DE DOCTORAT DE

LE MANS UNIVERSITÉ

ÉCOLE DOCTORALE N° 602
Sciences pour l'Ingénieur
Spécialité : *Acoustique*

Par
Arnold NGAPASARE

Waves in disordered and nonlinear mechanical structures

Thèse présentée et soutenue à Le Mans Université, le 17 décembre 2020
Unité de recherche : Laboratoire d'Acoustique de l'Université du Mans - UMR CNRS 6613
Thèse N° : 2020LEMA1036

Rapporteurs avant soutenance :

Mme. Vanessa MAGNANIMO	Associate Professor, University of Twente
M. Victor SÁNCHEZ-MORCILLO	Professeur, Universitat Politècnica de València

Composition du Jury :

Président :	M. Christophe JOSSERAND	Directeur de Recherche CNRS, École Polytechnique (Palaiseau)
Examinateurs :	M. Panayotis G. KEVREKIDIS	Professor, University of Massachusetts, Amherst
	M. Charalampos (Haris) SKOKOS	Associate Professor, University of Cape Town
Dir. de thèse :	M. Olivier RICHOUX	Professeur, Le Mans Université
Co-dir. de thèse :	M. Vassos ACHILLEOS	Chargé de recherche, CNRS, Le Mans Université
Co-enc. de thèse :	M. Georgios THEOCHARIS	Chargé de recherche, CNRS, Le Mans Université

To Mukundi

Acknowledgements

First and foremost, I would like to thank my advisors, Dr. Vassos Achilleos, Prof. Olivier Richoux, Dr. Georgios Theocharis and Prof. Charalampos Skokos all of whom whose guidance has been very much invaluable ; their patience and diligence is very much appreciated. I would also like to acknowledge LAUM (Laboratoire Acoustique de l'Université du Mans) for giving me this opportunity to pursue and work on my PhD thesis.

To the Nonlinear Dynamics and Chaos group members in South Africa, Bob, Many, Malcolm and Henok, I would like to thank you for all the useful discussions and ideas you always bring to the group. You have been great colleagues and teammates.

At LAUM, France, interactions with colleagues like both past and present such as Florian, Elie, Matthieu, Sobin, Xin-Xin, Li-Yang, Rajesh, Théo Thréard, Théo Cavalieri, Pierric, Long, Giannis and many others have been very inspiring.

I would also like to acknowledge the Centre for High Performance Computing (`https://chpc.ac.za`), South Africa, for providing computational resources to significant parts of this thesis as well as their user support engineers. Special mention goes to Kevin and Sean for the very useful ideas and suggestions.

I would like to thank immensely members of my PhD jury for sparing their time and agreeing to be part of my PhD journey. A special thank you goes to Prof. Vanessa Magnanimo and Prof. Victor Sanchez-Marcillo for reviewing my thesis and offering some valuable comments and insights. To Prof. Christophé Josserand and Prof. Panoyotis Kevrekidis, I truly appreciate and acknowledge the roles you played being my jury president and one of the examiners respectively.

Finally, last but certainly not the least, I would like to thank my brother, Albert, and sister, Melody, for the encouragement and moral support.

Contents

List of Figures

Chapter 1
General Introduction

1.1 Motivation

The phenomenon of exponential localization of waves due to heterogeneity (disorder), known as Anderson localization (AL) [1] have remained to be one of the foremost fundamental physical problems still at the frontiers of research. After the initial work of P.W Anderson, AL now encompasses a diverse spectrum of theoretical, experimental and numerical studies in many different contexts ranging from metal-insulator transitions to ultracold atoms to optical fiber arrays [2, 3, 4].

In addition, the effect of *nonlinearity* on AL is a subject that triggered a large amount of theoretical, computational and experimental studies [5, 6, 7, 8, 9, 10, 11, 12, 13], especially following the work of Lahini [14] in 2008, and controversial results were initially reported (see for example [15, 12, 14]). The controversy at that time revolved around the actual role played by nonlinearity; whether it enhances or destroys localization in the presence of disorder. It is now established that for typical nonlinear lattices such as the Klein-Gordon (KG) and the discrete nonlinear Schröedinger equation (DNLS), nonlinearity may destroy the localization of wave-packets due to non integrability and deterministic chaos. The experimental verification of the effects of nonlinearity on AL poses a challenging task, and for such studies one would desire an experimental setting which allows good control of both the nonlinearity and the disorder. Having the latter properties in mind, two particular mechanical systems appear to be excellent candi-

Fig. 1.1. A chain of (i) steel beads on a rubber substrate after [16] and (ii) flexible deformable structures made from LEGO bricks after [17].

dates for studying elastic nonlinear waves with disorder: (i) the granular crystals and (ii) highly deformable architected elastic metamaterials, both shown in Fig. 1.1. Both systems allow the tunability of nonlinearity and a variety of ways to introduce disorder. In the last few years, experiments performed on both aforementioned systems have shown that measurements can be very accurate and the wave propagation in these systems can be well characterized. The subject of this thesis is highly motivated by these two structures and we aim to study theoretically and numerically the interplay between nonlinearity and disorder in these elastic structures.

More importantly, mechanical lattices, such as those studied in this work, feature another characteristic which we wish to exploit in this thesis: rotations are coexisting with displacements. This is expected to lead to much richer dynamics and furthermore, the study of nonlinearity and disorder in systems with two degrees of freedom per site is missing from the current literature to the best of our knowledge.

1.2 Overview and state of the art

Anderson Localization

In 1958, P. W. Anderson published a seminal paper on the localization of waves due heterogeneity in electronic systems [1]. In fact, the work of Anderson was so ground breaking that he was awarded the Nobel prize for physics in 1977. Although, for electrons, disorder appears as on-site potential energy term (or diagonal disorder in matrix notation), many different variations have since being studied. For example, in mechanical lattices, disorder appears either due to geometrical characteristics or to different material properties and can be both diagonal and off-diagonal. From a general sense, disorder in lattices is usually classified as uncorrelated (as in the original Anderson model) or correlated.

Over the years, researchers have proved the theory of AL indirectly by various experiments. However, direct observation involving material particles such as electrons and atoms remained a difficult challenge. The major challenge was on how to deal with the thermally excited phonons and the unavoidable wave interactions. Light or microwaves proved to be a viable alternative as these interactions are very negligible. The first direct evidence results therefore came from light [18] and optical waves have been since then used to demonstrate AL by several researchers (see e.g., [19, 14]). An example of experimental results is shown in panel (i) of Fig. 1.2 where an extended mode of the homogeneous case is contrasted with a localized Anderson mode due to disorder. The direct observation of AL with material particles was also made using Bose-Einstein Condensates (BECs) trapped in optical potentials [20, 21, 22, 23, 24, 25]. As an example, a BEC localized in the center due to disorder is shown in panel (ii) of Fig. 1.2. More relevant to mechanical systems, in panel (iii) of Fig. 1.2, we show the experimental set-up and results of Ref. [26] in which a three-dimensional elastic network was used to show AL of ultrasound waves. It is important to note that Anderson localization continues to be a very active field of research. Furthermore, following a novel study

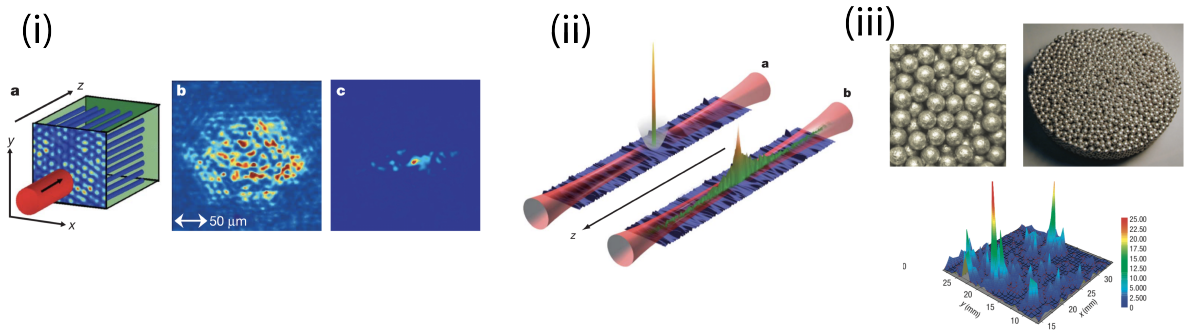

Fig. 1.2. Direct experimental observation of Anderson localization in: (i) a perturbed optical lattice [14], (ii) in a Bose-Einstein condensate [22] and (iii) glued granular aluminum beads [26].

on the so-called localization landscape [27], much interest in AL has been reignited with activities such as a huge collaboration between mathematicians and physicists formed in 2018 by Simons Collaborations in Mathematics and the Physical Sciences to investigate AL (https://cse.umn.edu/wave) taking place.

Nonlinear lattices - The FPUT model

In the 1950s, motivated by the desire to understand the thermalization process of crystals, Enrico Fermi and his team of researchers composed of John Pasta, Stanislaw Ulam and Mary Tsingou (FPUT) [28] set up a numerical experiment using the newly acquired "Maniac" computer at Los Alamos national laboratory in the United States of America. Fermi and his team decided to study how a crystal evolves towards thermal equilibrium by simulating a chain of particles of unitary mass, linked by a quadratic interaction potential, and including a weak *nonlinear* interaction.

Fermi *et al* considered the model now known as the α-FPUT model which is given by the Hamiltonian

$$H = \sum_{n=1}^{N} \frac{p_n^2}{2} + \frac{1}{2}(u_{n+1} - u_n)^2 + \frac{\alpha}{3}(u_{n+1} - u_n)^3, \tag{1.1}$$

where u_n and p_n is the displacement of the nth mass particle with respect to its equilibrium position along the chain and momentum respectively. The stiffness of the harmonic spring and the lattice constant were set to unity, without losing generality. The coefficient $\alpha \ll 1$ measures the strength of the nonlinear contribution to the interaction potential. The two ends of the chain were immobilized and thus $u_0 = u_{N+1} = 0$. Fermi and co-workers had conjectured that due to the nonlinear term, if the initial condition is a single mode, the total energy should slowly drift to the other modes until the equipartition of energy as predicted by statistical physics is achieved. The initial calculations suggested that this would be the case as the next successive modes (i.e., modes $2, 3, \ldots$) were excited. By oversight, their system was left to run long after the steady state had been reached and they discovered that the system had departed from the steady state. This result shocked the quartet as it was beyond their

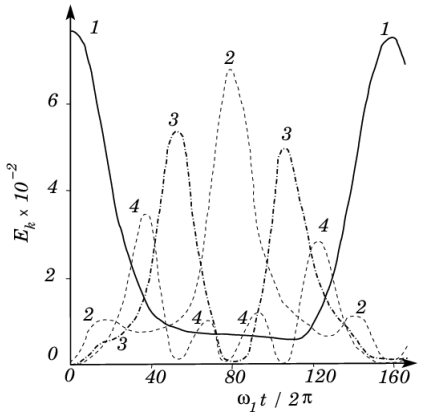

Fig. 1.3. FPUT recurrence: the plot shows the time evolution of the energy of each of the four lowest modes. Initially, only mode 1 was excited (from reference [28]).

wildest expectations and comprehensions. In particular, they observed the energies of the normal modes and their time averages. Fermi and co-workers considered initial data with all the energy in the first Fourier mode and observed that (see Fig. 1.3); (i) the harmonic energies seem to have a recurrent behavior (ii) the time averages of the harmonic energies quickly relaxes to a distribution which is exponentially decreasing with the wave number (FPUT packet of modes). This was quite surprising since, from the principles of statistical mechanics, the solution was expected to explore the whole phase space and the energies of the normal modes were expected to relax to equipartition.

This result became known as the FPUT paradox among scientists. Studies to understand this phenomenon where numerous and more importantly, they signaled the beginning of the nonlinear dynamical systems research as well as the now well established branch of computational physics. Interestingly, only very recently in the work of Onorato and co-workers [29] in 2015, it was shown that the FPUT lattice, as was initially studied, will eventually go to equilibrium after very long integration times, not possible at the period of the original paper. In fact, it appears that mode mixing, and thus the exchange of energy between more and more modes, for the chain of 32 or 64 particles, only appears between six-wave interaction resonances which are of strength of the order of $1/\alpha^4$ and thus very weak. These recent results motivated a part of this PhD thesis which focuses on the equipartition of energy in the presence of disorder and nonlinearity.

Interplay between disorder and nonlinearity

Mathematically, as also shown by the initial work of [28], nonlinearity couples the different linear modes. However, in some cases, nonlinearity seemed to suggest an enhancement of AL [14]. The theoretical explanations of these two seemly contrasting views became a hot topic among scientists. In order to address these controversies, fundamental lattice models such as the discrete KG lattice model and the DNLS were

the main test beds for both theoretical and computational studies. A flurry of theoretical studies followed around the year 2008 which also turned out to be controversial. For example, [15, 30] suggested that weak nonlinearities cause delocalization whilst [31] concluded that there is an absence of wave-packet diffusion due to nonlinearities. A much clearer picture began to emerge afterwards as more and more researchers began to understand the problem better.

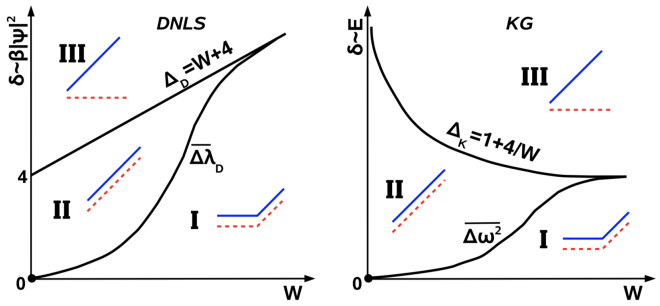

Fig. 1.4. A sketch taken from Ref. [32] indicating the three different energy spreading regimes for the DNLS equation and the KG model.

The initial attempt to explain the universal spreading of wave-packets in disordered nonlinear systems was made in [33] and they concluded that indeed nonlinearity caused spreading. They also discussed the three possible evolution outcomes due to frequency shifts which emerge as a consequence of nonlinearity separated in three regions;

I - localization and similar to linear dynamics,

II - transient localization followed by subdiffusion,

III - self-trapping of a part of the wave-packet and subdiffusion of the rest.

These regions are shown in Fig. 1.4 for both the DNLS equation and the KG model as a function of the disorder strength and the nonlinearity strength (quantified by the frequency shift). In addition, the subdiffussive spreading was attributed to weak chaos in the interior of the wave-packets, and the second moment of the energy distribution was found to grow as $t^{1/3}$.

Skokos and co-workers later followed up on these studies and focused on the chaotic nature of the wave-packet spreading in disordered nonlinear lattices [34] and investigated the chaotic behavior of wave-packets during time evolution (see Fig. 1.5). In their work, they quantitatively studied spreading of wave-packets in disordered lattices and found that chaos plays an important role. Most importantly, although it was believed that when energy is spreading to more degrees of freedom (and thus the oscillation amplitudes are falling), the system will eventually behavior like a linear system (no chaos). However it was shown that it is not the true at least for the KG and DNLS lattices.

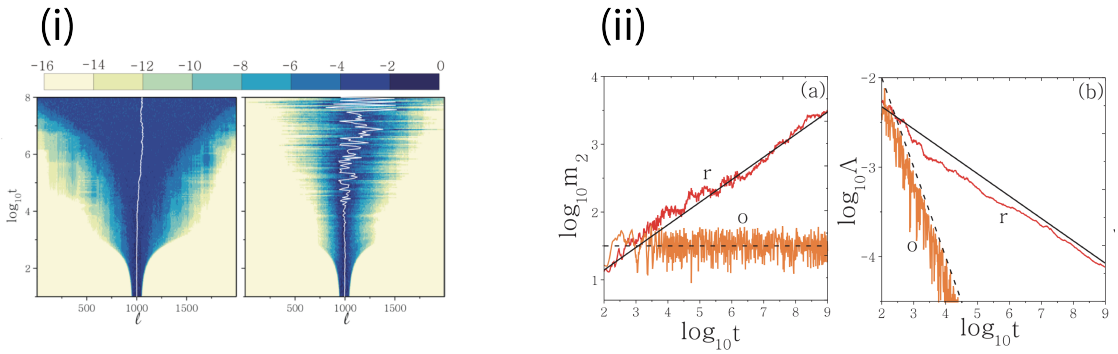

Fig. 1.5. (i) Spatiotemporal evolution of the energy for the KG lattice in the presence of disorder and the corresponding deviation vectors. The wave-packet spreads due to deterministic chaos. (ii) The second moment of energy and the maximum Lyapunov exponent indicating the correlation between energy spreading and chaoticity. Figures are taken from [34].

In particular, the spreading was described as a two stage process which first involves thermalization of the wave-packet then followed by chaotic subdiffusive spreading. Although the chaos was slowing down over time, it did not cross over into regular dynamics. The onset of spreading also triggered the falling of the maximum Lyapunov exponent (mLE) due to the decrease in the energy density as the energy spreads although it did not cross over to regular dynamics.

A few nonlinear resonances which randomly appear during wave-packet spreading were found to be the cause of wave-packet thermalization. All these results pointed to deterministic chaos and dephasing as the two mains ingredients necessary for nonlinear wave-packet spreading in random potentials. A quantitative description of how spreading takes place in the strong chaos regime was later made in [35]. Another issue that arose during these studies is whether wave-packet spreading in disordered lattices slows down or stops, since the sites are excited with less and less energy but this was addressed [36] showing that spreading persists.

However, several questions remain open to date and some of the questions we try to assess in this work:

- What are the transport characteristics of wave-packets in different disordered lattices?
- What is the influence of additional degrees of freedom on the interplay between nonlinearity and disorder?

Elastic classical mechanical lattices

Here we give some more details regarding the two physical systems to be studied in this thesis.

Granular chains

Over the last decade, there has been a growing interest in investigating the propagation of elastic/acoustic waves in phononic crystals. Among the systems that have have attracted a lot of research attention are granular crystals. Granular crystals are periodic arrangements of elastic particles in contact such as rice grains or sand. In the simplest scenario, one models only the force at the contacts between the particles. Due to the fact that this force depends on the contact angle, the geometry or a pre-compression force between particles, such structures exhibit a remarkable tunability of the nonlinearity. Among other things, granular chains are ideal for fundamental nonlinear studies and nowadays the experimental methods to study such systems are well established. Note that during the implementation of this thesis, in Ref. [37] granular structures were experimentally studied with disorder for the first time from a purely one-dimensional perspective.

The effect of central forces in mass-spring systems [38, 39, 40, 41] is not dominant in granular crystals where the transverse rigidity of the contacts are non-central and induce shear forces due to rotations of the beads. This implies that for each particle, a combination of the rotational degrees, particle dimensions and the interactions through non-central forces should be taken into consideration.

In a series of recent studies, both experimental and numerical [16, 42], it was shown that a better description of the dynamics of one-dimensional (1D) granular chains is obtained when the other degrees of freedom of the elastic particles are taken into account. In particular, *rotation* seems to be not only important but can also lead to new physical phenomena. The additional rotational degrees of freedom provide extra flexibilities to dispersion engineering of phononic crystals and to the control of the propagation of elastic waves. Rotational motion can be easily excited by non central forces acting on the particles. In panel (i) of Fig. 1.6, we show an example of a magneto-granular crystal where the particles stay in contact due to the supporting magnets. In panels (ii) and (iii), the experimental observation of both longitudinal and transverse rotational waves is also depicted.

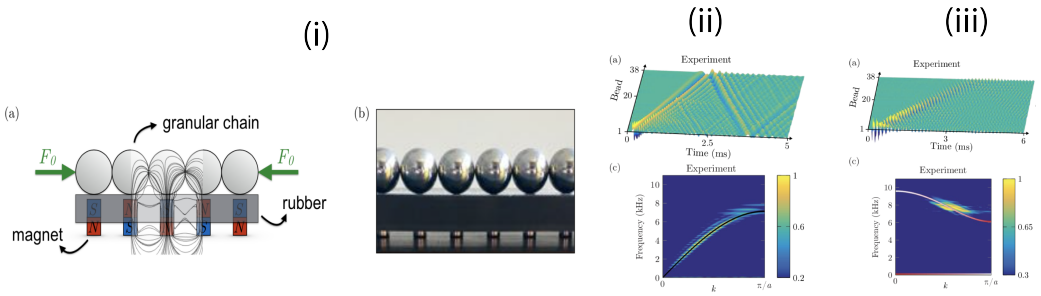

Fig. 1.6. (i) A sketch and an experimental picture of a 1D magneto-granular crystal. (ii) and (iii) the spatiotemporal evolution and the dispersion relation of the longitudinal and rotational waves obtained from experiments. All figures are taken from Ref. [43].

In this thesis we study 1D granular chains with additional degrees of freedom per lattice site and their effects regarding wave propagation.

Architected soft materials

Recently, it has been demonstrated that a novel type of artificial mechanical lattice that is highly deformable with soft springs, favor the manipulation of elastic/acoustic waves [17]. Such structures are also referred to as soft or nonlinear metamaterials and present opportunities to control the propagation of elastic waves, since their dispersion properties can be altered by by the pre-compression or geometrical characteristics. Initially, research was focused on the static behavior and the linear response of these structures. In Ref. [44], it was demonstrated that buckling can be used to manipulate the band structure of such lattices.

After several years of research in architected soft materials, the inherent strong nonlinearity in such materials has been demonstrated to support large-amplitude nonlinear waves known as solitons [45]. However, since the elastic elements of such soft nonlinear lattices can both be displaced and rotated at the same time, even in its simpler form the description of the corresponding waves is polarized. Thus, following the static and linear studies, new structures were composed and experimentally demonstrated to hold families of vector solitary waves.

Of interest to us, is the fact that these structures are configurable over a range of behaviors by taking advantage of geometric nonlinearities presented by the basic building blocks. This was recently used in Ref. [17] where a soft metamaterial composed of periodically arranged rotating crosses was found to support highly nonlinear elastic pulses in the form of vector solitons. The set-up of this experiment is shown in Fig 1.7.

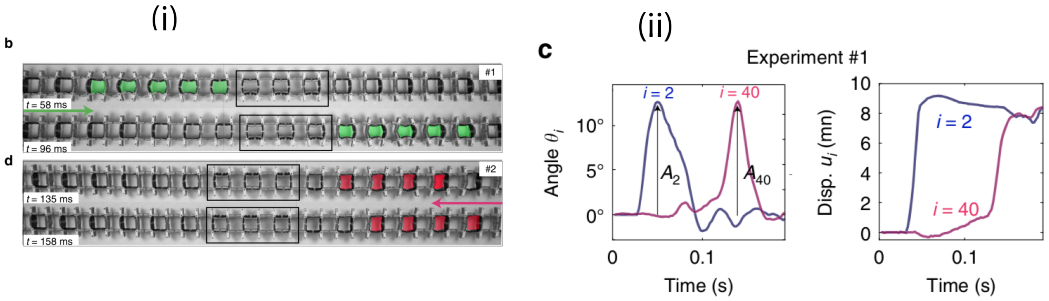

Fig. 1.7. (i) Snapshots of the experimental device of Ref. [17] at different time instants while the system is on a soliton diode operation.

Outline

In this thesis, we extend the studies regarding the interplay between disorder and nonlinearity by studying a particular class of elastic 1D lattices. One part is focused on finite disordered structures composed of spherical beads (a granular chain) taking

into account only the central forces and thus only the displacement from equilibrium of such particles. In this case, our focus is to understand how an initially localized mode is finally delocalized by nonlinearity, and what are the particularities of the granular nonlinearities with respect to other models as e.g., the FPUT. Thereafter, we are interested in studying disorder in lattices where rotations are introduced. Since both of the systems under study can support rotations, we consider first a generic model of masses and springs with both transverse and shear forces, and study the localization of such a polarized lattice under strong disorder. Finally, we use the lattice model corresponding to the soft metamaterial composed of LEGO bricks and exploit its strong nonlinearity to study the energy transfer in large disordered lattices.

The thesis is organized as follows. In Chapter 2, we review some of the spectral and dynamical properties of two universal mechanical lattice models, the mass-spring system and the KG lattice model. We study these systems, firstly, in the homogeneous state, and then we extend the characterization with heterogeneity to each of these lattices. We also introduce in detail all the indicators we use for the rest of the thesis in this chapter.

We study a disordered granular chain of spherical steel beads described by Hertzian contacts in Chapter 3. For the granular chain, we considered the in-plane motions for which the longitudinal degrees of freedom are decoupled from the other two degrees of freedom. This choice automatically means the system is effectively studied as an one dimensional chain since the transverse and rotational degrees of freedom are decoupled from the longitudinal degrees of freedom. For this system, we mainly consider the role played by the discontinuities in the system in aiding equipartition of energy as well as its chaoticity. A direct comparison with the FPUT model is also established featuring many differences.

In Chapter 4, we study a linear phononic system which is closely related to both a granular chain including rotations and the soft elastic LEGO bricks made structure. For this phononic crystal, we are interested in the polarization of the transported energy in the presence of strong disorder as well as the characteristics of the energy propagation for the system for different single site initial conditions.

In Chapter 5, we study the deformable and highly flexible lattice made of LEGO bricks. Although this system has three degrees of freedom like the phononic lattice which are reduced to two and the dynamics are much more complicated due to the intrinsic nonlinearity. We study an aligned version of the original structure with disorder on the masses and monitor the dynamics and how by traversing from the near linear to the strongly nonlinear regime, the energy spreading and the chaoticity changes.

Finally, in Chapter 6, we give the thesis conclusions and perspectives for future possible directions.

Chapter 2

One-dimensional Hamiltonian lattices

Contents

For many years, lattices have been widely used as models to describe problems in many areas of physical and life sciences. Some common examples are the phonon dynamics in condensed matter, the evolution of wave-packets in coupled waveguides, ultracold atoms in optical lattices and in general the wave propagation in complex media.

In this chapter, we present and review some details about two common 1D models namely the monoatomic mass-spring model and the discrete KG model. These two models will be used to describe and explain the phenomena observed in the three mechanical lattices considered in this thesis. For both models, we will consider and review the spectral and dynamic properties both with and without disorder. Additionally, we will give the definitions of different indicators which will use to describe the wave dynamics throughout this thesis.

2.1 Hamiltonian dynamical systems

2.1.1 Equations of motion and symplectic formalism

Dynamical systems can be described as a set of differential equations or difference equations governing the evolution of some variables, the values of which determine the present state of the system. For a dynamical system which has for example m state variables, the dimension thereof is $m \in \mathbb{N}$. The m state variables are usually represented by a state vector $\mathbf{x} = (x_1, x_2, x_3 \dots x_m)$ or a transposed matrix $\mathbf{x} = [x_1\, x_2\, x_3 \dots x_m]^T$. The space defined by $\mathbf{x}$ is called the system's phase space. For a phase space of m dimensions a state $\mathbf{x}$ gives a particular point in that space. The set of all the parameterized points $\mathbf{x}(t)$, where t is the discrete or continuous time, are termed an orbit of the dynamical system. There are two types of dynamical systems termed continuous and discrete. A continuous dynamical system is described by a set of continuous time differential equations of the form

$$\dot{\mathbf{x}} = \frac{d\mathbf{x}}{dt} = \vec{f}(\vec{x}). \tag{2.1}$$

Difference equations describe the so-called discrete dynamical systems or maps. In that case the dynamics of the system is defined by a set of equations of the form

$$x(t_{n+1}) = f(x(t_n)), \qquad n = 0, 1, 2, 3, \dots \tag{2.2}$$

A Hamiltonian system is an example of a continuous dynamical system whose dynamics is determined by the so called Hamiltonian function, which is a function of the system's state variables. If the Hamiltonian does not explicitly depend on time t, the system is called autonomous, while the explicit appearance of t in the functional form of the Hamiltonian makes the system non-autonomous. In this thesis we describe only autonomous Hamiltonian systems of the discrete type.

In classical mechanics, the functional form of a Hamiltonian is usually written as

$$H = \sum_{n=1}^{N} H\left(p_n, q_n\right) = T(\mathbf{p}) + V(\mathbf{q}), \tag{2.3}$$

where $\mathbf{q} = (q_1, q_2, \ldots, q_N)$ and $\mathbf{p} = (p_1, p_2, \ldots, p_N)$ are respectively the system's generalized positions $\mathbf{q}$ and momenta $\mathbf{p}$ for an N degrees of freedom (DOFs) Hamiltonian. Hamiltonians of the form in Eq. (2.3) consists of a kinetic and potential energy parts which are written respectively as $T(\mathbf{p})$ and $V(\mathbf{q})$. For Hamiltonians, the equations of motion are derived from Hamilton's equations and are written as

$$\frac{d\mathbf{p}}{dt} = -\frac{\partial H(\mathbf{p}, \mathbf{q})}{\partial \mathbf{q}}, \qquad \frac{d\mathbf{q}}{dt} = \frac{\partial H(\mathbf{p}, \mathbf{q})}{\partial \mathbf{p}}. \tag{2.4}$$

The system's generalized positions and momenta, can be expressed in the general setting of first order ordinary differential equations as

$$\frac{d\mathbf{x}}{dt} = \dot{\mathbf{x}} = \mathbf{J}_{2N} \cdot \mathbf{D}_H(\mathbf{x}(t)), \tag{2.5}$$

where $\mathbf{x} = (\mathbf{q}, \mathbf{p}) = (x_1, x_2, \ldots, x_N, x_{N+1}, \ldots, x_{2N}) = (q_1, q_2, \ldots, q_N, p_1, p_2, \ldots, p_N)$ is a vector representing the position of the system in its phase space and $(\dot{})$ denotes the first order derivative with respect to time t. In Eq. (2.5)

$$\mathbf{J}_{2N} = \begin{bmatrix} \mathbf{0}_N & \mathbf{I}_N \\ -\mathbf{I}_N & \mathbf{0}_N \end{bmatrix}, \tag{2.6}$$

is the symplectic matrix with $\mathbf{I}_N$ and $\mathbf{0}_N$ being the $N \times N$ identity and the null matrices respectively, and

$$\mathbf{D}_H = \left[\frac{\partial H}{\partial q_1}, \ldots, \frac{\partial H}{\partial q_N}, \frac{\partial H}{\partial p_1}, \ldots, \frac{\partial H}{\partial p_N}\right]^T, \tag{2.7}$$

with $[\,]^T$ denoting the transpose matrix.

2.1.2 Numerical scheme: Two part split symplectic integration

There is a class of integration schemes referred to as "symplectic" in which the geometrical properties of Hamiltonian equations of motion are preserved (e.g., their symplectic structure) [46].

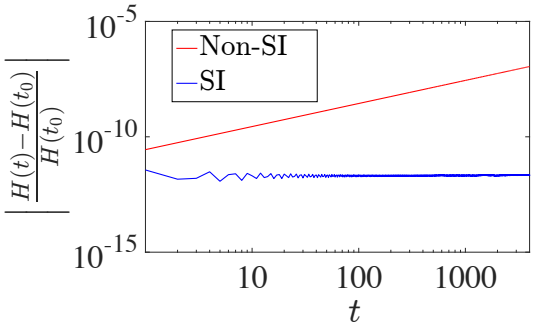

Fig. 2.1. Symplectic integration vs non-symplectic integration of the mass spring system to compare energy conservation for the two methods. For both schemes, the total system energy was $H = 0.5$ and a time step of $\tau = 0.01$ was employed.

The popular Runge-Kutta schemes [47, 48], fall into a class of what are known as non-symplectic integration schemes. Usually, for these schemes symplectic integration allows for long time integration of the system whilst preserving some conserved quantities such as the system total energy. We illustrate this point by integrating the Hamiltonian system with both the non-symplectic fourth order Runge-Kutta scheme and the `ABA864` [50], symplectic integrator (SI) as shown by the results in Fig. 2.1.
In this thesis we implement symplectic integration since the Hamiltonians of the systems considered are autonomous. In order to implement symplectic integration, we consider the Hamiltonian $H = H(\mathbf{p}, \mathbf{q})$ which can be separated into two integrable parts, namely $H = A(\mathbf{p}, \mathbf{q}) + B(\mathbf{p}, \mathbf{q})$. Formally the solution of the Eq. (2.5) can be written as

$$\frac{d\mathbf{x}}{dt} = \Big\{H, \mathbf{x}\Big\} = L_H\ \mathbf{x} \Rightarrow \mathbf{x}(t) = \sum_{n\geq 0} \frac{t^n}{n!} L_H^n\ \mathbf{x} = e^{tL_H}\mathbf{x}, \tag{2.8}$$

where $\mathbf{x}$ is the full coordinate vector as already defined and L_H is the Poisson operator

$$L_H f = \sum_{j=1}^{N} \left\{ \frac{\partial H}{\partial p_j}\frac{\partial f}{\partial q_j} - \frac{\partial H}{\partial q_j}\frac{\partial f}{\partial p_j} \right\}. \tag{2.9}$$

It then follows that we can approximate the action of the operator $e^{L_H} = e^{L_A} + e^{L_B}$ by the successive actions of products of the operators e^{L_A} and e^{L_B} (see e.g., ref. [49] for details).

$$e^{\tau L_H} = \prod_{i=1}^{k} e^{a_i \tau L_A} e^{b_i \tau L_B} + \mathcal{O}\left(\tau^{n+1}\right), \tag{2.10}$$

for appropriate choices of the real coefficients a_i, b_i with $i = 1, \ldots, k$ and τ denotes the integration time step. Different choices of coefficients a_i and b_i lead to schemes of different accuracy. In Eq. (2.10), n is called the order of a SI. Hamiltonians of the form of Eq. (2.3) can be split into two integrable parts $H = A(\mathbf{p}) + B(\mathbf{q})$, with each part having N cyclic coordinates. The kinetic energy part is $A(\mathbf{p})$ whilst the potential energy part is $B(\mathbf{q})$. This type of splitting is the most commonly used in the literature, therefore a large number of SIs have been developed for such splits. We can therefore write the explicit form of a common and highly efficient symmetrical 4^{th} order integrator, the `ABA864` SI as

$$\begin{aligned} \texttt{ABA864}(\tau) = {} & e^{a_1\tau L_A} e^{b_1\tau L_B} e^{a_2\tau L_A} e^{b_2\tau L_B} e^{a_3\tau L_A} e^{b_3\tau L_B} e^{a_4\tau L_A} e^{b_4\tau L_B} \ldots \\ & \times e^{a_4\tau L_A} e^{b_3\tau L_B} e^{a_3\tau L_A} e^{b_2\tau L_B} e^{a_2\tau L_A} e^{b_1\tau L_B} e^{a_1\tau L_A}. \end{aligned} \tag{2.11}$$

The coefficients for the `ABA864` SI are given in Ref. [50]. Some recent reviews on symplectic and nonsymplectic integration can be found in [51, 52].

2.1.3 Indicators used for the evolution analysis

During the time integration of Eq. (2.5), we compute certain indicators which help to quantitatively describe the wave-packet evolution.

2.1.3.1 Participation number

Wave-packet spreading phenomena is usually studied by exciting a single site, usually in the middle of a sufficiently large lattice to avoid boundary effects. The energy will then spread to the rest of the lattice from the point of initial excitation. One of the common tools used to characterize the wave-packet spreading or lack of it is the participation number (P), [53], which is computed as

$$P = \frac{1}{\sum_{n=1}^{N} h_n^2}, \tag{2.12}$$

where $h_n = H_n/H$ is the normalization of the site energy H_n. P is an indicator of the "evenness of the energy distribution" and it becomes $P \approx N$ when the energy is evenly distributed to all sites, while $P = 1$ when only one site is excited.

2.1.3.2 Energy density moments

We also consider the moments of energy distribution as they describe the wave-packet spreading [54, 55]. The kth moment is computed from the equation

$$m_k = \sum_{n=1}^{N} |n - n_0|^k \, h_n. \tag{2.13}$$

where n_0 denotes the mean position. However, for the work in this thesis we only compute m_2 which can be thought of as the variance of the energy distribution.

2.1.3.3 Exponents

Assuming a polynomial dependence of the spreading, for sufficiently long times, we may write $m_2 \propto t^{\beta}$ and the parameter β is used to quantify the asymptotic spreading behavior. The estimate of the rate of change

$$\beta = \frac{d \log_{10} m_2(t)}{d \log_{10} t}, \tag{2.14}$$

is obtained numerically through a central finite difference scheme as the values of $m_2(t)$ are analyzed in log-log scale after smoothing the $m_2(t)$ for example by a weighted regression algorithm [56, 57]. Similar arguments hold for the computation of the exponent of $P \propto t^{\alpha}$, where the exponent α is defined as

$$\alpha = \frac{d \log_{10} P(t)}{d \log_{10} t}. \tag{2.15}$$

For disordered systems, we perform numerical simulations for many disorder realizations. From the large number of realizations, we calculate the mean values of the second moment $\langle m_2 \rangle$ and the participation number $\langle P \rangle$. Thus the corresponding asymptotic exponents are calculated from these mean values as

$$\beta = \frac{d \log_{10} \langle m_2(t) \rangle}{d \log_{10} t}, \; \alpha = \frac{d \log_{10} \langle P(t) \rangle}{d \log_{10} t}. \tag{2.16}$$

2.1.3.4 Deviation vectors and the maximum Lyapunov exponent

To determine (globally) the chaotic behavior in multi-dimensional nonlinear Hamiltonian systems, the mLE and its finite time variance can be calculated using the so called standard method [58, 59]. To achieve this, we first consider some small perturbations $\mathbf{w}(t)$ from the trajectory $\mathbf{x}(t)$, which we denote

$$\mathbf{w}(t) = (\delta\mathbf{p}(t), \delta\mathbf{q}(t)) = (\delta q_1(t), \delta q_2(t), \ldots, \delta q_N(t), \delta p_1(t), \delta p_2(t), \ldots, \delta p_N(t)). \quad (2.17)$$

The evolution of the deviation vector $\mathbf{w}$ is obtained by linearizing the equations of motion leading to the following equation

$$\dot{\mathbf{w}}(t) = [\ \mathbf{J}_{2N} \cdot \mathbf{D}_H^2(\mathbf{x}(t))] \cdot \mathbf{w}(t), \quad (2.18)$$

where

$$[\mathbf{D}_H^2(\mathbf{x}(t))]_{i,j} = \left.\frac{\partial H^2}{\partial x_i \partial x_j}\right|_{x(t)} \qquad i, j = 1, 2, 3, \ldots, 2N \quad (2.19)$$

is the i, j element of the $2N \times 2N$ Hessian matrix $\mathbf{D}_H^2(\mathbf{x}(t))$ computed on the phase space trajectory $\mathbf{x}(t)$. Eq. (2.18) is linear in $\mathbf{w}(t)$, with coefficients depending on the system's trajectory $\mathbf{x}(t)$.

Using the time evolution of $\mathbf{w}(t)$, we may compute the finite time mLE using the following expression

$$\lambda(t) = \frac{1}{t} \ln \left[\frac{||\mathbf{w}(t)||}{||\mathbf{w}(t_0)||} \right]. \quad (2.20)$$

To characterize the regularity or chaoticity of a trajectory, we utilize one of the most commonly used chaos indicators, the finite time mLE , which is defined as $\Lambda = \lim_{t\to+\infty} \lambda(t)$. In Eq. (2.20), $||\cdot||$ denotes the usual Euclidian norm, while $\mathbf{w}(t_0)$ and $\mathbf{w}(t)$ are respectively the deviation vectors at $t = t_0$ and $t > t_0$. Here it is important to note that in the case of regular (non chaotic) dynamics, $\lambda(t)$ tends to zero following the power law $\lambda(t) \propto t^{-1}$. On the other hand when $\lambda(t)$ saturates to a positive asymptotic value the system is in a chaotic state. Cases where the time dependent mLE tends to zero but with a power law $\lambda(t) \propto t^{-\gamma}$ with $\gamma < 1$ are called weakly chaotic.

2.1.3.5 Deviation vector distribution

For chaotic trajectories, $\lambda(t)$ only gives a global status of the entire system and we remain with no additional information on the spatial distribution of chaos which may for example feature localization (chaotic spots). In order to extract the information on the nature of these chaotic spots, whether they move throughout the phase space or are confined to a certain region we use the normalized deviation vector distribution (DVD) [34] defined as

$$\xi_n = \frac{\delta q_n^2 + \delta p_n^2}{\sum_{n=1}^{N} \delta q_n^2 + \delta p_n^2}. \quad (2.21)$$

The DVD gives a measure of the sensitivity of a certain region of the chain to small variations of initial conditions and provides some idea of the "strength of the chaoticity" at each site as the system evolves.

In practice, when we perform numerical simulations, the variational equations Eq. (2.18) are integrated along with the equations of motion Eq. (2.5). In particular, we basically evolve in time the general vector $\mathbf{X}(t) = (\mathbf{x}(t), \mathbf{w}(t))$ by solving the system

$$\dot{\mathbf{X}}(t) = (\dot{\mathbf{x}}(t), \dot{\mathbf{w}}(t)) = \mathbf{f}(\mathbf{X}) = \begin{bmatrix} \mathbf{J}_{2N} \cdot \mathbf{D}_H(\mathbf{x}(t)) \\ [\, \mathbf{J}_{2N} \cdot \mathbf{D}_H^2(\mathbf{x}(t))] \cdot \mathbf{w}(t) \end{bmatrix}. \tag{2.22}$$

This is also known as the "tangent map method", see e.g., Ref. [60, 61, 62].

2.2 Homogeneous linear one-dimensional mass-spring system

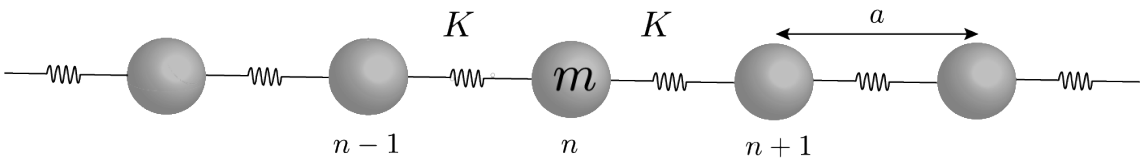

Fig. 2.2. Schematic of the one-dimensional (1D) mass-spring system.

Here we briefly review the properties of the well studied [63, 64, 65, 66], prototypical model of a chain of masses connected by linear springs as shown in Fig. 2.2. The Hamiltonian for this system has the following functional form

$$H = \sum_{n=1}^{N} \frac{p_n^2}{2m} + \frac{K}{2}(u_{n+1} - u_n)^2, \tag{2.23}$$

where u_n denotes the displacement of the nth mass from equilibrium, $p_n = m\dot{u}_n$ is the particle's momentum and K is a stiffness constant characterizing the linear springs. The corresponding equation of motion [see Eq. (2.4)] for the nth mass is given by

$$m\ddot{u}_n = K\left(u_{n+1} + u_{n-1} - 2u_n\right). \tag{2.24}$$

2.2.1 Spectral properties

Assuming solutions of the form

$$u_n = Ae^{i(qx_n - \omega t)}, \tag{2.25}$$

where $x_n = na$ and a denotes the lattice periodicity. This solution is meant to model a traveling wave where each particle oscillates about its equilibrium position with the same frequency ω and the same amplitude A while q denotes the wavenumber of the Bloch wave solutions. Here we first consider an infinite chain. When we plug back the solutions into Eq. (2.24), we obtain the expression

$$-m\omega^2 e^{iqna} = K\left(e^{iq(n+1)a} + e^{iq(n-1)a} - 2e^{iqna}\right). \tag{2.26}$$

After a further simplification of Eq. (2.26) we obtain the dispersion relation

$$\omega = \sqrt{\frac{4K}{m}} \sin\left(\frac{qa}{2}\right), \tag{2.27}$$

which is shown in Fig. 2.3(a). This is the typical acoustic dispersion relation where we can also easily recognize from the group velocity

$$v_g = \frac{d\omega}{dq} = \sqrt{\frac{K}{m}} \cos\left(\frac{qa}{2}\right), \tag{2.28}$$

that the speed of sound is given by $v_s \to \sqrt{\frac{K}{m}}$ obtained for $q \to 0$.

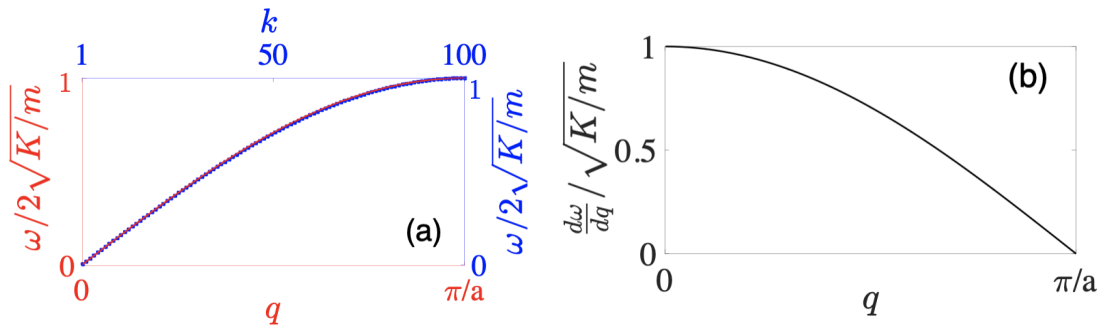

Fig. 2.3. (a) Dispersion relation (red curve) and the eigenfrequencies (blue circles) for a mass-spring chain of 100 masses obtained via Eq. (2.29). (b) Group velocity for the mass-spring system plotted as a function of the wave number q. We consider a homogeneous chain with stiffnesses $K = 1$ and and masses $m = 1$.

Since we are interested in finite mechanical lattices relevant to experimental settings, here we present the spectral properties of a finite system of N masses. In all the calculations in this thesis we will use fixed boundary conditions defined by $u_0 = u_{N+1} = 0$. We also assume solutions of the system of N equations [Eq. (2.24)] to be of the form $\mathbf{u}(t) = \mathbf{U}e^{-i\omega t}$, where $\mathbf{U} = [U_1, U_2, \ldots, U_N]$. We thus obtain the eigenvalue problem

$$-\omega_k^2 \mathbf{M}\mathbf{U}_k = \mathbf{K}\ \mathbf{U}_k, \tag{2.29}$$

where ω_k are the eigenfrequencies and $\mathbf{U}_k$ the corresponding eigenvectors. Here, the matrix $\mathbf{M}[m]$ is a diagonal matrix with mass elements m and $\mathbf{K}[K]$ is a sparse diagonal matrix containing the stiffness coefficients K. For this particular case the matrices $\mathbf{M}$ and $\mathbf{K}$ with fixed-fixed boundary conditions have the following form

$$\mathbf{M} = \begin{pmatrix} m & & & & \\ & m & & & \\ & & \ddots & & \\ & & & m & \\ & & & & m \end{pmatrix}, \quad \mathbf{K} = \begin{pmatrix} -2K & K & & & & \\ K & -2K & K & & & \\ & \ddots & \ddots & \ddots & & \\ & & K & -2K & K & \\ & & & & K & -2K \end{pmatrix}$$

The discrete spectrum for a chain of 100 masses is depicted by circles in Fig. 2.3(a). In Fig. 2.4, we show some typical examples of the profile of the modes of the finite chain reminding the fact that low frequency modes have a wavelength at the order of the total lattice length, while high frequency modes have a wavelength comparable to the lattice spacing.

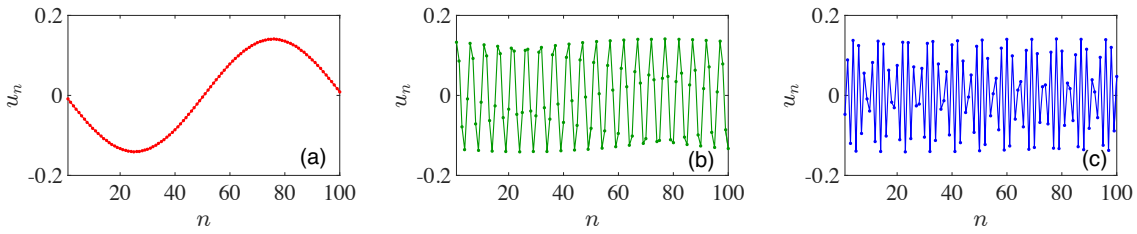

Fig. 2.4. Profiles of (a) mode 2 (b) mode 40 and (c) mode 90 for a homogeneous mass-spring lattice of size 100.

2.2.1.1 Projections of initial conditions onto normal modes

For most of the numerical simulations in this thesis, we consider *single site* excitations usually at the center of the lattice, and then study how such initially localized wave-packets spread through the total lattice. This particular choice is often found in the literature [67, 68] when studying wave propagation in disorder lattices. This choice is advantageous in the sense that it is both a natural choice to excite the system in practice as well as being efficient in exciting strongly most of the modes in the system.

To illustrate this, we now show how such a state (with only one site excited) is projected on the modes of the finite lattice. Note that for a finite chain of N masses the system has $2N$ degrees of freedom, i.e., the N displacements u_n and the N momenta p_n. A single site state can be achieved for example, by implementing a single finite displacement or a single finite momentum. A displacement initial excitation for a chain of size N with N even, we set $u_{N/2} = U_0$ where U_0 is a real constant and $u_n = 0$ for all $n \neq N/2$. We then project the single site state vector $\mathbf{U}_0$ onto the normal modes and obtain the projections such that

$$\mathbf{R} = \mathbf{A}^{-1}\mathbf{U}_0, \tag{2.30}$$

$$\mathbf{U}_0 = [0, \ldots, U_0, \ldots, 0]^T, \tag{2.31}$$

where $\mathbf{A}$ is an $N \times N$ matrix with the eigenvectors $\mathbf{U}_k$ as columns. The element R_k of the vector $\mathbf{R}$ is the amplitude coefficient of the kth eigenmode. Note that the amount of energy that each mode acquires in this case is equal to $E_k = \omega_k^2 R_k^2/2$.

A similar analysis is done for the case of a state with single site momentum initial excitation, $p_{N/2} = P_0$ where P_0 is a real constant and $p_n = 0$ for all $n \neq N/2$. In this case the projection onto the modes is also given by

$$\mathbf{P} = \mathbf{A}^{-1}\mathbf{V}_0, \tag{2.32}$$

$$\mathbf{V}_0 = [0, \ldots, P_0, \ldots, 0]^T. \tag{2.33}$$

For a single site momentum state the energy acquired by each mode is then given by $E_k = P_k^2/2$ where P_k is the kth element of projection vector $\mathbf{P}$. The projections of the

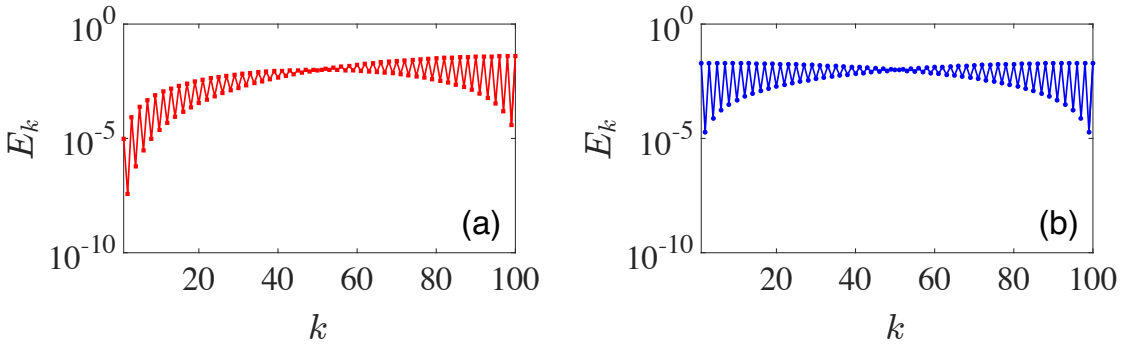

Fig. 2.5. The energy acquired by each mode using a single site (a) displacement and (b) momentum state onto the orthonormalized eigenmodes of a mass-spring system with $N = 10^3$. The index k takes the ordered modes from lowest frequency (low k values) to high frequency (high k values).

two different single site states on to the normal modes of a lattice with $N = 10^3$ sites, are depicted in Fig. 2.5 for the single site displacement (a) and single site momentum (b). Firstly, we observe that for both cases all the modes acquire a finite energy justifying the choice of such a state as an initial condition. However, as we can easily see, the energy per mode for the single site displacement is weighted by ω_k which results to a very weak excitation of the low frequency modes with respect to the single momentum state where almost all modes are excited equally. As we shall encounter later, this difference plays a crucial role in the dynamics of disorder lattices when initially excited with either a single displacement or momentum [54].

2.2.2 Dynamical properties

Having considered some of the spectral properties which are important in understanding the dynamics of the mass-spring system, we now consider the dynamical properties themselves. We initialize the system by either a single site momentum $[\mathbf{p}(t = 0) = \mathbf{V}_0)]$ or displacement $[\mathbf{u}(t = 0) = \mathbf{U}_0]$ excitation, and evolve the trajectory in time using Eq. (2.5) since the the system is linear. We describe the dynamical behavior by considering some snapshots of the energy density, the spatiotemporal surface plot of the energy density as well as P, m_2 and their respective exponents α and β.

2.2.2.1 Energy density profiles and snapshots

The spatiotemporal evolution of the energy densities shows slightly different dynamics between momentum and displacement initial excitations of the mass-spring system as depicted in Figs. 2.6(a) and (c), where we show similar energy density profiles for momentum and displacement initial excitations respectively. We also take snapshots during the evolution of the system at $t = 100$ and $t = 150$ for each initial excitation [see Figs. 2.6(b) and (d)] . In Fig. 2.6, the profiles in (a) and (c) are different due to the different ways the modes are excited. This is especially the case for the low frequency modes. For momentum initial excitations, the low frequency modes are excited with the same probability as any other mode. However, for displacement excitations, the

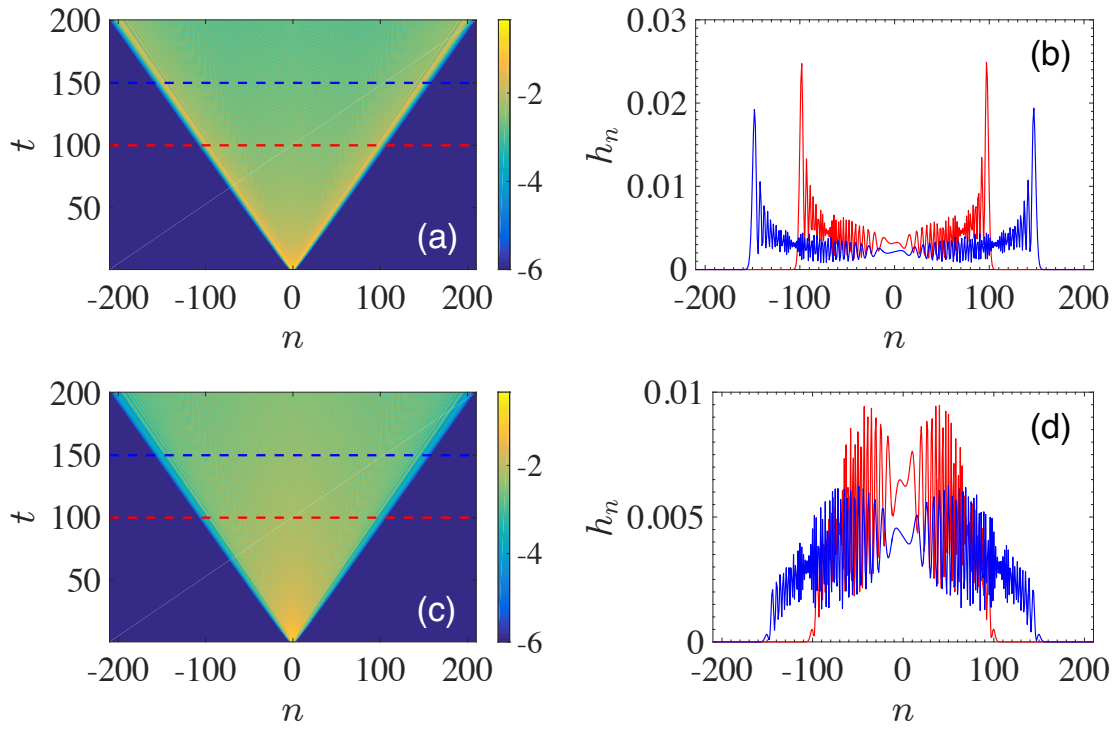

Fig. 2.6. (a) Spatiotemporal evolution of energy density for the mass-spring system with parameters $K = 1$ and $m = 1$ for momentum initial condition. The color bars are in logarithmic scale. (b) Energy density snapshots are taken at $t = 100$ shown by the red dashed line in (a) and $t = 150$ as shown by the blue dashed line in (a). The results for displacement initial conditions are shown in (c) and (d).

low frequency modes are excited weakly hence the propagating front for displacement excitations is much fainter [compare Figs. 2.6(b) and (d)]. Both initial excitations have a ballistic front which propagates at a speed of $v_s = \sqrt{K/m}$ (here $v_s = 1$). Notice that in our numerical simulations regarding the dynamics, the lattice is made to be sufficiently large to ensure that the wave-packet does not reach the boundaries in order to avoid finite size effects.

2.2.2.2 Time evolution of P, m_2 and β

Here we show the typical behavior of the different indicators to be used in this thesis, for the simple case of the homogeneous mass-spring system. Firstly, we discuss the evolution of the participation number which is shown in Fig. 2.7(a) for both types of initial excitations.

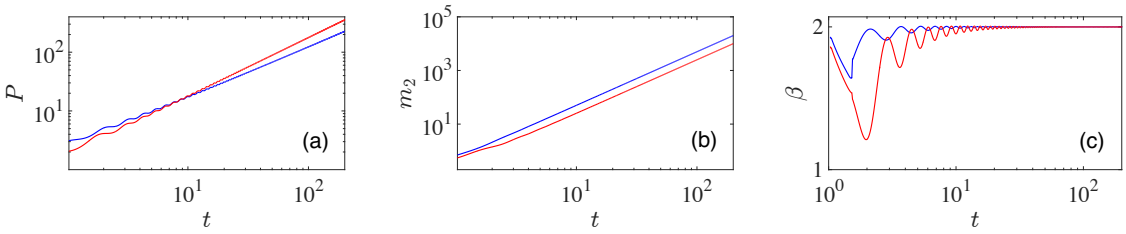

Fig. 2.7. (a) Time evolution of (a) P, (b) m_2 and (c) β for single site momentum (blue curves) and displacement (red curves) initial excitations for the mass-spring system. Both excitations show ballistic spreading ($\beta = 2$).

It is clear that initially P is of the order of unity since we are exciting a single site, and as time grows more and more sites are excited as the wave-packet spreads. In fact, at the end of the simulation almost all the sites are excited and $P \gtrsim 200$ as expected also by observing the energy density at $t \approx 200$ in Figs. 2.6(a) and (b).

The time evolution of the energy distribution second moment $m_2(t)$ is shown in Fig. 2.7(b) from where one directly observes that it increases with time indicating that the initially localized wave-packet is always spreading. This is what is expected for periodic systems where all modes are extended and are excited hence energy is transferred to all lattice sites. Furthermore, the spreading is also characterized by the exponent β which as shown in Fig. 2.7(c) it takes a value of $\beta = 2$ signaling ballistic energy transport for both types of initial conditions.

2.3 Homogeneous linear one-dimensional discrete Klein-Gordon lattice

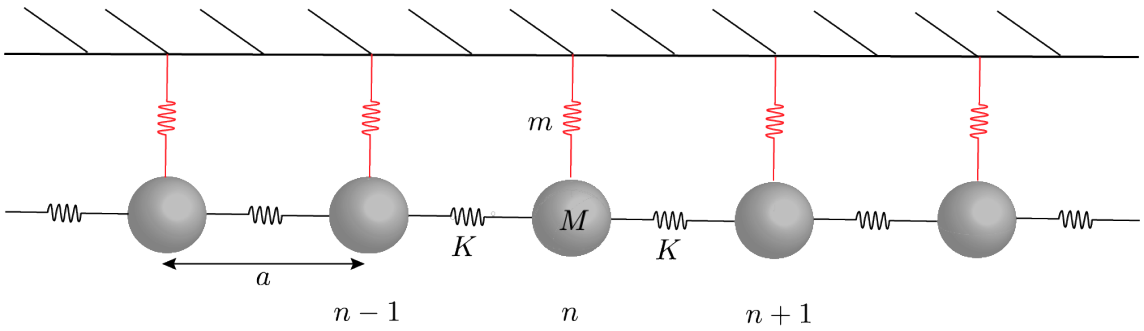

Fig. 2.8. Schematic of the discrete KG lattice with nearest neighbor potentials (depicted as black colored springs) and the onsite potential (depicted as red colored springs).

We now turn our attention to the discrete KG lattice model [69, 70, 31, 71] whose Hamiltonian is given by the following expression

$$H = \sum_n \frac{1}{2}\pi_n^2 + \frac{1}{2}(\phi_{n+1} - \phi_n)^2 + \frac{1}{2}m\phi_n^2, \tag{2.34}$$

where m is a positive constant and n is the site index. We also set the masses and spring constants as $M = 1$ and $K = 1$ respectively. Here we have changed the notation to ϕ_n and π_n for the positions and momenta respectively in anticipation of an upcoming chapter where a KG-type equation will be used to describe the rotation of elastic mechanical lattices. In addition, note that for a mechanical system such as the mass-spring system of Section 2.2, the KG lattice can be obtained by assuming that each mass is also coupled to a rigid substrate with an additional spring. The corresponding equations of motion for the KG lattice are obtained from Hamilton's equations Eq. (2.4) and are explicitly written as

$$\ddot{\phi}_n = (\phi_{n+1} + \phi_{n-1} - 2\phi_n) - m\phi_n, \qquad \dot{\phi}_n = \pi_n. \tag{2.35}$$

2.3.1 Spectral properties

As it was done for the mass-spring system, we assume solutions of the form $\phi_n = Be^{i(qx_n - \omega t)}$, where $x_n = na$. This solution is meant to model a traveling wave where each particle oscillates about its equilibrium position with the same frequency ω and the same amplitude B. The q denotes the lattice wave vector. Plugging this ansatz back to Eq. (2.35), we obtain the expression

$$-\omega^2 e^{iqna} = \left(e^{iq(n+1)a} + e^{iq(n-1)a} - 2e^{iqna}\right) - me^{iqna}, \tag{2.36}$$

and further simplification of Eq.(2.36) yields the dispersion relation of the KG lattice,

$$\omega = \sqrt{m + 4\sin^2\left(\frac{qa}{2}\right)}, \tag{2.37}$$

which is shown in Fig. 2.9(a).

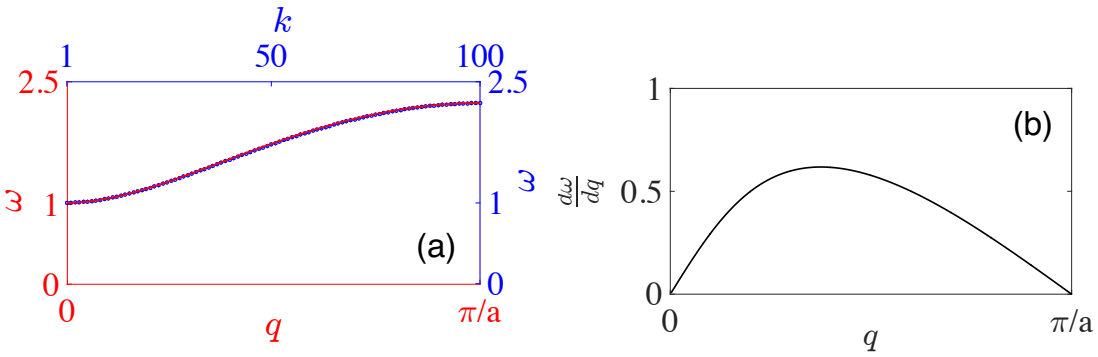

Fig. 2.9. (a) Dispersion relation (red curve) and the eigenfrequencies (blue circles) for the discrete KG lattice of 100 masses obtained via Eq. (2.39). (b) Group velocity for the KG model plotted as a function of the wave number q. We consider a homogeneous chain with $K = 1$ and and onsite potential coefficient $m = 1$.

The most important difference between the mass-spring and the KG lattice lies in the band gap of magnitude $\sqrt{m}$ which is present in the KG lattice. In particular the KG

system does not support propagating waves for vanishing frequencies. Furthermore the group velocity

$$v_g = \frac{d\omega}{dq} = \frac{2\cos\left(\frac{qa}{2}\right)\sin\left(\frac{qa}{2}\right)}{\sqrt{1+4\sin^2\left(\frac{qa}{2}\right)}}, \tag{2.38}$$

of the KG lattice indicates that waves at both the beginning and the end of the Brillouin zone have vanishing group velocities. Similar to the mass-spring system, for a finite lattice of size N, we assume harmonic solutions of the form $\mathbf{\Phi}(t) = \mathbf{\Phi}e^{i\omega t}$, where $\mathbf{\Phi}$ is a column vector and obtain the eigenvalue problem

$$-\omega_k^2 \mathbf{\Phi}_k = \mathbf{K}(m)\mathbf{\Phi}_k, \tag{2.39}$$

where now the "stiffness" matrix is given by,

$$\mathbf{K} = \begin{pmatrix} -(2+m) & 1 & & & & \\ 1 & -(2+m) & 1 & & & \\ & \ddots & \ddots & \ddots & & \\ & & 1 & -(2+m) & 1 & \\ & & & 1 & -(2+m) & \end{pmatrix}.$$

The eigenfrequencies of a KG lattice with $N = 100$ are shown in Fig. 2.9(a). For completeness sake, we also show some examples of profiles of the modes for the homogeneous KG lattice in Fig. 2.10 which bare a big resemblance with the ones of the mass-spring system.

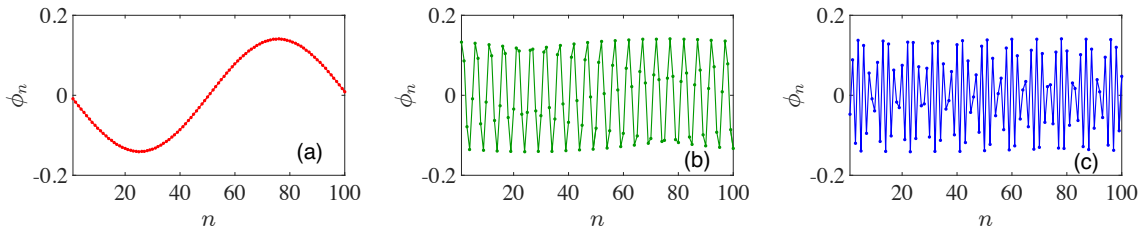

Fig. 2.10. Profiles of (a) mode 2 (b) mode 40 and (c) mode 90 for a homogeneous KG lattice of size 100.

2.3.1.1 Projections of initial conditions onto normal modes

As was the procedure in Section. 2.2.1.1, here also we will consider how the two types of single site state vectors excite the systems normal modes. The energy acquired by each mode is plotted in Fig. 2.11 for the single site displacement (left) and momentum (right) state. Here, in contrast to the case of the mass-spring system (see Fig. 2.5), both types of vectors result in a quite similar excitation of the normal modes. This can be understood by noting that for both lattices an initial momentum excitation assigns an energy to each mode equal to $E_k = P_k^2/2$, while for the case of the initial displacement the energy per mode is weighted by the frequency as $E_k = \omega_k^2 R_k^2/2$ where P_k and R_k are the projection coefficients. Thus for the KG model, the lowest propagating frequencies are significantly excited in contrast to the mass-spring system.

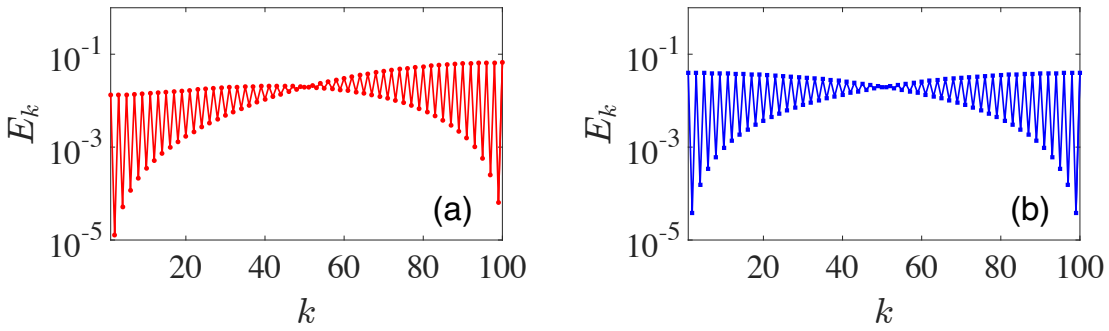

Fig. 2.11. Projections of single site initial (a) displacement and (b) momentum excitations onto the orthonormalized eigenmodes of the KG lattice model.

2.3.2 Dynamical properties

Similar to what was done in Section. 2.2.2, we again consider the dynamical properties to better understand the propagation of wave-packets in the KG lattice. To do so we use the same single site initial conditions both in displacement and in momentum.

2.3.2.1 Energy density profiles and snapshots

The results for a lattice of $N = 200$ sites and for $m = 1$ are shown in Fig. 2.12. Firstly, we note that compared to the mass-spring system, for the same normalized time the wave-packet did not reach the $\pm$200th site. This implies that the maximum speed in the KG lattice with $m = 1$ is smaller than unity which is in fact easily seen by calculating the maximum group velocity (for $m = 1$) which is around 0.62 [see Fig. 2.9(b)] . As discussed before, for the KG lattice, both single site displacement and single site momentum excitations assign similar energy to the linear modes. As such, the profiles for both cases look alike as indicated by the snapshots during evolution shown in Figs. 2.12(b) and (d) featuring a ballistic propagating front.

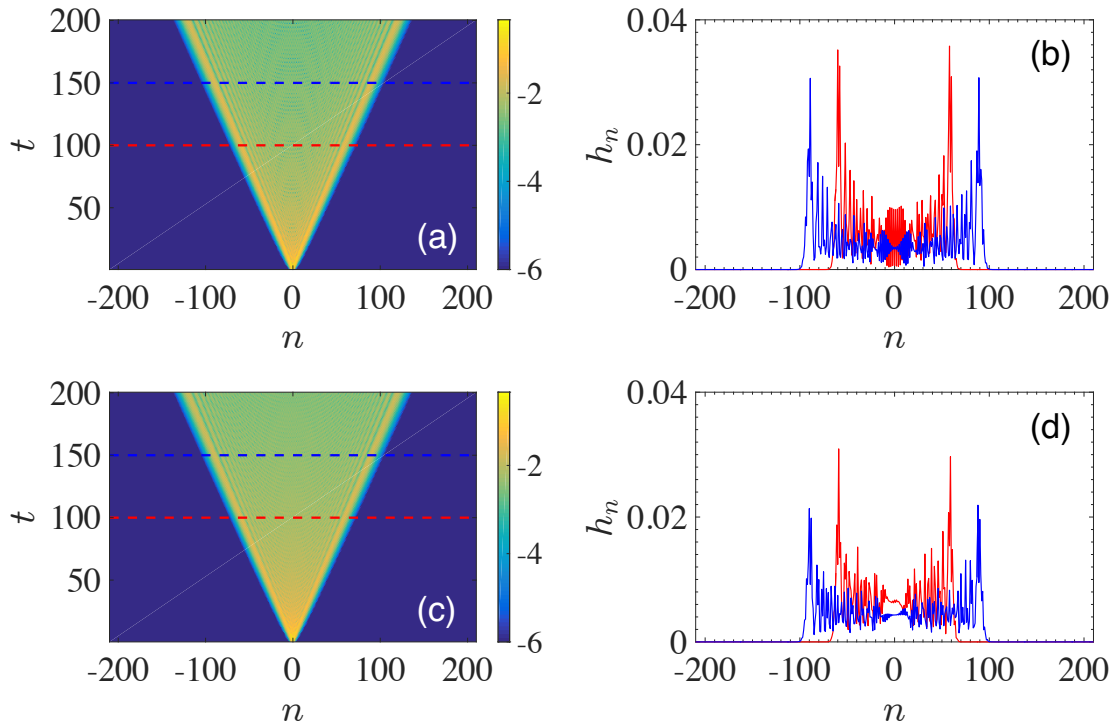

Fig. 2.12. (a) Spatiotemporal evolution of energy density for the KG lattice with onsite parameter $m = 1$ for momentum initial condition. The color bars are in logarithmic scale. (b) Energy density snapshots are taken at $t = 100$ shown by the red dashed line in (a) and $t = 150$ as shown by the blue dashed line in (a). The results for displacement initial conditions are shown in (c) and (d).

Again these snapshots are very much similar since almost similar modes are excited for the two initial conditions. Although there are some ballistic fronts for both excitations. We note that the speed of the propagating fronts is much less that the speeds observed for the mass-spring system at least for the parameter $m = 1$.

2.3.2.2 Time evolution of P, m_2 and β

To conclude the comparison of the homogeneous cases of the two models, we also show the evolution of the different indicators. Here, as shown in the panels of Fig. 2.13, we barely recognize any difference between the two models since also for the KG lattice, P starts of the order unity and grows up to the order of N, and the second energy moment m_2 also grows as $m_2 \propto t^{\beta}$ with an asymptotic value of $\beta = 2$ signaling ballistic behavior.

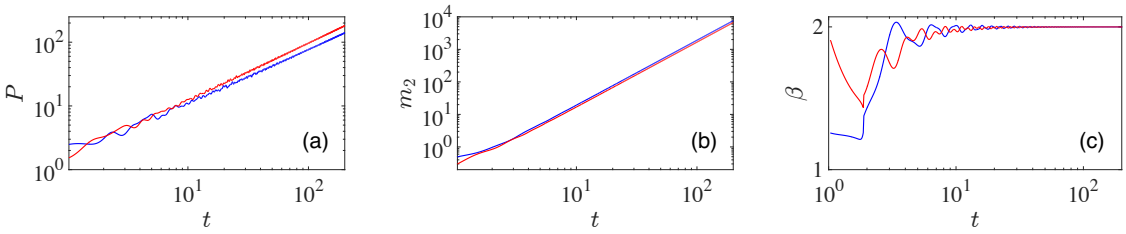

Fig. 2.13. (a) Time evolution of (a) P, (b) m_2 and (c) β for single site momentum (blue curves) and displacement (red curves) initial excitations for the KG lattice. Both excitations show ballistic spreading ($\beta = 2$).

A similar power law relation $m_2 \propto t^\beta$ with $\beta = 2$ also exists for the second moment for both types of excitations similar to the results for the mass-spring system. There appears to be no difference in the dynamics for either momentum or displacement initial excitations as shown by the results in both Fig. 2.12 and Fig. 2.13.

2.4 Disordered linear one-dimensional mass-spring system

2.4.1 Spectral properties

We now introduce disorder to the mass-spring system we have described in Section. 2.2 by taking the mass at the nth site, m_n, from a uniform random distribution such that $m_n \in [0.1, 1.9]$. The Hamiltonian for the disordered mass-spring system is now written as

$$H = \sum_{n=1}^{N} \frac{p_n^2}{2m_n} + \frac{K}{2}(u_{n+1} - u_n)^2. \tag{2.40}$$

Note here that we could have introduced disorder in the stiffnesses instead on the masses. However, Lepri and coworkers [55] have shown that the choice of where to put the disorder is immaterial and they have shown how the two types of disorder can be mapped by a transformation which connects disorder in mass to disorder in the stiffness. The corresponding equations of motion for the disorder lattice are

$$m_n \ddot{u}_n = K\left(u_{n+1} + u_{n-1} - 2u_n\right). \tag{2.41}$$

Here, to analyze the spectrum of a disordered mass-spring chain we consider an ensemble of disorder realizations and we also calculate averages over these ensembles. The spectrum of a mass disordered mass-spring system can be numerically obtained by following a similar procedure as in Section. 2.2.1 although now the mass matrix $\mathbf{M}[m_n]$ has random elements. The corresponding eigenvalue problem to be solved numerically is given by

$$-\omega_k^2 \mathbf{M}(m_n)\mathbf{U}_k = \mathbf{K}\ \mathbf{U}_k. \tag{2.42}$$

Here as an example, we study disorder in mass with mean value of $\langle m \rangle = 1$ and the masses are taken from a uniform distribution within the values $m_n \in [0.1, 1.9]$. We also fix $K = 1$ in order to be able to compare with the results of Section. 2.2. The

corresponding averaged disorder frequency spectrum over 500 realizations is shown in Fig. 2.14(a).

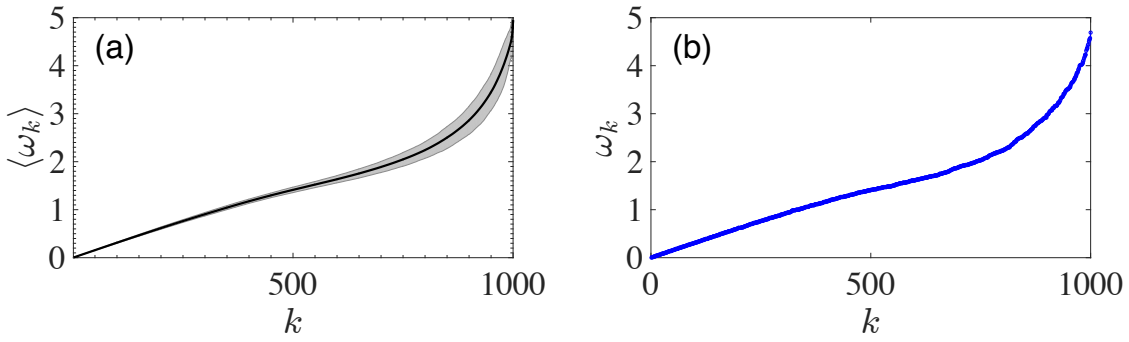

Fig. 2.14. (a) Averaged frequency spectrum over 500 disorder realizations for a disordered mass-spring system. The index k takes the ordered modes from lowest frequency (low k values) to high frequency (high k values) and the lightly shaded areas indicate statistical error. (b) Eigenfrequencies of a randomly chosen representative realization of a disordered mass-spring lattice.

Firstly, we note that, in comparison to the corresponding homogeneous lattice with $m = K = 1$ where the maximum allowed frequency was $\omega_{\max} = 2$, for the disorder case, modes may appear for much larger values of frequency. Furthermore, the eigenmodes of the system now constitute a set of extended modes as well as a set of localized modes. In fact, it is known that for this particular type of lattice, there are about $\sqrt{N}$

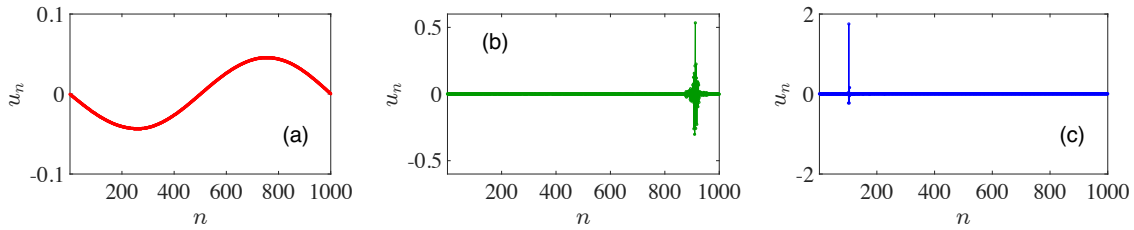

Fig. 2.15. Profiles of (a) mode 2 (b) mode 500 and (c) mode 900 for a representative disordered mass-spring system of size 1000.

extended modes [72, 73, 54]. The origin of these extended modes lies in the dispersion relation for the homogeneous case and especially in the low frequency modes close to $\omega = 0$. These particular modes are responsible for the major differences between the disordered mass-spring lattice and the KG lattice where such extended modes are absent as we will see below. In Fig. 2.15, we show some examples of the profiles of certain modes for the disorder lattice. It is readily observed that a low frequency mode such as the one in Fig. 2.15(a) is extended throughout the lattice, while on the opposite side a high frequency mode such as the one of panel (c) is very localized.

2.4.1.1 Projections of singe site states onto the normal modes

As explained in the previous paragraph, when disorder is introduced into the system, a significant number of the eigenmodes become exponentially localized. In that sense

a single site state vector as the one defined in Eqs. (2.31) or (2.33) will have different behavior than in the homogeneous case. In Fig. 2.16, the average energy acquired by each mode assuming a single site state vector for both displacement and momentum is shown for a lattice of $N = 10^3$ masses for 500 disorder realizations.

The first observation is that in contrast to the results of the homogeneous case (see Fig. 2.5), here on average the high frequency modes (large k) are less excited. This is understood since most of the high frequency modes are very localized in random positions and by exciting only the middle particle in the lattice, there is a very small probability that such a mode is excited. On the other hand, even with disorder the low frequency modes remain extended and are more excited than the higher frequency modes. However, the difference between the single site displacement and momentum excitations in the low frequency is still valid, i.e., the single site [panel (b)] displacement excites less the low frequency modes (small values of k).

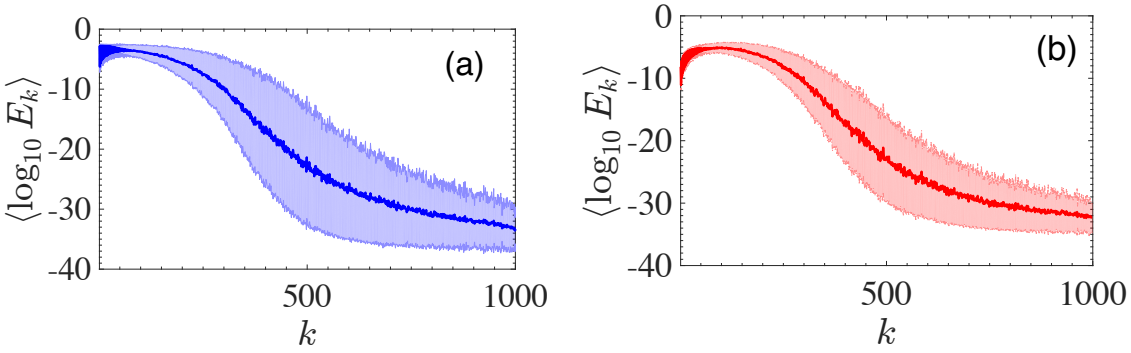

Fig. 2.16. Average energy per mode for single site initial (a) momentum and (b) displacement excitations onto the eigenmodes of the mass-spring system. The index k takes the ordered modes from lowest frequency (low k values) to high frequency (high k values). The averages were taken over 500 disorder realizations and the lighter shaded areas represent statistical error.

2.4.2 Dynamical properties.

The dynamics of the disorder lattice are now studied by integrating the system of equations Eq. (2.41) for sufficiently large lattices using single site initial conditions for all realizations. The final integration time is chosen such as to avoid reflections on the boundaries.

2.4.2.1 Energy density profiles and snapshots

First we show the spatiotemporal evolution of the energy density for two representative disorder realizations in Fig. 2.17 for momentum (a) and displacement (b) single site initial excitations. For both types of initial excitations, there is a localized portion of the total energy which remains around the excitation point and also a propagating front which with ballistic peaks in both cases. The ballistic peaks are due to the extended modes which are excited for both momentum and displacement excitations as described in Section. 2.4.1.1.

This is a direct result of localization due to disorder, since by exciting a single site in the center we are exciting mostly the localized modes around that region. In addition since (as it was shown by the projections on the modes) there are always some extended modes that are also excited, thus some amount of energy is able to spread throughout the lattice. In Figs. 2.17(b) and (d) we show the average (over 1000 realizations) energy profiles for two different time instances. In Ref. [55], it has been shown that the energy density exhibits a specific profile $\langle h_n \rangle \propto |n - n_0|^{-\nu}$ with $\nu = 3/2$ for the initial momentum and $\nu = 1/2$ for the initial displacement.

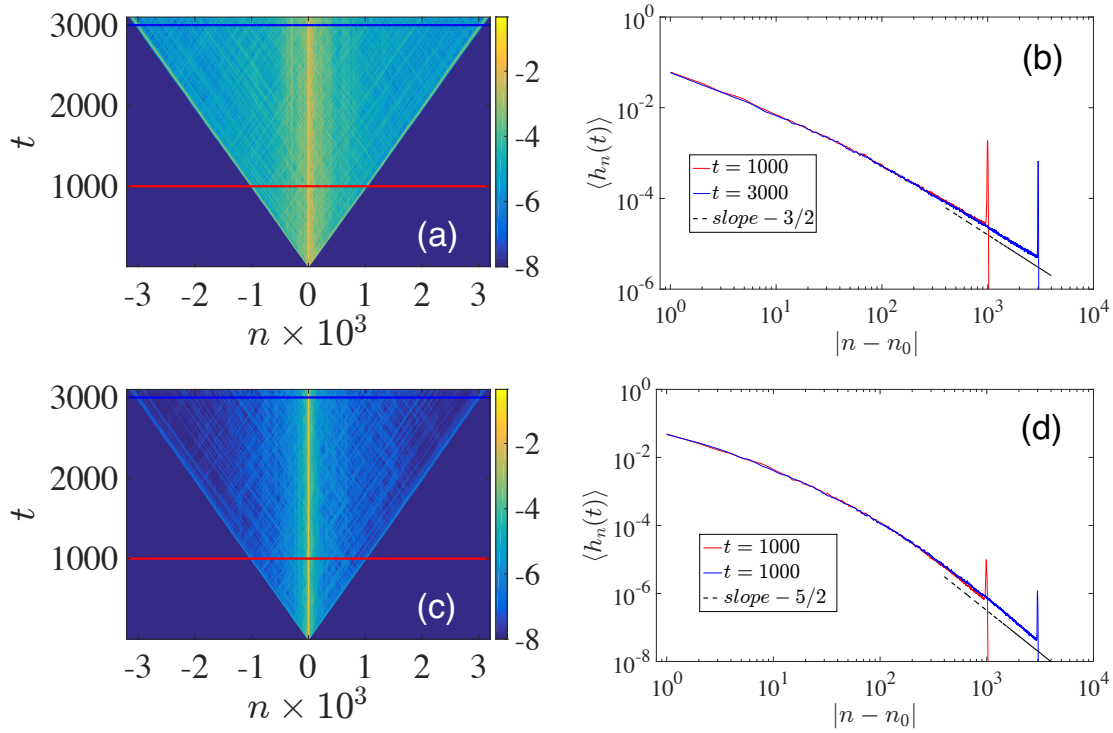

Fig. 2.17. (a) A representative spatiotemporal evolution of energy density for a disordered mass-spring system with parameters $K = 1$ and $\langle m_n \rangle = 1$ for momentum initial condition. The color bars are in logarithmic scale. (b) Energy density snapshots are taken at $t = 1000$ shown by the red dashed line in (a) and $t = 3000$ as shown by the blue dashed line in (a). The results for displacement initial conditions are shown in (c) and (d) and the averaged values of $\langle h_n(t) \rangle$ are taken over 1000 disorder realizations and with lighter shaded areas representing the statistical error.

2.4.2.2 Time evolution of P, m_2 and β

The time evolution of $\langle P \rangle$ reaches some finite values for both cases as depicted in Fig. 2.18(a) in sharp contrast to the the power law spreading behavior of the homogeneous chain. In a similar manner, the $\langle m_2 \rangle$ also slows down from ballistic to superdiffusive and subdiffusive spreading for momentum and displacement initial excitations respectively. as shown in Figs. 2.18(b) and (c). Note that the asymptotic values of β for both cases have been analytically obtained in both Refs. [54] and [55] and were found to be $\beta = 1.5$ and $\beta = 0.5$ for initial momentum and displacement excitations respectively.

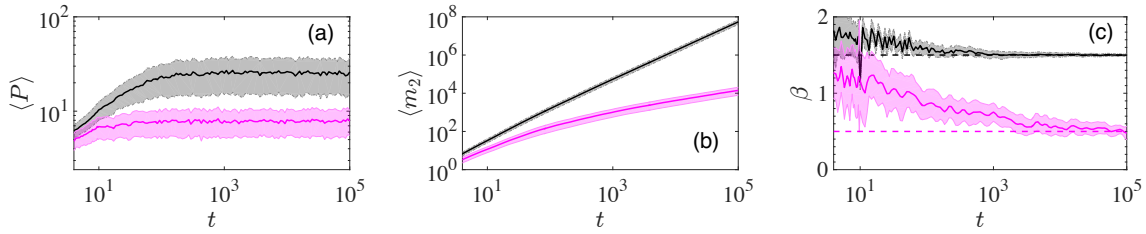

Fig. 2.18. Time evolution of (a) $\langle P \rangle$ (b) $\langle m_2 \rangle$ and (c) β for the disordered mass-spring system. The averaged values are taken over 100 disorder realizations and the lighter shaded areas represent statistical error.

2.5 Disordered linear one-dimensional discrete Klein-Gordon lattice

2.5.1 Spectral properties

Returning to the already discussed KG lattice in Section. 2.3 we now also introduce disorder to the system by assuming that m_n are chosen randomly. The Hamiltonian is now written as

$$H = \sum_n \frac{1}{2}\pi_n^2 + \frac{1}{2}(\phi_{n+1} - \phi_n)^2 + \frac{1}{2}m_n\phi_n^2. \tag{2.43}$$

For a finite KG lattice, it is again possible to numerically obtain the linear spectrum. In order to do so, we consider a finite lattice of size N and assume harmonic solutions of the form $\mathbf{\Phi}(t) = \mathbf{\Phi}e^{i\omega t}$, where $\mathbf{\Phi}$ is a column matrix with elements ϕ_n, $n = 1, 2, 3, \ldots, N$ for a finite lattice. The resulting corresponding eigenvalue problem

$$-\omega_k^2\mathbf{\Phi}_k = \mathbf{K}(m_n)\mathbf{\Phi}_k, \tag{2.44}$$

is then solved. As an example, we chose m_n from a random uniform distribution such that $m_n \in [0.1, 1.9]$.

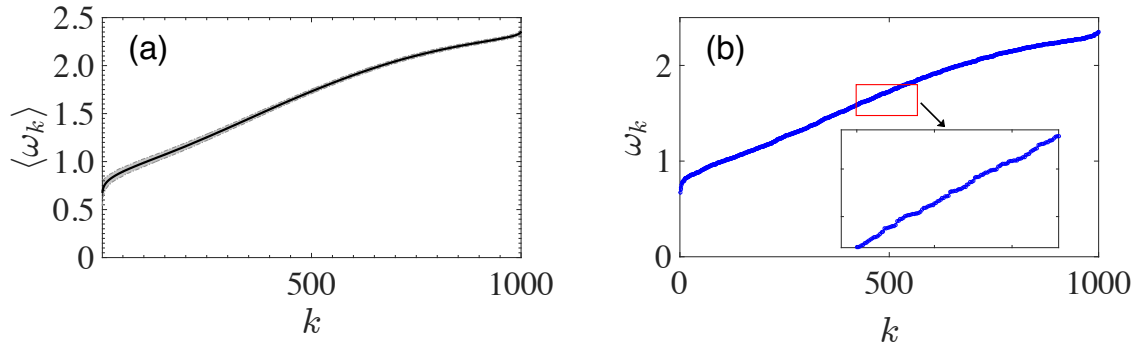

Fig. 2.19. (a) Averaged frequency spectrum over 500 disorder realizations for a disordered KG lattice. The index k takes the ordered modes from lowest frequency (low k values) to high frequency (high k values) and the lightly shaded areas indicate statistical error. (b) Eigenfrequencies of a randomly chosen representative realization of a disordered discrete KG lattice. The inset depicts a zoom of the area inside the (red) rectangle.

The averaged frequency spectrum is gaped and the allowed frequencies increase beyond $\sqrt{m+4}$ in contrast to ordered KG system whose dispersion relation only allows frequencies within the range $[\sqrt{m}, \sqrt{m+4}]$. In Fig. 2.19 we show the disordered KG lattice's averaged frequency spectrum. The gap is reduced when disorder is introduced as some frequencies are allowed below $\sqrt{m}$.

Examples of three different modes taken from a particular disorder realization are shown in Fig. 2.20. It is found that all the modes in the system are localized. In fact, it is known that the eigenvalue problem of the disorder KG lattice can be directly mapped [74, 75, 76] to the well known Anderson model [1]. Thus, when the disorder strength is chosen to be large enough (such that the localization length [73, 77] is smaller than the system size) all modes of the lattice are localized. This is is the fundamental difference between the disordered lattices discussed in this Section.

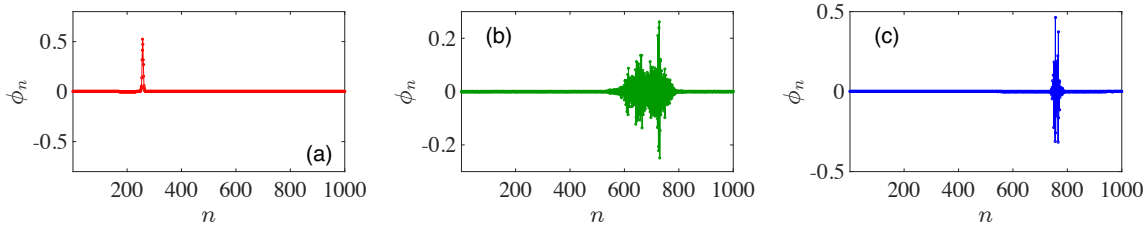

Fig. 2.20. Profiles of (a) mode 2 (b) mode 500 and (c) mode 900 for a representative disordered harmonic lattice of size 100. The averaged quantities are taken over 100 disorder realizations.

2.5.2 Dynamical properties

To further illustrate that the system undergoes Anderson localization we also study its dynamics using single site initial excitations.

2.5.2.1 Energy density profiles

As shown in panels (a) and (b) of Fig. 2.21, the wave-packet spreads for an initial transient time up to the localization length of the disordered lattice. The wave-packet then stops spreading and remains localized thus no further energy spreading.

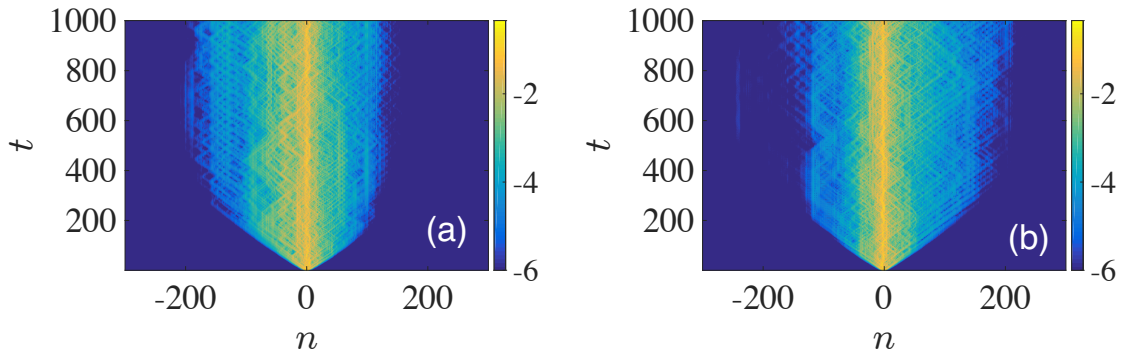

Fig. 2.21. The energy density profiles for some representative disorder realizations of the disordered KG lattice for initial (a) momentum and (b) displacement excitations. The color bars are in logarithmic scale.

2.5.2.2 Time evolution of P, m_2 and β

For completeness in Fig. 2.22 we show the indicators $\langle P\rangle$, $\langle m_2\rangle$ and β for the disordered KG lattice. As expected, the energy remains localized and the participation number reaches a finite asymptotic value. The the second energy moment stops growing after a transient time resulting in a vanishing exponent β.

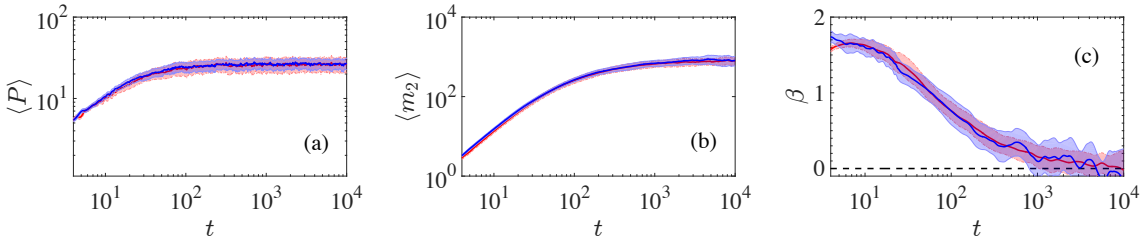

Fig. 2.22. Time evolution of (a) $\langle P\rangle$ (b) $\langle m_2\rangle$ and (c) β for the disordered KG lattice.

2.6 Disordered classical nonlinear lattices

A well known result is that for linear disordered systems, energy excitations of eigenstates remain localized (AL). AL has also been observed experimentally [18, 22, 26, 24]. The fate of localized modes in disordered systems under the effect of nonlinearity in disordered systems has attracted tremendous research interest in the past decade from theoretical and numerical viewpoints [78, 53, 79], to complement experiments [19, 23, 14]. One of the fundamental questions which has puzzled researchers in this context is what happens to energy localization in the presence of nonlinearities.

Extensive numerical studies on the effect of nonlinearity to the propagation of initially localized energy excitations in disordered variants for many spatial dimensions have been mainly concentrated on the discrete KG chains and the DNLS equation. From several of these studies, statistical characteristics of energy spreading have been determined and showed that nonlinearity destroys AL [31, 30, 80, 81]. A common denominator in many of these studies has been the establishment of several dynamical spreading regimes such as the so-called weak and strong chaos regimes. In addition to the identification of these regimes, several follow up theoretical works have cast more light on the dynamical characteristics and appearances of these regimes. In particular, it is now generally accepted that nonlinearity leads to the subdiffusive spreading of wave-packets after the initial predictions were experimentally validated in [82].

From a quantitative point of view, for 1D lattices, the wave packet's m_2 grows in time t as $m_2 \propto t^{\beta}$. For the weak and strong chaos regimes the exponents of m_2 are $\beta = 1/3$ and $\beta = 1/2$ respectively. Energy spreading in disordered lattices energy spreading in disordered lattices is commonly identified as a chaotic process, the characteristics of this chaotic behavior are yet to be systematically understood in detail. An early attempt to achieve this goal in 1D disordered nonlinear lattices was made in [34, 35] for the weak chaos regime. In this study study, the authors made an attempt to study in detail the weak chaos regime of the KG model. The weak chaos regime was also

shown to have the characteristics of slowing down of the dynamics which however do not cross over into regular dynamics. A further insight provided by that work has been the numerical evidence of the existence of chaotic hot spots in disordered lattices where few lattice sites seem to behave more chaotically than others and meander throughout the system as time evolves, sustaining the chaoticity. The work in [35] has been further extended to 2D disordered lattices in [71] where the the energy transport and chaotic behavior was characterized.

Chapter 3

Hertzian versus the Fermi-Pasta-Ulam-Tsingou model

Contents

3.1 Contact forces in the granular chain

In this chapter, whose contents are based on the published article [83], we make use of granular crystals to study the role of different nonlinearities in the destruction of Anderson localization, the system's chaoticity and also energy equipartition in a 1D lattice. It is thus instructive to first present the main properties of a periodic granular chain before proceeding to the more complicated structure of a disorder lattice. In granular crystals, the interactions between the elastic particles appear due to their contacts. The forces at the contact points are described here considering only normal forces and are also shown schematically in Fig. 3.1.

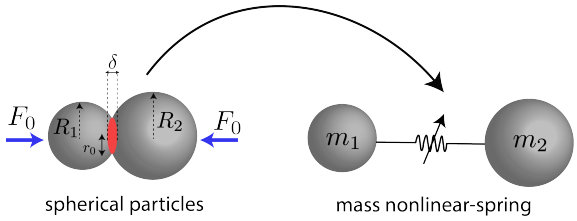

Fig. 3.1. A schematic showing how two spherical particles in contact and under a pre-compression force of magnitude F_0 can be described by a mass-spring system with nonlinear stiffness.

One of the main assumptions of the Hertz-Mindlin theory, which we use here, is that the contact area between two elastic spheres is small compared to their radii and the area in contact is considered to be elliptical (see Fig. 3.1). The radius of the contact surface is therefore written as

$$r_0 = \Big(\frac{3R^* F_0}{4E^*}\Big)^{1/3}, \tag{3.1}$$

where $1/R^* = 1/R_1 + 1/R_2$ and $1/E^* = (1-\nu_1^2)/E_1 + (1-\nu_2^2)/E_2$ where 1 and 2 refer to the two different spherical particles. Here E is the Young's modulus and ν the Poisson's ratio for each sphere. By making use of these relations, we may write the deformation of the particles to be

$$\delta_0 = \Big(\frac{3F_0}{4E^*\sqrt{R^*}}\Big)^{2/3}. \tag{3.2}$$

The importance of Eq. (3.2) lies in the fact that it reveals the nonlinear dependence of the center of mass displacement and the magnitude of the pre-compression force F_0. This stress/strain nonlinear relation arises solely due to the geometry of the particles and vanishes when the compression force diminishes. It is exactly this force that makes granular crystals a versatile system to study the transitions from linear to strongly nonlinear wave dynamics tuned by the ratio between the static overlap δ_0 when the system is in equilibrium and the displacement of the spheres when oscillating. In fact, the granular lattice can be tuned to behave like (a) a mass spring system in the linear limit (b) like an FPUT lattice in the weakly nonlinear regime and (c) most importantly it has discontinuous nonlinearity in the strongly nonlinear regime. One of the main goals in this chapter is to identify the mechanisms that lead to energy spreading of an initially excited localized mode in granular chains.

In this chapter, we exploit this property of the granular crystal to compare it with the FPUT model regarding their properties when both disorder and nonlinearity are present. In particular, the main interest here is to study the fate of strongly localized modes, which appear due to disorder, and focus on the role of discontinuous nonlinearities on the dynamics. In the first section, a statistical analysis of the linear limit, which is common for both models, shows that for sufficiently strong disorder, the system acquires a significant number of strongly localized, almost single particle, modes. From this ensemble a representative realization was chosen to illustrate its nonlinear behavior. Additionally, chaos indicators are used to quantify the system's chaotic behavior. Chaos propagation information in the lattice aids the differentiation of localized and extended chaos. By tracking the mode distribution during the dynamics' evolution, it is possible to glean some insights regarding equipartition.

3.2 Hertzian and FPUT models with disorder

For the rest of this chapter, we study a granular chain using a Hertzian model and a power series approximation of the Hertzian model which leads to the FPUT model. The total energy for a chain with N spherical homogeneous beads of radius R_n and mass m_n ($n = 1, 2, 3, \ldots, N$) is given by the following Hamiltonian (see Fig. 3.2),

$$H = \sum_{n=1}^{N} H_n = \sum_{n=1}^{N} \frac{p_n^2}{2m_n} + V_n^{(Hz,F)}. \tag{3.3}$$

Here, $p_n = m_n \dot{u}_n$ and u_n denote respectively the momentum and displacement from equilibrium for each particle, $\dot{(\cdot)}$ denotes the first order time derivative, while the random radii R_n are uniformly chosen in the interval $[\min(R_n), \max(R_n)]$.
The Hertzian potential V_n^{Hz} for each bead due to the nearest neighbor coupling is defined as $V_n^{Hz} = [V^{Hz}(u_n) + V^{Hz}(u_{n+1})]/2$ where,

$$V^{Hz}(u_n) = \frac{2}{5} A_n [\delta_n + u_{n-1} - u_n]_+^{5/2} - \frac{2}{5} A_n \delta_n^{5/2} - A_n \delta_n^{3/2} (u_{n-1} - u_n). \tag{3.4}$$

The static overlap δ_n between two neighboring beads $n-1$ and n is given by $\delta_n = (F_0/A_n)^{2/3}$ where F_0 is the magnitude of the pre-compression force. The coefficient A_n for spherical beads is given as $A_n = (2/3)\varepsilon\sqrt{R_{n-1}R_n/(R_{n-1}+R_n)}/(1-\nu^2)$ where ε and ν are the elastic modulus and the Poisson ratio respectively [84]. The plus sign in $[\cdot]_+$ describes the fact that this term is present as long as $\delta_n + u_{n-1} - u_n > 0$ and is absent otherwise, since then the particles are no longer in contact. This is the non-smooth nonlinearity which substantially differentiates the two models.

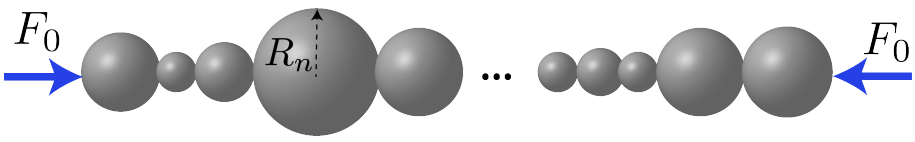

Fig. 3.2. A schematic showing how a pre-compressed granular chain with random radius.

The FPUT model is described by Eq. (3.3) with a potential

$$V^F(u_n) = \sum_{k=2}^{4} K_n^{(k)} (u_n - u_{n-1})^k. \tag{3.5}$$

Accordingly, the potential of the n^{th} particle is written as $V_n^F = [V^F(u_n) + V^F(u_{n+1})]/2$. For the rest of this chapter a chain of $N = 40$ particles is considered. For the numerical simulations, units corresponding to a mean radius of $\bar{R} = 0.01$m, and a static pre-compression force $F_0 = 1$N were chosen. The mean radius is used as a reference to the uniform system with particles of radius $R = (\alpha + 1)\bar{R}/2$. The disorder strength, is quantified by the parameter $\alpha = \max(R_n)/\min(R_n)$. This choice of disorder naturally leads to a random distribution of both the masses and stiffness coefficients [85]. In all calculations, the use of fixed boundary conditions with fixed beads on both ends such that $u_0 = u_{N+1} = 0$ and $p_0 = p_{N+1} = 0$ is employed. The corresponding equations of motion for the Hertzian model Eq. (3.4) are

$$m_n \ddot{u}_n = A_n [\delta_n + u_{n-1} - u_n]_+^{\frac{3}{2}} - A_{n+1} [\delta_{n+1} + u_n - u_{n+1}]_+^{\frac{3}{2}} \tag{3.6}$$

while for the FPUT model we obtain

$$m_n \ddot{u}_n = \sum_{k=2}^{4} \left[K_{n+1}^{(k)} (u_{n+1} - u_n)^{k-1} - K_n^{(k)} (u_n - u_{n-1})^{k-1} \right]. \tag{3.7}$$

A direct connection between the two models is made by taking the Taylor series expansion of Eq. (3.4) up to fourth order (assuming small displacements) $u_n/\delta_{n,n+1} \ll 1$. Doing so we recover Eq. (3.7) with coefficients $K_n^{(2)} = (3/2)A_n\delta_n^{1/2}$, $K_n^{(3)} = -(3/8)A_n\delta_n^{-1/2}$ and $K_n^{(4)} = (3/48)A_n\delta_n^{-3/2}$ [86]. Below all the units are normalized such that for the linear homogeneous chain with $\alpha = 1$, the frequency cut-off is $\omega_{\max} = \sqrt{\frac{4K}{m}} = 1$ with $K = K_n^{(2)}$ and $m = m_n = 1$.

3.2.1 Linear mode analysis of the disordered chain

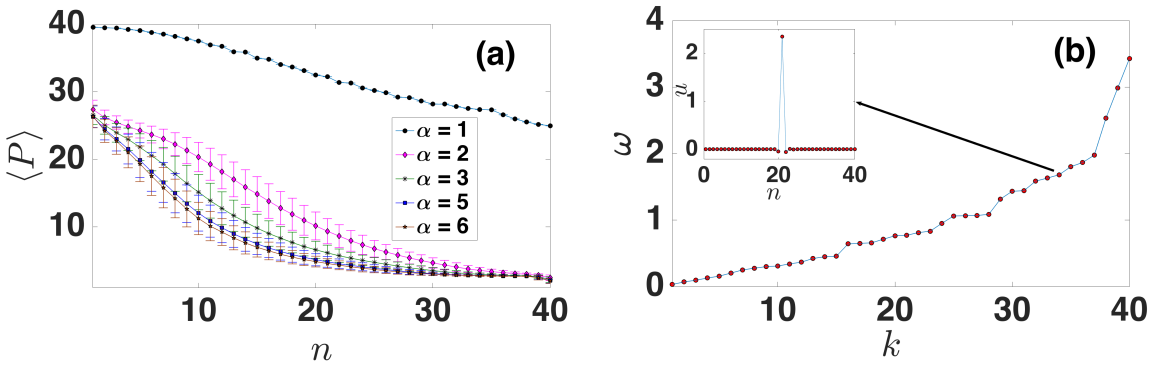

Fig. 3.3. (a) Mean (over 1000 disorder realizations) participation number $\langle P \rangle$ of the eigenmodes for varying disorder strengths α, sorted in descending order k for each realization. The standard deviation at each point is shown by the error bars. (b) The eigenfrequencies of a particular disordered chain of 40 sites for $\alpha = 5$ sorted by increasing frequency. The inset shows the profile of the 34^{th} mode.

In this chapter, the main interest is on the fate of strongly localized modes thus it is important to first identify the sufficient disorder strength able to sustain a significant amount of localized modes. To do so, a statistical analysis of the linearized equation of motion

$$m_n \ddot{u}_n = K_{n+1}^{(2)}(u_{n+1} - u_n) - K_n^{(2)}(u_n - u_{n-1}) \tag{3.8}$$

which is common for both models was done. Assuming harmonic solutions of the form $\mathbf{U}(t) = \mathbf{U_0} e^{i\omega t}$, where $\mathbf{U}_0$ is a column matrix with elements U_n, $n = 1, 2, 3, \ldots, N$. The following corresponding eigenvalue problem was then solved

$$-\omega^2 \mathbf{M}\mathbf{U_0} = \mathbf{K}\mathbf{U_0}. \tag{3.9}$$

The matrix $\mathbf{M}$ is a diagonal matrix with elements m_n and $\mathbf{K}$ is a sparse diagonal matrix containing the stiffness coefficients $K_n^{(2)}$. In Fig. 3.3(a), the mean value $\langle P \rangle$ of the participation number of the eigenmodes for different disorder strengths is shown, using an ensemble of 1000 disorder realizations. The modes are sorted with descending values of P for each realization. For relatively weak disorder (e.g. for $\alpha = 2$) $\langle P \rangle$ largely deviates for the homogeneous case ($\alpha = 1$) and some localized modes appear in the system. On the other hand for values of $\alpha \geq 4$ the averaged participation number reaches a limiting curve with about 10 strongly localized modes with $\langle P \rangle \approx 2$. The above analysis, provides clear evidence that a single disorder realization with $\alpha = 5$ is sufficient for the chain to possess several strongly localized modes.

Here, we make use of the DVDs in order to spatially characterize the chaoticity of the system, either as localized or extended chaos. The initial condition used for the deviation vectors $\vec{v}(0)$ is a random uniform distribution of momentum perturbations δp_i as for this choice, the time evolution of the finite time mLE was found to converge faster to the $\Lambda(t) \propto t^{-1}$ law for regular orbits.

The numerical results shown in the rest of this work (unless stated otherwise), are performed using a representative single realization of the statistical ensemble for $\alpha = 5$. The corresponding eigenfrequencies of this realization are shown in Fig. 3.3(b). Generally, low frequency modes extend over many particles, whilst high frequency modes are localized. The 34^{th} mode is easily identified to be a strongly localized mode ($P \approx 2.5$) located in the middle of the chain at site $n = 21$ as shown in the inset of Fig. 3.3(b). To study the effect of nonlinearity, the 21^{st} site is excited which results in the excitation of almost only the 34^{th} mode, and we monitor the evolution of both models as we increase the initial excitation energy.

3.3 Dynamical evolution of an initially localized mode

3.3.1 Near linear limit

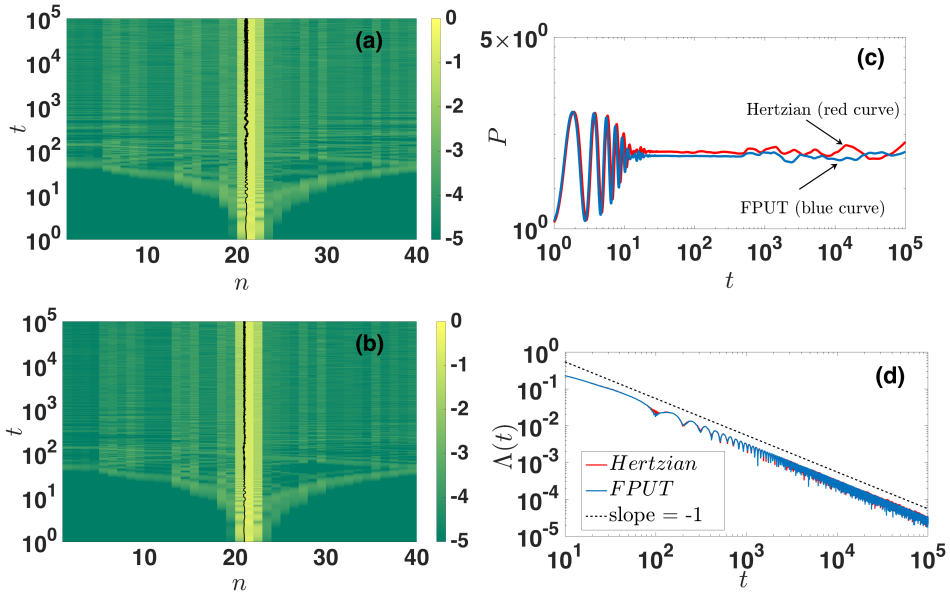

Fig. 3.4. (a) and (b) The spatiotemporal evolution of the energy distribution for the Hertzian and FPUT chains respectively for $H = 0.25$. The black curves indicate the running mean position of the energy distributions. The color bars on the right sides of (a) and (b) are in logarithmic scale. (c) The locally weighted smoothed values of P as a function of time for the Hertzian chain (red curve) and the FPUT chain (blue curve). (d) The time evolution of $\Lambda(t)$ for the Hertzian chain (red curve) and the FPUT chain (blue curve). Both lines practically overlap and the dashed line indicates the law $\Lambda(t) \propto t^{-1}$.

For sufficiently small energies H, we have numerically confirmed that the two models behave both qualitatively and quantitatively the same. An example is given in Fig. 3.4 which corresponds to $H = 0.25$. As shown in panels (a) and (b) the energy density for both models is completely localized around the initially excited site $n = 21$ as shown by the black solid line which indicates the mean position of the energy distribution. Localization is quantified by the almost constant value of $P \approx 1.8$ for both models, shown in Fig. 3.4(c). The curves of the Hertzian (red) and the FPUT (blue) models almost overlap. The time evolution of $\Lambda(t)$ is depicted in Fig. 3.4(d) and confirms that the dynamics is regular as $\Lambda(t)$ follows the power law $\Lambda(t) \propto t^{-1}$.

The spatiotemporal evolution of the corresponding DVD, plotted in Figs. 3.5(a) and (b), exhibits an extended deviation vector distribution in contrast to the localized, pointy shape that DVDs exhibit for chaotic orbits [34, 35, 87]. Accordingly, particular profiles of the DVDs taken at different times shown in Figs. 3.5(c) and (d) are found to be extended covering the whole excited part of the lattice in a relatively smooth way.

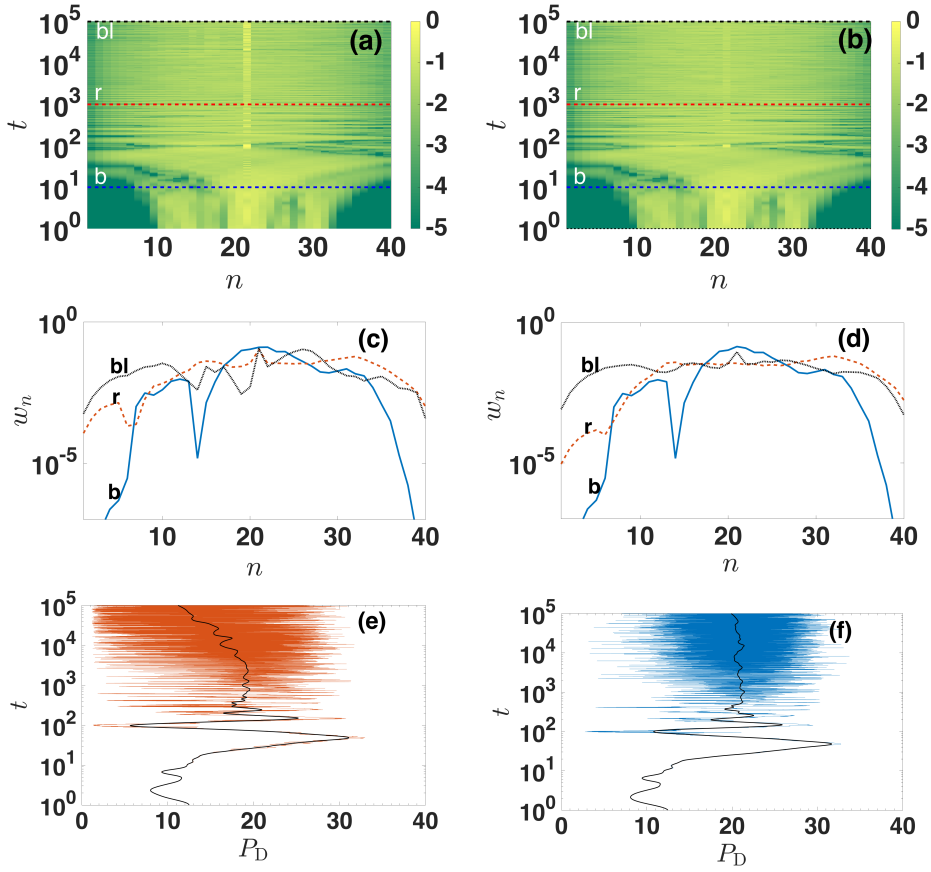

Fig. 3.5. (a) [(b)]: The spatiotemporal evolution of the deviation vector density (DVD) for the Hertzian [FPUT] disordered chain. The color bars on the right sides of (a) and (b) are in logarithmic scale. (c) [(d)]: Deviation vector profiles for three time instances of $t \approx 10^1$ indicated by the blue (b) curve, $t \approx 10^3$ indicated by the red (r) curve and $t \approx 10^5$ indicated by the black (bl) curve. These times correspond respectively to the blue, red and black horizontal lines in panel (a) [b]. (e) [(f)]: The time evolution of the participation number P_D of the DVD for the Hertzian [FPUT] model. All results are obtained for $H = 0.25$.

However, a difference between the two models is found by closely inspecting the corresponding participation number P_D of the DVDs shown in Figs. 3.5(e) and (f). This quantity is calculated in a similar way as the energy density and it gives the number of sites that are significantly participating in the dynamics of the DVD. In Figs. 3.5(e) and (f) we observe that although up to $t \approx 10^3$ both DVDs exhibit approximately $P_\mathrm{D} \approx 20$, for the case of the Hertzian chain [panel (e)] it starts to drop to a smaller value. As discussed earlier, the tendency of the DVD to start to localize is a precursor of a chaotic spot that may appear in the dynamics over a longer timescale.

It is interesting to note that, although the two models behave almost identically for $H = 0.25$, this energy corresponds for the Hertzian model to an initial displacement of $u_{21}(0) = 1.01$ with the neighboring static overlaps being $\delta_{21,22} \approx 1.06$. These values are far from the small amplitude approximation ($u_n/\delta_{n,n+1} \ll 1$). The two models however

show no differences (at least for the studied time scales), mainly due to the fact that practically only a single mode is participating in the dynamics.

3.3.2 Chaos and destruction of localization

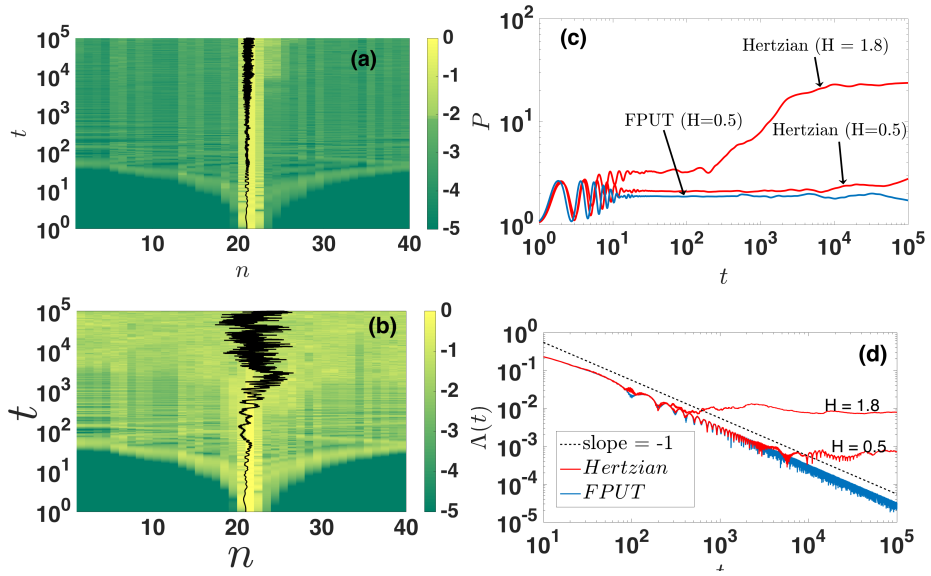

Fig. 3.6. Panels (a) and (b) show the spatiotemporal evolution of the energy distribution for the Hertzian model with $H = 0.5$ and $H = 1.8$ respectively. Black curves indicate the running mean position of the energy distributions. The colorbars on the right sides of (a), (b) are in logarithmic scale. Panels (c) and (d) are the same as Figs. 3.4(c) and (d); for the Hertzian model $H = 0.5$, $H = 1.8$ and for the FPUT model with $H = 1.8$.

3.3.2.1 Energy density evolution and chaos

In Fig. 3.6(a) we show the energy density evolution for the Hertzian model with energy $H = 0.5$. The energy distribution for both models [results for the FPUT are similar to Fig. 3.4(b)], is still localized for $H = 0.5$. However, there is a difference during the last decade, better captured by the evolution of P as illustrated in Fig. 3.6(c), since the Hertzian chain exhibits a tendency to increase the number of highly excited particles.

The most intriguing feature for this particular case is found in the system's chaoticity as quantified by the time evolution of $\Lambda(t)$ shown in Fig. 3.6(d). The red solid line, which corresponds to the Hertzian chain with $H = 0.5$, deviates from the $\Lambda(t) \propto t^{-1}$ curve, at the last decade, and attains an almost constant value. This signals that the system is chaotic. In contrast, for the same energy the FPUT model's orbit remains regular. The Hertzian model therefore exhibits localized chaos whilst the FPUT model is localized and regular.

In Fig. 3.6(b) we show that initially localized wave-packet for the Hertzian model at $H = 1.8$, gradually spreads throughout the lattice signaling the destruction of Anderson localization. In particular, up to $t \approx 2 \times 10^2$ the wave-packet remains localized [see Figs. 3.6 (b) and (c)] with a participation number $P < 3$, it then rapidly spreads until

$t \approx 4 \times 10^3$. At the last decade the participation number saturates to a value $P \approx 26$. This is the maximum observed value of P in all our simulations. According to the corresponding $\Lambda(t)$ shown in Fig. 3.6(d) for $H = 1.8$, the system also becomes chaotic as early as $t \approx 2 \times 10^2$ acquiring an almost constant positive value of $\Lambda(t) \approx 10^{-3}$. Results for the FPUT are not shown for this energy since excitations were still found to be localized and regular.

It is important to note here that for the particular single site excitation, all energies $H > 1.8$ lead to a final chaotic and delocalized state. This suggests the appearance of an energy threshold beyond which the final state of the Hertzian model is delocalized and chaotic. Below we show that this is true for different modes of this realization but also for different realizations.

3.3.2.2 Spatiotemporal evolution of chaos

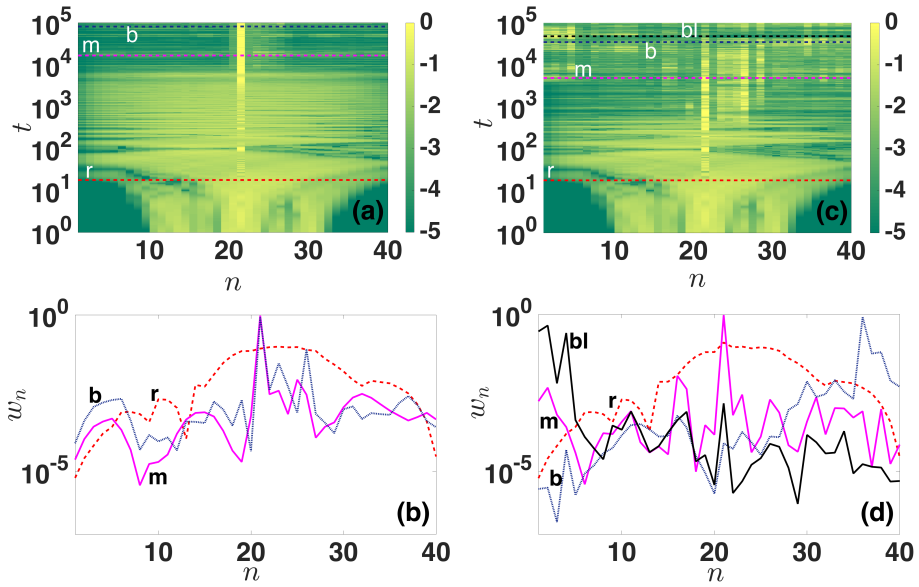

Fig. 3.7. Panel (a) shows the spatiotemporal evolution of the DVD for the Hertzian model at $H = 0.5$ whilst panel (b) shows the profiles of the DVDs at $t \approx 1.7 \times 10^1$ red (r) curve, $t \approx 1.7 \times 10^4$ magenta (m) curve and $t \approx 8.2 \times 10^4$ blue (b) curve. (c) Same as (a) but for $H = 1.8$. (d) Same as (b) but for $H = 1.8$ at $t \approx 1.7 \times 10^1$ red (r) curve, $t \approx 4.9 \times 10^3$ magenta (m) curve, $t \approx 3.5 \times 10^4$ blue (b) curve and $t \approx 4.8 \times 10^4$ black (bl) curve. The color bars in (a) and (c) are in logarithmic scale.

In order to better understand the onset of chaos in the aforementioned cases, we study more closely the behavior of the DVDs. In Figs. 3.7(a) and (c) we plot the DVDs for the Hertzian model for $H = 0.5$ and $H = 1.8$ respectively. Focusing on the case of $H = 0.5$ we see that initially, when the system behaves regularly, the DVD exhibits an extended smoothed profile. This is more clearly seen by the red (dotted) curve in Figs. 3.7(b). Thereafter, during a period up to $t \approx 4 \times 10^3$ the DVD gradually converges around site $n = 21$. A profile of the DVD in this era is shown with the magenta curve in Fig. 3.7(b). Finally for the rest of the simulation the profile of the DVD is strongly

localized around site $n = 21$ as also confirmed by two different profiles during the last decade shown in Fig. 3.7(b). Other recent studies (i.e. Refs. [34, 35, 87]) also used the DVD to spatially characterize chaos. In these works, it was found that the profile of the DVD exhibits a peak that oscillates within a chaotic region, while in our case it remains attached to a single site indicating strongly localized chaos.

At a higher energy of $H = 1.8$ the DVD initially exhibits an extended and smooth profile and an example is plotted in Fig. 3.7(d) with the red (dotted) line. Further on, it concentrates around a region close to the center of the chain and beyond this point the system is chaotic. The evolution of the DVD during this chaotic era, is characterized by one dominant peak along with other smaller peaks usually two orders of magnitude smaller (at most) as illustrated in Fig. 3.7(d). We particularly choose three cases where the dominant peak is either at the center (magenta), closer to the right edge (blue) or at the left edge (black). This is to emphasize the fact that for this energy, the chaoticity of the system is extended featuring strongly chaotic spots throughout the whole lattice. Here we would like to stress the importance of the DVD which enables us to differentiate between localized and extended chaos.

3.3.2.3 Chaos and delocalization for the FPUT model

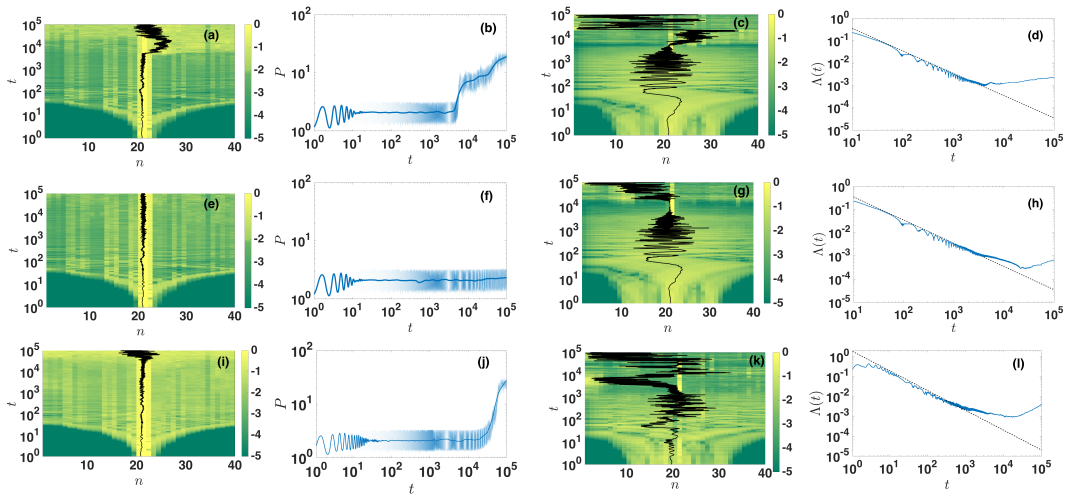

Fig. 3.8. (a), (b), (c) and (d) depict the energy density, P, DVD, and $\Lambda(t)$ respectively for the FPUT with $H = 2.9$. The second, and third rows correspond to energies $H = 4$ and $H = 8.7381$ respectively. The color bars on the right sides of panels (a), (c), (e), (g), (i) and (k) are in logarithmic scale.

In contrast to the Hertzian model, the dynamics for the FPUT model appears to remain localized and regular up to an energy excitation of $H = 1.8$ [see Figs. 3.6 (c) and (d)]. The first energy at which the FPUT model's wave-packet is delocalized, exhibiting also a chaotic behavior, is around $H = 2.9$ (first row of Fig. 3.8). After an initial transient time for which the wave-packet remains localized, in the last decade of the simulation, it eventually spreads as shown by the energy density and P in Figs. 3.8(a) and (b) respectively.

The time evolution of $\Lambda(t)$ shown in panel (d) significantly deviates from the $\Lambda(t) \propto t^{-1}$ line, indicating chaotic dynamics for $t \gtrsim 4 \times 10^3$. Furthermore the DVD shown in Fig. 3.8(c) exhibits peaks at different places within the lattice when the system is chaotic, similarly to Fig. 3.7(c) for the Hertzian model, which is associated with extended chaos.

The most striking difference between the two models is found by examining higher energy excitations. To our surprise, we found that increasing the energy for the FPUT model does not necessarily lead to delocalization. In other words there isn't an energy threshold beyond which the final state of the FPUT lattice is delocalized. For example, as shown in the second row of Fig. 3.8; for $H = 4$ the excited wave-packet remains well localized and the participation number hardly changes [compare Figs. 3.8(a) and (b) with Figs. 3.8(e) and (f)]. This is somewhat a surprising result and it highlights the complexity of the phase-space of a disordered FPUT lattice. We could qualitatively describe the results for the FPUT model as alternating between spreading and localization as the energy increases. To better visualize this alternate behavior, an example for $H = 8.7381$ in the bottom row of Fig. 3.8 is shown, which exhibits a delocalized and chaotic final energy profile. For this energy, the system behaves qualitatively the same as in the first row with $H = 2.9$.

Regarding chaoticity, the dynamics of the DVDs are shown in the third column of Fig. 3.8. For all cases, the initially localized DVD around $n = 21$ finally departs from this site and it oscillates within the lattice. Accordingly, $\Lambda(t)$, shown in the last column of Fig. 3.8, initially follows the regular orbit slope but eventually signals chaotic dynamics by diverging from this line and acquiring a non-zero value. We have found that for all $H > 2.8$, the final state of the lattice is always chaotic irrespectively of the localized or delocalized nature of the wave-packet.

3.3.3 Role of the non-smooth nonlinearity and energy equipartition

In order to further track down the mechanisms responsible for the different behaviors between the two models we monitor the appearance of the non-smooth nonlinearity [i.e., whenever $(u_n - u_{n-1}) > \delta_n$] for the Hertzian model, or in other words the appearance of gaps. Fig. 3.9(a), shows the position of gaps for the case $H = 0.5$, which corresponds to the panels of the first row of Fig. 3.6. We clearly see that on the left and right side of site $n = 21$ a gap often opens during the system's evolution triggering the appearance of the non-smooth nonlinearity.

At this energy no more than one gap is open at any instant as observed in Fig. 3.9(c) where the total number of gaps as a function of time is plotted. Importantly, since for this energy the dynamics of both the Hertzian and FPUT models is equivalent, but the Hertzian model appears to be chaotic, we identify the non-smooth nonlinearity around $n = 21$ as the ingredient which induces chaos for the Hertzian model.

For the energy $H = 1.8$ shown in Fig. 3.9(b), we find that more gaps start to open"moving" away from site $n = 21$, covering eventually the whole lattice. In fact, for the energy

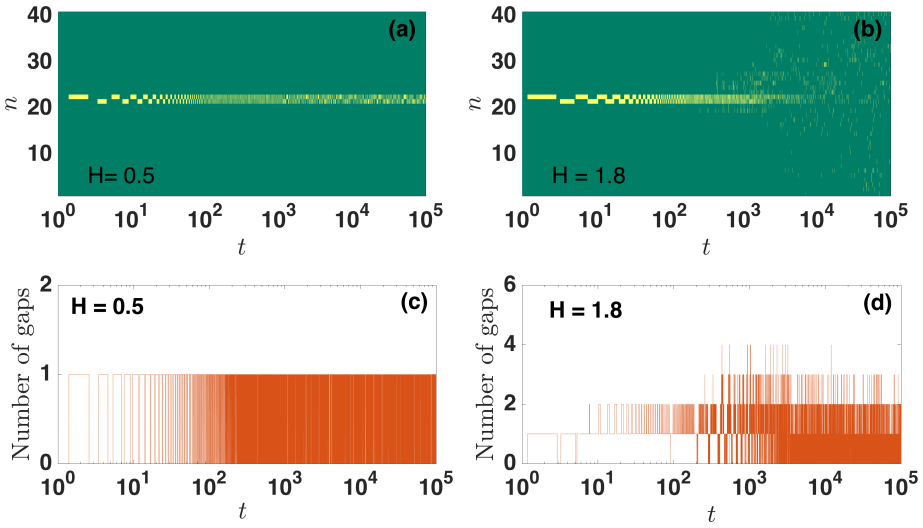

Fig. 3.9. The spatiotemporal evolution of the gaps in the Hertzian model for energies $H = 0.5$ (a) and $H = 1.8$ (b). The yellow (lighter) color corresponds to the lattice points where $(u_n(t) - u_{n-1}(t)) > \delta_n$. The instantaneous total number of gaps for the Hertzian model for energies $H = 0.5$ (c) and $H = 1.8$ (d).

region $0.5 \lesssim H \lesssim 1.8$ the wave-packet starts to delocalize (as quantified by P) at the same time that additional gaps start to move away from site $n = 21$. For $H = 1.8$, as shown in Fig. 3.9(b), this happens around $t \approx 3 \times 10^2$ which is the same time that P [see Fig. 3.6(b)] starts to increase and the wave-packet starts to delocalize. These results, indicate a direct connection between the *spreading of gaps* within the lattice and the energy threshold beyond which the Hertzian model always traverses to delocalized and extended chaos.

To complete the comparison between the two models we also calculate the so called "spectral entropy" [88] by monitoring the corresponding normal modes. We write the weighted harmonic energy of the kth mode as $v_k = E_k / \sum_{k=1}^{N} E_k$ where E_k is the kth mode's energy. We thus obtain the spectral entropy at time t as:

$$S(t) = -\sum_{k=1}^{N} v_k(t) \ln v_k(t). \tag{3.10}$$

with $0 < S \leq S_{max} = \ln N$. It is however more convenient to use the normalized spectral entropy $\eta(t)$ which can be written as,

$$\eta(t) = \frac{S(t) - S_{max}}{S(0) - S_{max}}. \tag{3.11}$$

The value of η is normalized such that $0 \leq \eta \leq 1$. With this normalization, when η remains close to one the dynamics does not substantially deviate from the initially excited modes. On the other hand as more modes are excited, η decreases towards zero.

For a system at equipartition, a theoretical prediction for the mean entropy $\langle\eta\rangle$ exists, which assumes that the modes at equipartition follow a Gibbs distribution when the nonlinearity is weak. The analytical form of the mean entropy $\langle\eta\rangle$ is given by [89, 90]

$$\langle\eta\rangle = \frac{1 - C}{\ln N - S(0)} \tag{3.12}$$

with $C \approx 0.5772$ being the Euler constant.

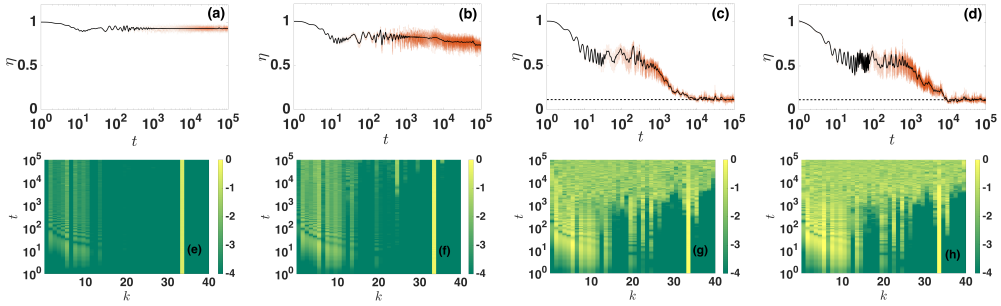

Fig. 3.10. Top row: The time evolution of the normalized spectral entropy $\eta(t)$ for the Hertzian model. The dashed horizontal line in panels (c) and (d) show the mean value $\langle\eta\rangle$ given by Eq. (3.12). Bottom row: The evolution of the weighted harmonic energy of eigenmodes as a function of time. The modes are sorted by increasing frequency [c.f. Fig. 3.3(b)]. The values of the energy are $H = 0.25$ (a)-(e), $H = 0.5$ (b)-(f), $H = 1.8$ (c)-(g), and $H = 3$ (d)-(h). The color bars on the right sides of panels (e)-(h) are in logarithmic scale.

In Fig. 3.10 we plot the time evolution of η and of the normal modes for different values of the energy H. As shown in Fig. 3.10(a), for $H = 0.25$ where the dynamics for both models is localized, the normalized entropy initially has a value of $\eta = 1$ and only slightly decreases from that value. This indicates that the dynamics is dominated by the single mode initially excited along with some weakly excited low frequency modes. This is also very clear in Fig. 3.10(e) where the time evolution of the weighted modes is shown. Initially only mode 34 is visible, and after some brief transient phase, a set of extended (low frequency modes) are slightly excited. In fact after $t \approx 10^2$ the amplitude of each mode remains approximately constant and so does the time evolution of the normalized entropy $\eta(t)$.

Similar behavior for the Hertzian model is observed at $H = 0.5$ [Figs. 3.10(b)-(f)], although in this case $\eta(t)$ reduces its value at different time instants. By closely inspecting panel (f) we see that indeed around $t \approx 8 \times 10^3$ and $t \approx 8 \times 10^4$ new modes appear to kick in. For the two examples with $H \geq 1.8$ shown in panels (c),(g) and (d),(h) of Fig. 3.10 the system is driven closer to equipartition. The entropy $\eta(t)$ features a plateau at a value around $\eta \approx 0.5$ and then decreases into a minimum value. The horizontal dashed lines in Figs. 3.10(c) and (d) indicate the value of the mean entropy at equipartition as given by Eq. (3.12). The asymptotic value of $\eta(t)$ approaches the theoretically predicted value of $\langle\eta\rangle$ with $H \geq 1.8$ as indicated in panels (c) and (d).

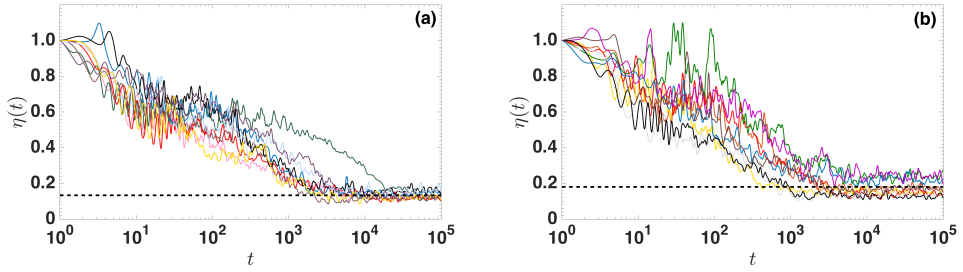

Fig. 3.11. (a) Temporal evolution of $\eta(t)$ for the 9 most localized modes of the distribution corresponding to Fig. 3.3(b). (b) Temporal evolution of $\eta(t)$ obtained by exciting site $n = 20$ of 9 different disordered realizations with $\alpha = 5$. In both panels, the results correspond to the Hertzian model with an energy $H = 3$. The dashed horizontal lines show the average (on the different initial conditions), mean entropy at equipartition $\langle\eta\rangle$.

The fact that the final stages of these simulations are close to an equipartition state is also supported by the mode energy distribution which clearly shows that at the last decade all modes appear to participate in the dynamics.

The existence of an energy *threshold* beyond which equipartition is reached for the Hertzian model depends neither on the particular mode nor the chosen realization shown in Fig. 3.3(b). To illustrate this, we first identified the 9 most localized modes of the distribution shown in Fig. 3.3(b). We then excite these modes by using a single site excitation around the point of localization of each mode with an energy $H = 3$. The choice of energy is to ensure that it is above the *threshold* for each mode. The results are shown in Fig. 3.11(a) and it is clear in all cases that the system finally reaches equipartition. We also performed simulations using different disorder realizations with $\alpha = 5$, and exciting them at the central site $n = 20$ with energy $H = 3$. Since we always excite the same site but for different realizations, we may or may not excite a single localized mode. In any case, as it is shown in Fig. 3.11(b), the system reaches to equipartition in all cases. The absence of an energy threshold leading to equipartition

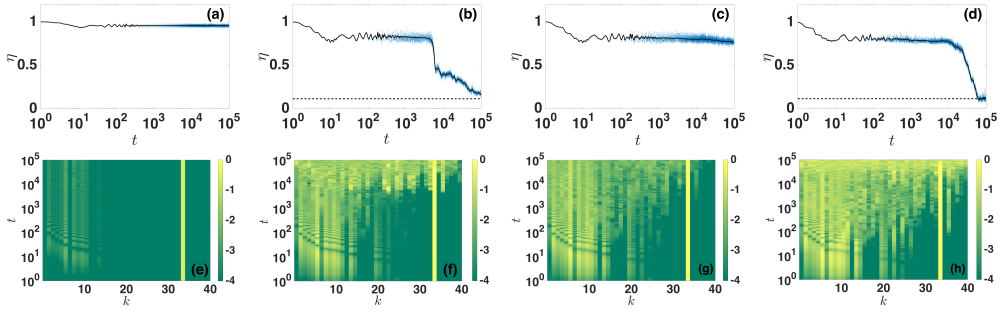

Fig. 3.12. Same as in Fig. 3.10 but for the FPUT model. The dashed horizontal line in panels (b) and (d) show the mean value $\langle\eta\rangle$ given by Eq. (3.12). The values of the energy in this case are $H = 0.25$ (a)-(e), $H = 2.9$ (b)-(f), $H = 4$ (c)-(g), and $H = 8.7381$ (d)-(h).

for the FPUT model is also shown in Fig. 3.12. F $H = 0.25$ [panels (a) and (e)] the behavior is the same as for the Hertzian model: $\eta(t)$ saturates to a finite value close to 1 and a dominant mode along with some low frequency modes are present. For a much higher energy excitation of $H = 2.9$ shown in Figs. 3.12(b) and (f), from the early stages of the evolution more modes are excited and the entropy exhibits a plateau at $\eta \approx 0.7$. Note that such a plateau is well known and studied in homogeneous FPUT chains and is associated with a metastable phase [90]. Beyond this point the entropy abruptly falls at $t \approx 5 \times 10^3$ and finally reaches a minimum value which is found to be close to the analytical result for equipartition given by Eq. (3.12). As shown in Fig. 3.12 (f) this is associated with the excitation of almost all linear modes.

For a larger initial energy $H = 4$, i.e. the case presented in the second row of Fig. 3.8, the dynamics of η is quite surprising. As shown in Fig. 3.12(c) the entropy saturates for most of the evolution around a relatively large value $\eta \approx 0.82$. For the last two decades it starts to decrease, but with a very small slope. This is unexpected (also in accordance to the homogeneous FPUT studies e.g. Ref. [90]) since for higher energy excitations we anticipate to have a shorter plateau (than the one for $H = 0.25$) and the system to be driven faster towards equipartition. However, here the dynamics suggests that the contribution of modes other than mode 34 remains weak. This is also seen in Fig. 3.12(g) where not all modes have been excited at the end of the simulation, and in particular the highest frequency ones are still "mute". However, it is expected, that for larger timescales the system will reach equipartition, and η will eventually drop.

To highlight the alternate behavior found for the disorder FPUT model, in Fig. 3.12(d) we show the entropy for an even higher energy excitation of $H = 8.7381$ which corresponds to the results presented in the third row of Fig. 3.8. Similarly to the case of $H = 2.9$ the entropy saturates for a long time interval at a value $\eta \approx 0.8$. Then at $t \approx 10^4$, η starts to drop and at the end of the simulation reaches a minimal value well captured by the analytical prediction of Eq. (3.12). Accordingly in Fig. 3.12 (h) we observe that as time increases more modes participate in the dynamics, and at the final stages of the simulation all modes are present.

3.4 Conclusions

In this chapter, we numerically studied energy localization/delocalization and the chaoticity of two one-dimensional disorder models: the Hertzian model featuring a non-smooth nonlinearity, and the FPUT model. The two models share the same linear limit and thus the same linear eigenmodes. Statistics on 1000 disorder realizations demonstrate that beyond a sufficient disorder strength, the linear chain acquires a significant amount of strongly localized modes. Focusing on a single realization from the aforementioned ensemble, we show that the evolution of such a mode can be characterized by three different scenarios: (i) localization with no chaos; (ii) localization and chaos; (iii) spreading of energy, chaos and equipartition.

In particular, for sufficiently small energies the two models behave quantitatively simi-

lar, with excitations remaining localized and non chaotic, at least for the time scales of our simulations. For larger energy values, a transient energy region is found for which the Hertzian model exhibits localized but chaotic behavior. After an energy threshold, associated to the spreading of gaps in the lattice, the Hertzian model evolves into an equipartition, chaotic state independent of the particular value of the initial energy.The appearance of such a threshold is confirmed for other modes of the particular disorder realization but also for different disorder realizations.

On the other hand the dynamics of the FPUT model is substantially different from that of the Hertzian model. Firstly, delocalization and chaos emerge for higher energies for the FPUT model. We find strong numerical evidences that this difference is attributed to the non-smooth nonlinearity which is present only in the Hertzian model. Furthermore, for higher energy values, the FPUT system shows an alternating behavior between chaotic *localized* and chaotic *extended* dynamics lacking a particular threshold beyond which equipartition is always reached. We therefore conclude that, in contrast to the Hertzian model, the final state of a strongly disordered FPUT lattice under single site excitation, strongly depends on both the disorder realization and the initial excitation energy.

Our results provide further insights into the chaotic dynamics of strongly disordered chains. Using additional chaos indicating tools such as the deviation vector densities, we are able to clearly separate localized (in space) from extended chaotic behavior. In addition we show that non-smooth nonlinearities do not only induce the destruction of Anderson localization but also provide a mechanism to drive the system into equipartition. An interesting direction stemming from our results is to pursue a thorough statistical analysis in order to probe the interplay between disorder and nonlinearity and the resultant effect on the corresponding time scales for energy equipartition.

Chapter 4

Disordered one-dimensional micropolar lattice supporting rotational waves

Contents

4.1 The micropolar lattice

Following the recent studies in granular chains and also other architected mechanical structures (see e.g., Ref. [16, 17]), it has become clear that taking into account more degrees of freedom of the elastic particle in a chain not only is more realistic but also can reveal new physical phenomena. As such, in this chapter whose contents are based on a published article [91], we are interested into extending the studies of 1D chains of elastic particles by taking into account both the transverse and rotational degrees of freedom. We note that, few such studies already exist in the literature but are focused on the tight binding model by assuming a linear coupling between two (or more) 1D chains [92, 93] and illustrate how the coupling modifies the energy transport properties. In particular, here we will consider a model describing square blocks as shown in Fig. 4.1 which are able to perform not just out of plane displacements, but also rotations.

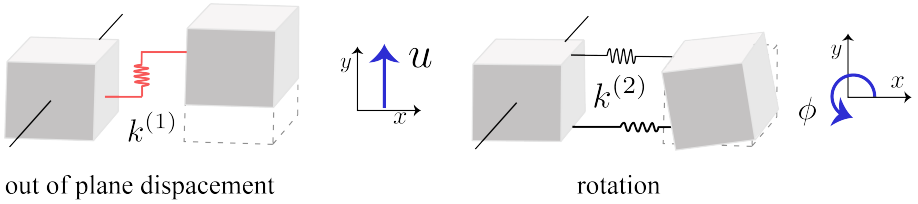

Fig. 4.1. A schematic showing the micropolar model to be used in this chapter. The system is composed of blocks which can perform both out of plane displacements (y-direction) and rotations. The two motions are described by two different stiffness.

Such a model is relevant to macroscopic mechanical lattices (e.g., granular phononic crystals, lego and origami chains [94, 42, 95, 17, 16]), where the coupling between the DOFs stems from either the geometrical characteristics or from the material properties. The main goal of this study is to unveil the role of the coupling between the DOFs regarding the energy transport in the presence of strong disorder and to identify the differences with the underlying 1D harmonic lattice. In particular, we first discuss the spectral properties of the model both without and with disorder and characterize the polarization of the linear modes as well as their localization properties. Furthermore, we present results regarding the dynamics of the system after different initial excitations. Finally, we show how the asymptotic long time evolution of the energy exhibits interesting features including different spreading behavior different from what is observed in purely single DOF models as well as strong polarization of the wave-packet tails.

4.2 The model and equations of motion

A phononic structure composed of discrete block-spring elements such that the nth element can be described by transverse and rotational DOFs as shown in Fig. 4.2. The transverse displacements are in the y direction whilst the rotation is about an axis perpendicular to the xy-plane. The blocks are coupled through a shear stiffness $k_n^{(1)}$ and a bending one $k_n^{(2)}$ [see Fig. 4.2(b,c)]. In this chapter, N identical cube blocks of

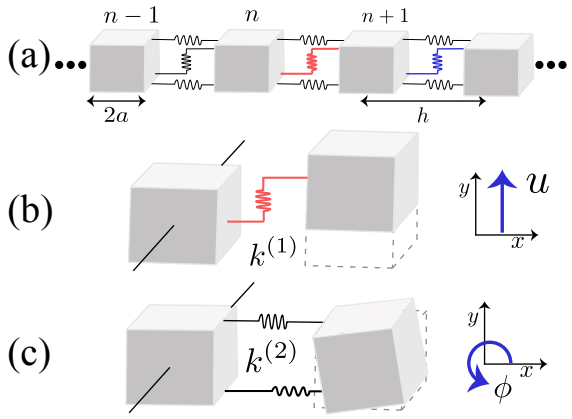

Fig. 4.2. (a) Schematic of the disorder phononic lattice with random shear stiffness indicated by the different spring thicknesses (colors). (b) Illustration of the transverse motion and the corresponding shear stiffness $k^{(1)}$. (c) Illustration of rotational motion and the corresponding bending stiffness $k^{(2)}$.

mass m with edges of length $2a$ and consequently a moment of inertia $I = 2ma^2/3$. Systems that could be potentially described by such a structure include models in micro- and nano-scale films [96], granular media [16], modeling of beam lattices [97] or the interaction of finite size particles with pre-designed connectors [17]. The periodicity of the system is imposed by the distance h between the center of each block as shown in Fig. 4.2, where u_n and ϕ_n respectively represent the transverse and rotational motion of the nth block from equilibrium. The corresponding momenta are written as $P_n^{(u)} = m\dot{u}_n$ and $P_n^{(\phi)} = I\dot{\phi}_n$ for the former and latter motions, while $(\dot{\ })$ denotes derivative with respect to time. The total energy of the system H, of the system is given by the following expression [98, 99]

$$H = \sum_{n=1}^{N} \frac{1}{2}P_n^{(u)^2} + \frac{1}{2I}P_n^{(\phi)^2} + \frac{1}{2}K_{n+1}^{(1)}\Big[(u_{n+1}-u_n) + \frac{3}{2}(\phi_{n+1}+\phi_n)\Big]^2 + \frac{1}{2}K_{n+1}^{(2)}(\phi_{n+1}-\phi_n)^2. \tag{4.1}$$

In this thesis the constants are defined such that, $K_n^{(1)} = 2k_n^{(1)}(2a)^2/l_d^4$, $K_n^{(2)} = k_n^{(2)}2a^2/l^2$, the lengths $l = h - 2a$ and $l_d = \sqrt{l^2 + (2a)^2}$ and for simplicity, $m = 1$, $l = 1$ and thus $h = 3$. The equations of motion for the two DOFs are explicitly given by:

$$\begin{aligned}
\ddot{u}_n &= K_{n+1}^{(1)}\Big(u_{n+1} - u_n\Big) - K_n^{(1)}\Big(u_n - u_{n-1}\Big) \\
&\quad + \frac{3K_{n+1}^{(1)}}{2}\Big(\phi_{n+1} + \phi_n\Big) - \frac{3K_n^{(1)}}{2}\Big(\phi_n + \phi_{n-1}\Big), \qquad (4.2)\\
I\ddot{\phi}_n &= \frac{3K_n^{(1)}}{2}\Big(u_{n-1} - u_n\Big) + \frac{3K_{n+1}^{(1)}}{2}\Big(u_n - u_{n+1}\Big) \\
&\quad - \frac{9K_{n+1}^{(1)}}{4}\Big(\phi_{n+1} + \phi_n\Big) - \frac{9K_n^{(1)}}{4}\Big(\phi_n + \phi_{n-1}\Big) \\
&\quad + K_{n+1}^{(2)}\Big(\phi_{n+1} - \phi_n\Big) - K_n^{(2)}\Big(\phi_n - \phi_{n-1}\Big). \qquad (4.3)
\end{aligned}$$

It is important to first study the periodic phononic crystal [94] with $K_n^{(1)} \equiv K^{(1)} = 1$ and $K_n^{(2)} \equiv K^{(2)}$. In this case, Bloch like solutions are sought and take the form

$$\mathbf{X}_n = \begin{pmatrix} u_n(t) \\ \phi_n(t) \end{pmatrix} = \mathbf{X} e^{i\Omega t - iQn}, \tag{4.4}$$

where $\mathbf{X} = [U, \Phi]$ is the amplitude vector, Ω is the frequency and Q is the Bloch wave number. Inserting Eq. (4.4) into Eqs. (4.2) and (4.3) we obtain the following eigenvalue problem for the allowed frequencies

$$\mathbf{S}\mathbf{X} = \Omega^2 \mathbf{X}, \tag{4.5}$$

where the resultant dynamical matrix,

$$\mathbf{S} = \begin{pmatrix} 4\sin^2 q & -6\ i \sin q \cos q \\ 6\ i \sin q \cos q & \frac{2}{3}[9\cos^2 q + 4K^{(2)} \sin^2 q] \end{pmatrix},$$

with $q = Q/2$.
The corresponding expression for the eigenfrequencies is given by

$$\Omega_{\pm}^2 = \frac{1}{2}\Bigg\{ 4\sin^2 q + \frac{2}{3}\left(\frac{9}{4} 4\cos^2 q + 4K^{(2)} \sin^2 q\right) \pm \sqrt{\left[4\sin^2 q + \frac{2}{3}\left(\frac{9}{4} 4\cos^2 q + 4K^{(2)} \sin^2 q\right)\right]^2 - 64K^{(2)} p \sin^4 q} \Bigg\}. \tag{4.6}$$

The dispersion relation of Eq. (4.6) for $K^{(2)} = 1$ is depicted by the solid curves plotted in Fig. 4.3(a). We directly observe the appearance of two branches separated by a band gap and terminated by a maximum allowed frequency. Since the two DOFs are coupled, the modes are composed by a mixture of transverse and rotational motion. Note that the constant $K^{(2)}$, which depends on the bending stiffness, can be used as a tuning parameter to change the form of the dispersion relation and the dominant motion participating in each propagating mode [94].

In the rest of this chapter we introduce disorder to the system only through the shear spring stiffness's $K_n^{(1)}$ [see also Fig. 4.2(a)]. We choose this particular disorder aiming to expose the role of each DOF and isolate its importance in the energy transfer. The values of $K_n^{(1)}$ are taken from a uniform probability distribution

The parameter W determines the width of the distribution and thus the strength of the disorder. Fig. 4.3(b) illustrates the eigenfrequencies of a strongly disordered ($W = 2$) finite chain of $N = 10^3$ blocks. The eigenmodes have been sorted from lowest to highest frequency for increasing mode index k. Due to the strength of the disorder, the middle band gap is filled with modes while the maximum frequency of the system is much bigger in comparison to the maximum frequency of the periodic chain.

To further characterize the disordered finite lattice, for each mode we calculate P for the modes. The mean value of P taken for 200 disorder realizations is shown in the

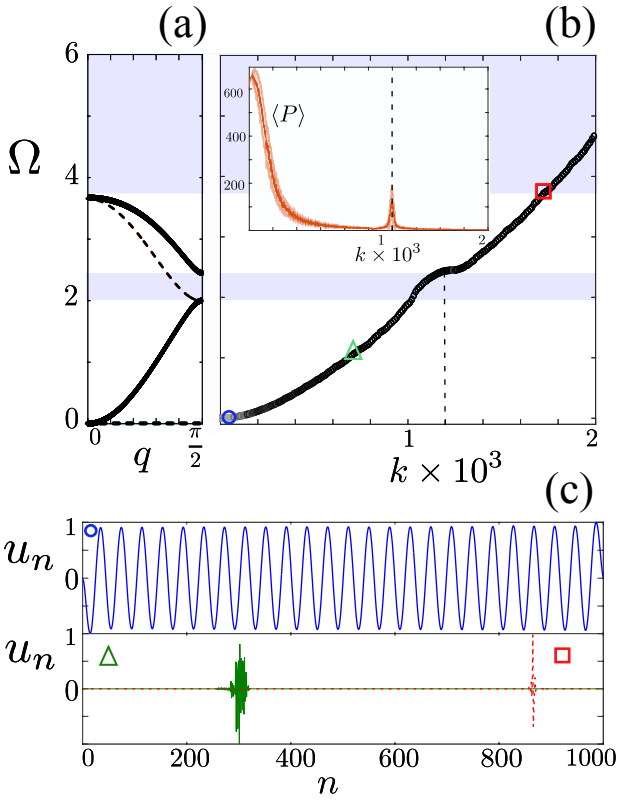

Fig. 4.3. (a) Dispersion relations of the lattice for $K^{(1)} = 1$ and $K^{(2)} = 1$ ($K^{(2)} = 0$) solid curves (dashed curves). (b) Corresponding eigenfrequencies for a single strongly disordered lattice ($W = 2$) with $\langle K^{(1)} \rangle = 1$ and $K^{(2)} = 1$. The inset shows the mean value (200 realizations) of $\langle P \rangle$ for each mode, and the standard deviation (shaded area). The vertical dashed line denotes the index where the *quasi-extended* modes appear. (c) Representative profiles of the eigenmodes of the disordered lattice with $K^{(2)} = 1$ for the three different cases indicated by the circle, square and triangle in (b). Here we show only profiles for u_n.

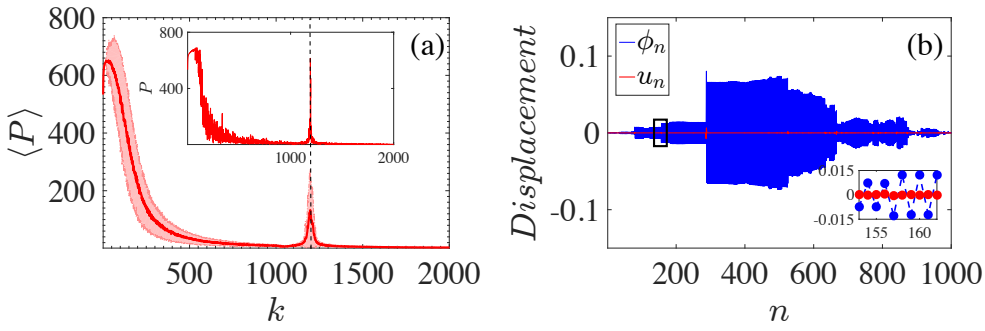

Fig. 4.4. (a) A full view of the inset depicted in Fig. 4.3(b) and its own inset shows P against sorted linear eigenmodes for a single disorder realization. The vertical dashed line denotes the index where the *quasi-extended* modes appear. (b) The profile of a characteristic *quasi-extended* mode $k = 1194$ showing negligible displacements u_n in comparison to ϕ_n. The inset shows a zoom of the region enclosed by a black rectangle with consecutive rotations having similar amplitudes and opposite signs ($\phi_{n+1} \approx -\phi_n$).

inset of Fig. 4.3(b). It becomes clear that most of the modes are strongly localized throughout the spectrum except at very low frequencies where a rather small portion of the modes is extended. As such, we may loosely describe the modes as either localized or extended. Interestingly enough we obtain a set of what we coin as *quasi-extended* modes around the cut-off frequency of the upper branch of the periodic case. The appearance of these modes is due to the particular implemented disorder, which is only on the shear stiffness.

4.3 Quasi-extended modes

Here we focus our attention on the *quasi-extended* modes appearing close to the cut-off frequency of the upper band of the periodic case (see Fig. 4.3). As depicted in Fig. 4.4(a), the participation number $\langle P \rangle$ features a peak around $k \approx 1200$ which corresponds to the cut-off frequency of the upper branch of the periodic system [see Figs. 4.3(a) and (b)]. Note that in many cases we found that these modes may be as extended and have P values which are of the same order as the low index modes (small k) as indicated by the inset in Fig. 4.4(a) corresponding to a single realization.

To further understand this phenomenon we now consider a characteristic profile of such a mode depicted in Fig. 4.4(b). We find that: (i) these modes consist almost solely of rotational motion (the contribution of the transverse DOFs is negligible i.e., $u_n \approx 0$) and (ii) the profile of the modes consists of various regions with consecutive rotations of similar amplitude and opposite signs ($\phi_{n+1} \approx -\phi_n$), as shown by the zoom in the inset of Fig. 4.4(b). Using this two observations and the functional form of the Hamiltonian (4.1), it is noticeable that for these modes, effectively only the bending potential term analogous to $K^{(2)}$ is present. But since there is no disorder in $K^{(2)}$ these modes are extended reminiscent of the periodic lattice.

For illustration in Fig. 4.3(c) we show the normalized transverse profiles of an extended mode [$k = 50$ (circle)] and of two localized modes [$k = 735$ (triangle), and $k = 1700$ (square)]. The normalized rotational profile follows the same patterns. As we will show below, both the low frequency *extended* modes and the *quasi-extended* modes contribute to the transfer of energy in the lattice.

4.4 Dynamics of the system

To study the properties of energy transfer in the system we excite strongly disordered lattices using single site initial conditions. Our results are averaged over an ensemble of 200 disorder realizations and since we are interested in the effects of strong disorder we choose $W = 2$ such that $K_n^{(1)} \in (0, 2)$. For all the time dependent simulations, each realization had $N = 10^5$ lattice sites.

4.4.1 Momentum excitation

We first study the dynamics of the lattice under two different initial momentum excitations

$$P_{N/2}^{(\phi)}(0) = \sqrt{I}, \text{ or } P_{N/2}^{(u)}(0) = 1 \tag{4.7}$$

i.e., initially exciting either the transverse or the rotational momentum of the central site. Note that this choice of initial conditions corresponds to a total energy of $H = 0.5$ for both cases. Some typical time evolutions of the energy densities are shown Figs. 4.5(a) and (b) for an initial (a) rotational and (b) transverse momentum excitation. We observe that for both cases, a large amount of energy remains localized in the region of the initial excitation at the lattice's center. This is expected due to the fact that most of the modes are localized and thus the implemented initial condition strongly excites localized modes around the central site. This is also quantified by the time evolution of the averaged participation number $\langle P \rangle$ shown in Figs. 4.5(c) and (d) for respectively the rotational and transverse initial momentum excitations. In fact we observe that in both cases $\langle P \rangle$ saturates to a small number compared to the total lattice size. However, comparing the two final values we observe a significant difference between the two cases as the transverse initial excitation [Fig. 4.5(d)] leads to a larger $\langle P \rangle$.

This behavior can be understood by studying the projection of the initial conditions onto the normal modes of a finite but large disordered lattice. For a given initial momentum excitation we define the vector $\vec{V}(0) = [\dot{u}_1(0), \ldots, \dot{u}_N(0), \dot{\phi}_1(0), \ldots, \dot{\phi}_N(0)]^T$ whose projection on the system's normal modes is given by $\vec{R} = \mathbf{A}^{-1}\vec{V}(0)$ with matrix $\mathbf{A}$ having as columns the lattice eigenvectors. Using this projection, we can calculate the energy given to each normal mode as $E_k = \dot{R}_k^2/2$ where $\dot{R}_k$ are the elements of projection vector $\vec{R}$. Obviously the system's total energy is $H = \sum E_k$. Figs. 4.5(e) and (f), although they appear to have a similar form, exhibit important differences regarding low index (k) modes. Since we sorted the modes with increasing frequency, low indices correspond to low frequency extended modes. In fact, for the initial *rotational* momentum [Fig. 4.5(e)], the low frequency extended modes (low index k) are

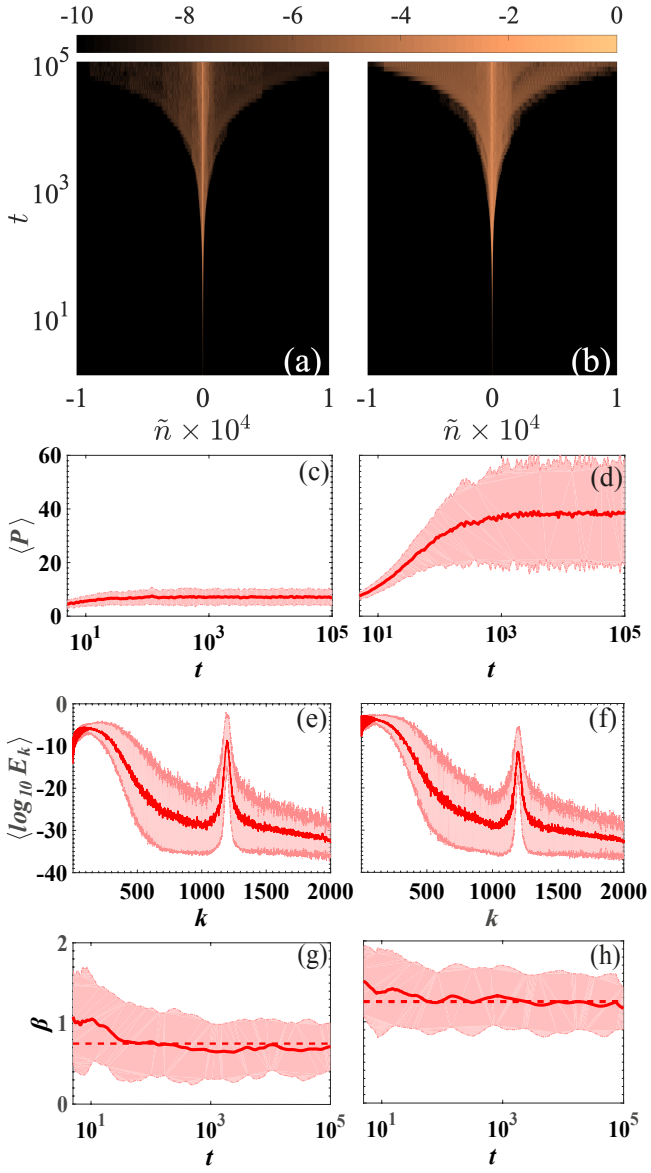

Fig. 4.5. Results corresponding to rotational (left panels) and transverse (right panels) initial momentum excitation. (a)-(b) Time evolution of the energy distribution for a representative disordered realization with colorbar in $\log_{10}$ scale . The horizontal axis represents $\tilde{n} = n - N/2$. (c)-(d) Time evolution of the average participation number $\langle P \rangle$. (e)-(f) Average energy per mode after projecting the initial condition to the normal modes. (g)-(h) Estimation of the exponent β related to the time evolution of the average second moment through $\langle m_2(t) \rangle \propto t^\beta$. The horizontal dashed line indicates the values (g) $\beta = 0.75$ and (h) $\beta = 1.25$. For (c)-(h), results have been averaged over 200 disorder realizations, and the shaded area denotes one standard deviation.

the stronger excited ones with an energy up to the order of 10^{-6}. On the other hand, by initially exciting the transverse momentum, the low frequency modes (low index k) as shown in Fig. 4.5(f), are strongly excited acquiring energies up to 10^{-3}. These orders of magnitudes difference in energy of low frequency extended modes explains the differences in $\langle P \rangle$ shown in Figs. 4.5(c) and (d).

Here we also observe major differences between the micropolar lattice and the well studied 1D harmonic lattice with disorder [78, 54, 55]. With an initial momentum excitation, instead of exciting all modes with the same energy as in the 1D harmonic lattice, here we observe a strong excitation of the low frequency modes and another set of modes around the cut-off frequency of the upper branch of the periodic case. As we will see below this has consequences to the energy transport.

In Figs. 4.5(g) and (h) we observe that for both cases β reaches an asymptotic value. In fact $\beta \approx 0.75$ ($\beta \approx 1.25$) for initial rotational (transverse) momentum excitations corresponding to subdiffusive (superdiffusive) transport. These values are quite different than the ones observed for the 1D harmonic lattice where momentum excitation is always found to be superdiffusive with $\beta \approx 1.5$ [54, 55, 100]. To qualitatively explain this difference we first note that the exponent β has been shown to depend mainly on two factors: (i) the characteristics of extended modes (group velocity, localization length as function of frequency, total number) and (ii) the projection of the initial condition on the modes [54, 55, 100]. Regarding point (i), for both models, there is a set of extended modes at $\Omega \ll 1$. Major differences are thus expected since the dispersion relation of Eq. (4.6) for the micropolar lattice at low frequencies is quadratic with respect to the wavenumber i.e., $\Omega \approx 3\sqrt{K^{(2)}}Q^2$ in contrast to the 1D harmonic lattice where $\Omega \approx Q$. Furthermore, for the micropolar lattice, the *quasi-extended* modes at higher frequencies may influence the energy spreading, as it was shown for example in [54, 101] where additional extended modes were found either due to symmetries or resonances. As far as point (ii) is concerned, the results of Figs. 4.5(e) and (f) are substantially different from those of the 1D harmonic lattice indicating that differences between the two models are anticipated.

4.4.2 Displacement excitation

To further compare the behavior of the micropolar model to that of the 1D harmonic lattice [72, 73, 54], we now study the dynamics induced by the following initial conditions

$$\phi_{\frac{N}{2}}(0) = \phi_{\frac{N}{2}}, \text{ or } u_{\frac{N}{2}}(0) = u_{\frac{N}{2}}, \tag{4.8}$$

which correspond to initial rotation or transverse displacement of the central block. In this study, the values of $\phi_{\frac{N}{2}}$ and $u_{\frac{N}{2}}$ are chosen such that the total energy for each realization is again $H = 0.5$.
Similarly to Section 4.4.1, the evolution of the energy distribution [Figs. 4.6(a) and (b)] is characterized by a localized wave-packet at the region of the initial excitation in center of the lattice, and by a portion which is propagating. However, compared to the initial momenta excitations, here the energy carried away from the central site is

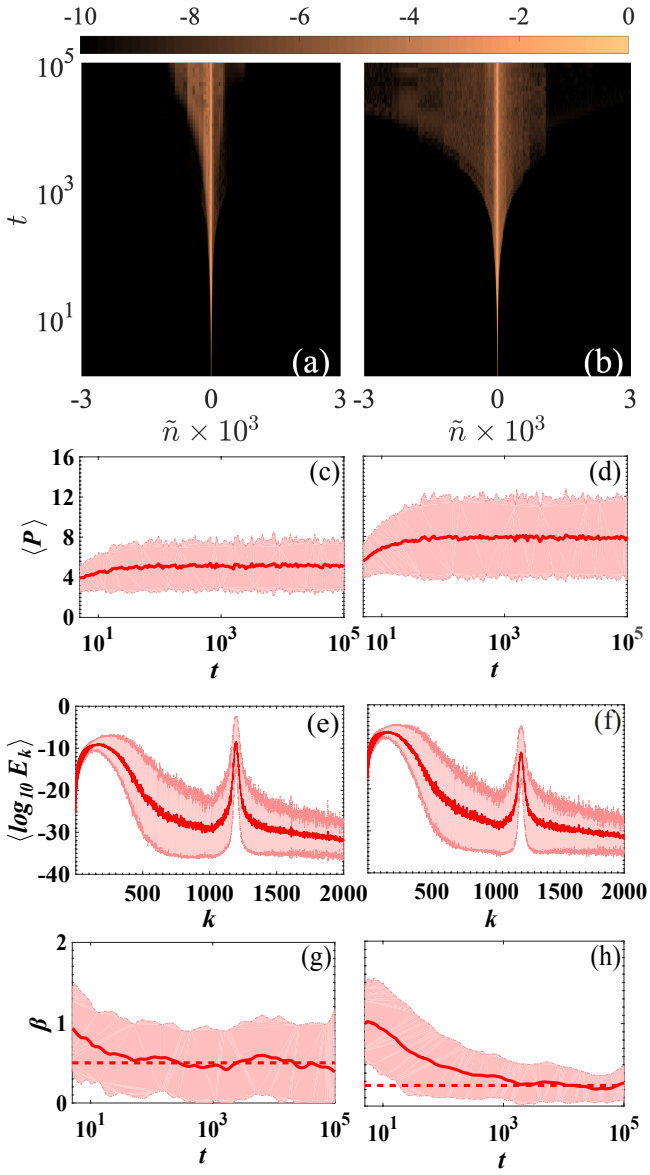

Fig. 4.6. Similar to Fig. 4.5 but for displacement excitation(s). The horizontal dashed lines in (g) and (h) respectively indicate $\beta = 0.5$ and $\beta = 0.25$.

substantially smaller. For both types of initial conditions, $\langle P \rangle$ attains an asymptotic value of less than 10 sites as shown in Figs. 4.6(c) and (d). This behavior can be also understood using the projection of the initial conditions to the normal modes of a large but finite lattice. This is now done by projecting the vector $\vec{U}(0) = [u_1(0), \ldots, u_N(0), \phi_1(0), \ldots, \phi_N(0)]^T$ onto the normal modes to yield $\vec{R} = \mathbf{A}^{-1}\vec{U}(0)$. In this case, the energy of the kth normal mode is $E_k = \Omega_k^2 R_k^2/2$ with Ω_k being the kth eigenfrequency. Again the system's total energy is $H = \sum E_k$. The outcome of this projection is shown in Figs. 4.6(e) and (f) for the initial rotation and transverse displacement respectively. The results are similar to those of Figs. 4.5(e) and (f) with suppressed contributions of the low frequency modes leading to a small value of $\langle P \rangle$ during the evolution.

Furthermore, we also calculated the exponent β for the energy propagation resulting from these two different initial excitations and the results are shown in Figs. 4.6(g) and (h). In a similar manner as in the 1D disordered harmonic lattice case, single site displacement excitation lead to subdiffusive behavior. However, our findings show that although the initial rotation excitations leads to the same value ($\beta \approx 0.5$) as in the 1D harmonic lattice, the initial transverse displacement features extremely slow energy transport with $\beta \approx 0.25$. The discrepancy between the two models is anticipated as it was discussed at the end of Section 4.4.1. However our results for the displacement excitations of the micropolar lattice strongly suggest that the energy transport is indeed mediated by both the low frequency and the *quasi-extended* modes. To be more precise we compare the results of Fig. 4.5(e) with Fig. 4.6(e) and notice that in the latter lower frequency modes are less excited leading to a smaller value of β ($\beta \approx 0.75$ for the former and $\beta \approx 0.5$ for the latter). In the same spirit, by comparing Fig. 4.5(e) with Fig. 4.6(f) the main difference lies in the *quasi-extended* modes which are suppressed in the later case leading to a $\beta \approx 0.25$ instead of 0.75. Thus reducing the amount of energy allocated to either the low frequency extended modes or the *quasi-extended* modes results in a reduced β suggesting that both contribute to the energy spreading.

Note that the result of initial transverse momentum, corresponding to Fig. 4.5(f) is not compared with the other three since in that case the low frequency modes are highly excited. We thus conclude that the complete picture is comprehended by casting one eye on the low frequency extended and the other onto the *quasi-extended* ones.

4.4.3 Energy contributions in the micropolar lattice

The participation number measures the localization of the total energy and the exponent β is a measure of how fast the energy is spreading, however, none of them carries any information of what amount of this energy is attributed to the rotational or the transverse DOFs. We can have an indication of how much energy is attributed to each of the two DOFs by decomposing the total energy of the system into two parts i.e., $H = H_R + H_T$ as follows

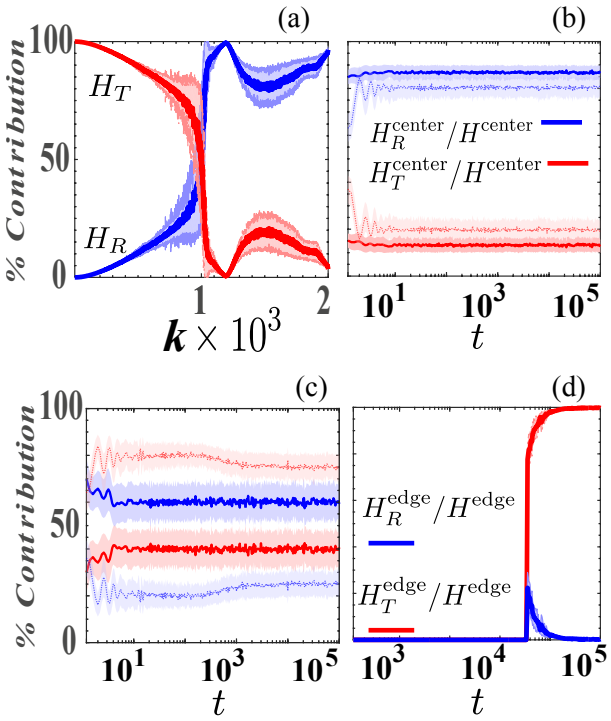

Fig. 4.7. (a) Averaged normalized energy contributions H_R and H_T of the normal modes for finite lattices of 1000 sites. (b) Time evolution of normalized averaged rotational (H_R^{center}) and transverse (H_T^{center}) energy contributions near the excitation region. Solid bolder (dashed lighter shaded) curves show rotational displacement (momentum) initial excitations. (c) Same as (b) but for transverse displacement (momentum) initial excitations. (d) Time evolution of averaged normalized energy contributions H_R^{edge} and H_T^{edge}, for transverse momentum excitations. Averaged values are over 200 disorder realizations and one standard deviation is indicated by the lightly shaded regions.

$$H_R = \sum_{n=1}^{N} \frac{1}{2I} P_n^{(\phi)^2} + \frac{9}{8} K_{n+1}^{(1)} (\phi_{n+1}+\phi_n)^2 + \frac{1}{2} K_{n+1}^{(2)} (\phi_{n+1}-\phi_n)^2 + \frac{3}{4} K_{n+1}^{(1)} (\phi_{n+1}+\phi_n)(u_{n+1}-u_n), \tag{4.9}$$

$$H_T = \sum_{n=1}^{N} \frac{1}{2} P_n^{(u)^2} + \frac{1}{2} K_{n+1}^{(1)} (u_{n+1}-u_n)^2 + \frac{3}{4} K_{n+1}^{(1)} (\phi_{n+1}+\phi_n)(u_{n+1}-u_n), \tag{4.10}$$

separating the rotational H_R and transverse H_T energy contributions. Note that the coupling potential energy, which is described by the last terms in both Eqs. (4.9) and (4.10), is equally shared between the two contributions. It is interesting to determine the nature of the lattice's energy in two different regions: i) around the initially excited central block and ii) sufficiently far away from the region of localization. For the central area we calculate the energy using Eqs. (4.9) and (4.10) but taking the sum for $n \in [N/2-100, N/2+100]$ to obtain H_R^{center} and H_T^{center}. Conversely, we also define the

energies at the edges of the energy distribution H_R^{edge} and H_T^{edge} by summing Eqs. (4.9) and (4.10) for $n \notin [N/2 - 5000, N/2 + 5000]$.

Before discussing the dynamical behavior of the system in these two distinct regions, it is relevant to show how the two different energy contributions are shared between the modes of a finite disordered lattice. The result is shown in Fig. 4.7(a) where the red (blue) curve depicts the transverse (rotational) energy contribution. As a general observation, we mention that the modes with lower k values are dominated by transverse motion, while the high frequency ones are dominated by rotational motion. As it is shown in Fig. 4.7(b), for both initial conditions concerning the rotational DOFs $[P_n^{(\phi)}(0) = \sqrt{I}\delta_{n,N/2}$ and $\phi_n(0) = \phi_{N/2}\delta_{n,N/2}]$, the central, localized part of the energy distribution is dominated by the rotational motion with almost the same ratios. This is so as the majority of the localized modes are dominated by rotation [see Fig. 4.7(a) and Fig. 4.3(b)]. By initially exciting the transverse DOF we end up with the two energy contributions in the central part shown in Fig. 4.7(c). We find that the central part of the energy distribution for the initial displacement excitation $[u_n(0) = u_{N/2}\delta_{n,N/2}]$ is still dominated by rotation as indicated by the solid curve in Fig. 4.7(c). Interestingly, for the case of initial transverse momentum excitation $[P_n^{(u)}(0) = \delta_{n,N/2}]$, the energy contribution of each motion in the central part is inverted with respect to all other cases. This is due to the fact that this initial condition excites more strongly the low frequency modes [Fig. 4.5(f)] which according to Fig. 4.7(a) are dominated by transverse motion.

Let us now turn our attention to the energy distribution far away from the central site following the propagating tails that are responsible for the energy transfer. The corresponding results for the initial transverse momentum excitation is shown in Fig. 4.7(d). After the arrival of the propagating front at the chosen sites $n = N/2 \pm 5000$, it is readily seen that the energy at the edges is completely carried by the transverse motion. We have confirmed the same quantitative result for all types of initial conditions. This behavior can be comprehended since we have shown that energy is carried away mostly from the low frequency extended modes hence as shown in Fig. 4.7(a) these modes (corresponding to small k) are almost completely constituted by transverse motion and so is the energy at the edges.

4.4.4 The special case of $K^{(2)} = 0$

Now, we focus on a special case of the system i.e., in the limit of vanishing bending stiffness $K^{(2)}$. Note that such a case is very relevant to situations where the bending stiffness is so small that it may be neglected, see for example Ref. [16].Then, the corresponding dispersion relation of the periodic system [dashed lines in Fig. 4.3(a)] is substantially altered. In particular instead of two propagating bands, it consists of a zero frequency non-propagative band and a dispersive band emerging after a cut-off frequency $\Omega = 2$. The zero frequency branch is made possible due to a counterbalance between the shear and bending forces [94].

To study the energy transfer for this special case of $K^{(2)} = 0$, we have performed simulations for the different single site initial conditions considered before and a characteristic

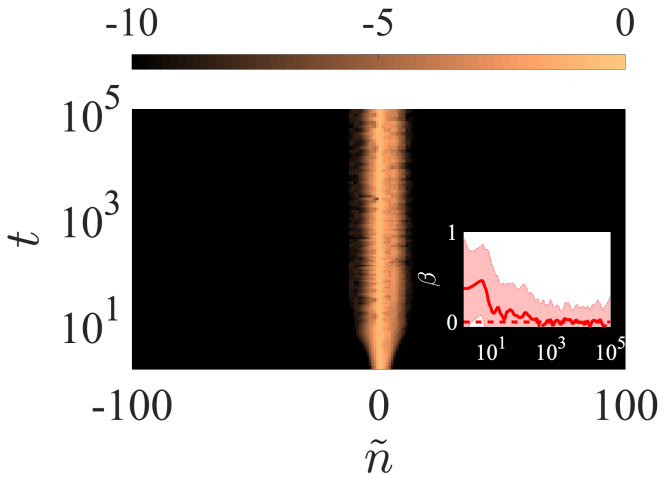

Fig. 4.8. Time evolution of the energy density after an initial transverse momentum excitation $P^u_{N/2}(0) = 1$ with $K^{(2)} = 0$ where $\tilde{n} = n - N/2$. The inset depicts the evolution of the exponent, β in the relation $\langle m_2(t) \rangle \propto t^\beta$ averaging over 200 disorder realizations, which is shown to be zero indicating no spreading. The horizontal dashed line indicates $\beta = 0$.

example is shown in Fig. 4.8. There it is readily seen that the energy remains localized around the center, and in addition there is no energy transfer to the rest of the lattice. This is also confirmed by the time dependence of the exponent β in $\langle m_2(t) \rangle \propto t^\beta$, which becomes zero (see inset of Fig. 4.8) thus signaling no energy spreading.

Trying to explain the absence of energy transport we found (by solving the corresponding eigenvalue problem numerically) that the lower branch of the system's frequency spectrum, in the limit case of $K^{(2)} = 0$, still remains at zero frequency even in the presence of strong disorder due to a counterbalance of the transverse and rotational motions. As such, in this limit, the micropolar lattice is similar to a 1D KG model i.e., featuring a single propagating band emerging after a lower cut-off frequency and thus the system is expected to exhibit AL.

4.5 Conclusions

We have demonstrated how energy is transported in a strongly disordered micropolar lattice subject to shear forces and bending moments when the shear stiffness are chosen randomly. The phononic crystal investigated was composed of connected blocks possessing two degrees of freedom corresponding to transverse and rotational motion. The dynamics of the energy density, under different single site initial excitations was characterized into two different regions: a localized energy distribution around the initially excited site and a propagating part at the edges of the lattice. The energy localization for each initial condition as quantified by the participation number P was found to acquire a small (compared to the lattice length) asymptotic value.

Depending on which motion or momentum we initially excited, energy spreading was found to be either superdiffusive or subdiffusive, as quantified by the energy's second moment m_2. Compared to the underlying 1D harmonic case, energy transport is altered, and in general the micropolar lattice featured slower spreading. The modified energy transport characteristics are attributed to the differences of the dispersion relation between the two models in the low frequency limit, to the weight by which the modes of the system are excited depending on the initial condition and also to the existence of additional *quasi-extended* modes in the micropolar lattice.

Furthermore, by measuring the parts of the total energy related to the rotational and transverse motions we showed that the propagating part is always carried by translation for any choice of initial condition. On the other hand, the localized part was found to be either dominated by rotation or translation depending on the initial conditions. Finally, the limiting case of vanishing bending force was found to be similar to a linear 1D KG lattice which exhibits AL and thus no energy spreading.

Our results not only revealed interesting properties of 1D disordered micropolar lattices with bending forces, but also raised new questions for future investigations. A direct generalization of our results is to study the effect of other kinds of disorder i.e., disorder in the masses or in different combinations of the stiffnesses. Furthermore, the appearance of the extended modes at the edge of the upper band is worthy of its own investigation in relation to other known models where anomalous localization appears either due to correlations or symmetry.

Chapter 5

Nonlinear architected structures

Contents

5.1 The highly deformable elastic lattice

This chapter is a natural extension of the studies in Chapter 4 where we will investigate the role of nonlinearity for lattices supporting rotational waves. In a similar manner, as already discussed for granular media, the nonlinearity in highly deformable elastic structures in general is inherent, and usually comes from the geometrical characteristics of the particles constituting the lattice.

More specifically, here we will consider a specific model that was recently introduced [45, 17] to describe architected elastic lattices made with LEGO bricks as shown in Fig. 5.1.

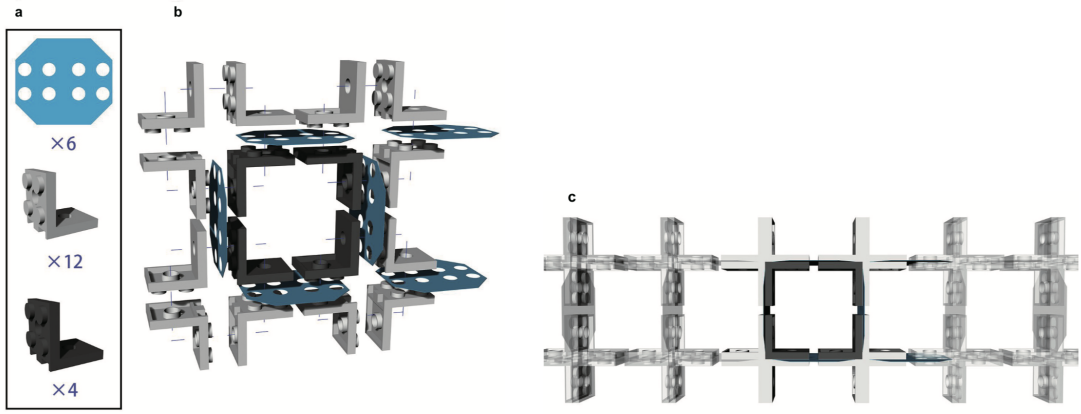

Fig. 5.1. a) The LEGO bricks used for the construction of the lattice. b) View of how the pieces are assembled to construct the unit cell. c) An illustration of how the lattice is formed. Figures are taken from the supplementary material of Ref. [17].

The model was also compared with experimental results and it successfully captures the wave dynamics of the system as well the formation of high amplitude vector solitons. We chose such a model not only because it is experimentally relevant but also due to its specific nonlinearity.

In particular, in this chapter, we establish the coupled nonlinear equations of motion of the lattice, overview the properties of the linear homogeneous case and finally study the spectral properties of the disordered case. It is established that only initial excitations on the rotation are able to couple the two DOFs. Thus, we then excite the lattice with a single site rotation and study the energy spreading as we increase the excitation energy and thus the nonlinearity. The chaoticity of the system is also monitored using the mLE. The system features a unique character resembling the more known FPUT and KG models regarding its asymptotic behavior both in energy spreading and chaoticity.

5.2 The model Hamiltonian and equations of motion

To model the highly deformable elastic lattice of LEGO bricks [102], we consider an array of aligned cross pairs as depicted in Fig. 5.2. In Ref. [17], the authors describe the general equations of motion for a structure that takes into consideration some of the possible geometrical variations of the lattice. However, for the purposes of this work, we limit ourselves to an aligned, symmetrical structure. The crosses are joined to their neighbors by some flexible hinges which are modeled using a combination of three linear springs. The stretching which is captured by a spring with stiffness k_l and the shearing is described by a spring k_s whilst the bending is modeled by a torsional spring k_θ. By making use of the spatial periodicity a, we recast the horizontal deflections u_n at the nth to $U_n = u_n/a$ and change time units to dimensionless time, $T = t\sqrt{k_l/m}$ and the springs are normalized as $K^{(\theta)} = 4k_\theta/k_l a^2$ and $K^{(s)} = k_s/k_l$. The mass of each cross unit m_n, is normalized by the average mass of the crosses, $\overline{m}$. This implies that in the case of the homogeneous chain, $M_n = m_n/\overline{m} = M$ and $\Gamma_n = J/\overline{m}a^2 = \Gamma$. As it was modeled and confirmed by experiments in [45, 17], each pair of crosses is assumed to share the same displacement and rotation, but in opposite directions (i.e., if the top cross rotates by a certain amount in clockwise direction, then the bottom one rotates by the same amount in counter-clockwise direction, and vice versa). As such, two degrees of freedom are assigned to the nth pair of crosses: the longitudinal displacement u_n and the rotation θ_n. The Hamiltonian H, is thus given as (see Ref. [17] for details)

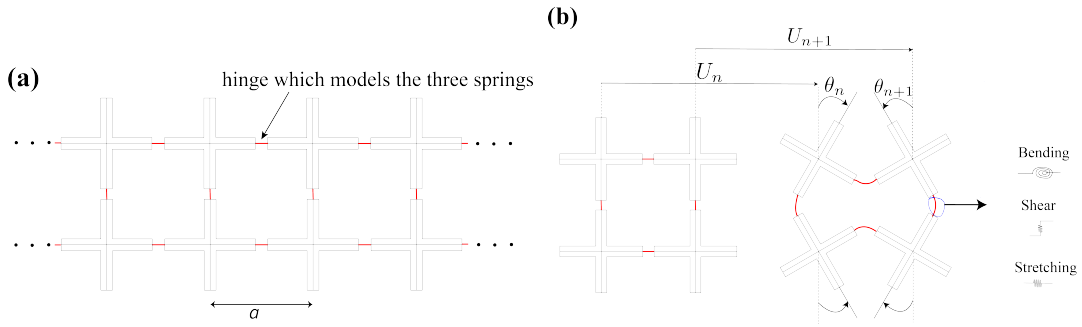

Fig. 5.2. (a) An architected, highly deformable and elastic mechanical structure which supports translational and rotational waves. (b) A schematic of the cross pairs [by symmetry, the dynamics can be described by either the top row or bottom row of (a)] showing the translational and rotational deflections. The connectors (marked in red) model a combination of bending k_θ, shear k_s and stretching springs k_l.

$$H = \sum_{n=1}^{N} \frac{P_n^{(u)^2}}{2M_n} + \frac{P_n^{(\theta)^2}}{2\Gamma_n} + \frac{1}{2}{\Delta_{LH}^n}^2 + \frac{K^{(s)}}{2}{\Delta_{SH}^n}^2 + \frac{K^{(\theta)}}{8}\left({\delta_{\theta H}^n}^2 + \frac{1}{2}{\delta_{\theta V}^n}^2\right), \tag{5.1}$$

where the dimensionless deflections are given by,

$$\Delta^n_{LH} = U_{n+1} - U_n + \frac{1}{2}\left(2 - \cos\theta_n - \cos\theta_{n+1}\right),$$
$$\Delta^n_{SH} = \frac{1}{2}\left(\sin\theta_{n+1} - \sin\theta_n\right),$$
$$\delta^n_{\theta H} = \theta_{n+1} + \theta_n,$$

and

$$\delta^n_{\theta V} = 2\theta_n.$$

Since there are 2 DOFs per cross, the translation momenta are $P^{(u)}_n = M_n\dot{U}_n$ and the corresponding conjugate positions are U_n. For rotational DOFs, the corresponding conjugate momenta and positions are $P^{(\theta)}_n = \Gamma_n\dot{\theta}_n$ and θ respectively. The dimensionless masses and moments of inertia of each cross unit are written as M_n and Γ_n respectively.

We derive the equations of motion from the corresponding Hamilton's equations to yield

$$\begin{aligned} M_n\ddot{U}_n = &\left[U_{n+1} - U_n + \frac{1}{2}\{2 - \cos(\theta_n) - \cos(\theta_{n+1})\}\right] \\ &-\left[U_n - U_{n-1} + \frac{1}{2}\{2 - \cos(\theta_n) - \cos(\theta_{n-1})\}\right], \end{aligned} \tag{5.2}$$

$$\begin{aligned} \Gamma_n\ddot{\theta}_n = &\frac{1}{4}K^{(s)}\cos(\theta_n)\left[\sin(\theta_{n+1}) - \sin(\theta_n)\right] \\ &+\frac{1}{4}K^{(s)}\cos(\theta_n)\left[\sin(\theta_{n-1}) - \sin(\theta_n)\right] \\ &+\frac{1}{4}\sin(\theta_n)\left[2(U_n - U_{n+1}) + \cos(\theta_n) + \cos(\theta_{n+1}) - 2\right] \\ &+\frac{1}{4}\sin(\theta_n)\left[2(U_{n-1} - U_n) + \cos(\theta_n) + \cos(\theta_{n-1}) - 2\right] \\ &-\frac{1}{4}K^{(\theta)}(\theta_{n+1} + 4\theta_n + \theta_{n-1}). \end{aligned} \tag{5.3}$$

5.2.1 The homogeneous linear system

Firstly, let us consider the homogeneous system and linearize the nonlinear terms (trigonometric terms) in Eqs. (5.2) and (5.3) by assuming that θ_{n+p} is small and taking a power series expansion of the appropriate cosine and sine terms to give the first two lowest order terms as

$$\sin\theta_{n+p} \approx \theta_{n+p} - \frac{1}{6}\theta^3_{n+p} + \ldots, \tag{5.4}$$

$$\cos\theta_{n+p} \approx 1 - \frac{1}{2}\theta^2_{n+p} + \ldots. \tag{5.5}$$

In this study, we consider a system where each cross has mass $m = 4.52$ g, spatial periodicity $a = 42$ mm and rotational moment of inertia $J = 605$ g·mm^2. The parameters for the spring constants are $k_l = 71.69$ N·mm^{-1}, $k_s = 1.325$ N·mm^{-1} and

$k_\theta = 4.85$ N·mm. These parameters correspond to those used in Ref. [17]. We change the parameters to dimensionless units as described at the beginning of this section. The linear parts of Eqs. (5.4) and (5.5) are plugged appropriately into Eqs. (5.2) and (5.3) to give the linear equations of motion as

$$M_n \ddot{U}_n = (U_{n+1} - U_n) - (U_n - U_{n-1}), \tag{5.6}$$

and

$$\Gamma_n \ddot{\theta}_n = \tilde{K}\theta_{n+1} + \tilde{K}\theta_{n-1} - 2\tilde{K}\theta_n - 6K^{(\theta)}\theta_n, \tag{5.7}$$

where $\tilde{K} = K^{(s)} - K^{(\theta)}$. For the homogeneous case, $M_n = M$ and $\Gamma_n = \Gamma$ as already defined. A quick glance at Eqs. (5.6) and (5.7) shows that the two DOFs are decoupled in the linear regime. Eq. (5.6) describes the linear FPUT model equations of motion and whilst Eq. (5.7) describes those of the linear KG model. We highlight that this decoupling of the DOFs in the linear regime is valid only for the aligned lattice structure.

We consider solutions of the form,

$$\mathbf{X}_n = \begin{pmatrix} U_n(t) \\ \theta_n(t) \end{pmatrix} = \mathbf{X} e^{i\omega t - iqn}, \tag{5.8}$$

where $\mathbf{X} = [U_0, \Theta_0]$ is the amplitude vector, ω is the cyclic frequency and q is the wave number. Inserting Eq. (5.8) into Eqs. (5.6) and (5.7), we obtain the following eigenvalue problem for the allowed frequencies $\mathbf{DX} = \Omega^2\mathbf{X}$, where the resultant dynamical matrix,

$$\mathbf{D} = \begin{pmatrix} 2 - 2\cos q & 0 \\ 0 & \frac{2}{4\Gamma}[(K^{(s)} + 2K^{(\theta)}) - (K^{(s)} - K^{(\theta)})\cos q] \end{pmatrix}.$$

The corresponding dispersion branch for the transverse DOFs is

$$\omega^{(U)} = \sqrt{2 - 2\cos q}, \tag{5.9}$$

whilst for the rotational DOFs,

$$\omega^{(\theta)} = \frac{1}{\sqrt{4\Gamma}} \sqrt{2(K^{(s)} + 2K^{(\theta)}) - 2(K^{(s)} - K^{(\theta)})\cos q}. \tag{5.10}$$

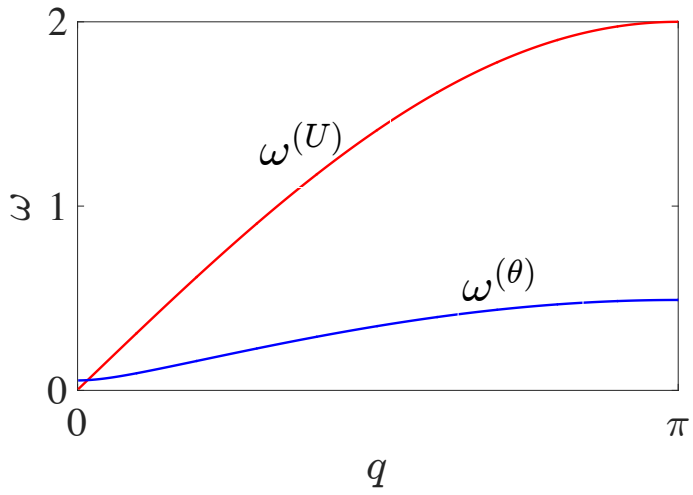

Fig. 5.3. The two dispersion branches of the system for translational ($\omega^{(U)}$) and rotational ($\omega^{(\theta)}$) DOFs.

The dispersion branches of the system's DOFs, as given by Eqs. (5.9) and (5.10) respectively, are plotted in Fig. 5.3. An important feature for the system is that the purely rotational mode branch starts at a finite frequency. This means that linear rotational waves are not supported for $\omega < \frac{1}{\sqrt{4\Gamma}}\sqrt{6K^{(\theta)}}$ because the dispersion relation, Eq. (5.10) has a frequency band gap.

5.2.2 Disordered linear system

We now model the crosses of the structure with disorder in the masses M_n which in turn implies also correlated disorder in rotational moments of inertia Γ_n, for the linear regime, as described by Eqs. (5.6) and (5.7). In a practical sense, disorder to the system can be achieved by changing the material used to manufacture the LEGO bricks [102] without changing the geometrical dimensions. This in turn induces a mass and inertia disorder whilst all the other parameters remain unchanged. In dimensionless units, the masses are normalized to unity for a homogeneous chain hence we take this into consideration in choosing the disorder distribution and take M_n from a uniform probability distribution $f\left(M_n\right)$ where,

$$f\left(M_n\right) = \begin{cases} W^{-1}, & -W/2 < \ M_n - M < W/2, \\ 0 & \text{otherwise.} \end{cases}$$

W denotes the distribution width and for this study, we chose $W = 1.8$ hence $0.1 \leq M_n \leq 1.9$.

To study the dynamical behavior of the system, the equations of motion are integrated using the `ABA864` symplectic integrator [50]. We employ fixed boundary conditions i.e., $U_0 = U_{N+1} = 0$, $\theta_0 = \theta_{N+1} = 0$, $P_0^{(u)} = P_{N+1}^{(u)} = 0$ and $P_0^{(\theta)} = P_{N+1}^{(\theta)} = 0$. This integration scheme allows for energy conservation of the total energy H, and keeps the

relative energy error $\Delta H(T) = \left|\dfrac{H(T) - H(0)}{H(0)}\right| < 10^{-5}$ when the time step $\tau = 0.1$. In all our numerical simulations, the lattice size is large enough so that the energy density profile does not reach the lattice boundaries. A typical numerical integration of the nonlinear system for $T = 10^5$ requires a lattice size of at least 2×10^5. These huge lattice sizes are computationally expensive considering that the variational equations are also integrated at the same time as the equations of motion.

5.2.2.1 Translational DOFs

We start by first exploring the two single site initial excitations of momentum or displacement on the translation DOF i.e.,

$$P^{(u)}_{N/2}(0) = \sqrt{2M_{N/2}H}, \quad U_{\frac{N}{2}}(0) = \nu, \tag{5.11}$$

independently. From Eq. (5.11), the scalar ν is real and its value is altered to match the desired system energy. We fix the total system energy at $H = 10^{-4}$ and integrate the system up to $T = 10^5$ as we observe how the initially localized wave-packet evolve in time. The system had disorder hence we followed the time evolution of the participation number P and the second moment of the energy distribution m_2. The energy density profile with momentum single site initial excitation displays a profile with two main parts, a central localized part, and some peripheral parts which are spreading beyond the excitation point [see Fig. 5.4(a)]. Similar spreading characteristics are observed in the dynamics when the initial condition is displacement as depicted in Fig. 5.4(b).

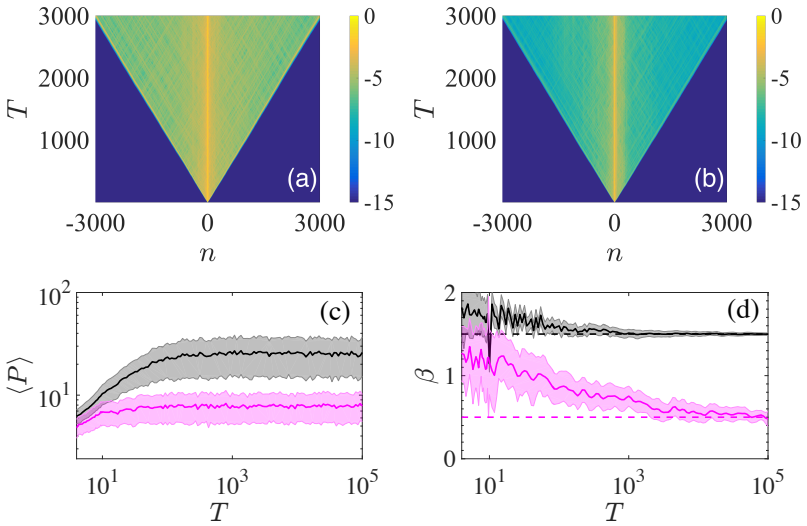

Fig. 5.4. Spatiotemporal evolution of the energy density for a representative realization with (a) momentum and (b) displacement single site initial excitation. The colorbars in (a) and (b) are in log-scale. (c) Mean time evolution of $\langle P \rangle$, (d) estimation of the exponent β, related to the time evolution of the average second moment through $\langle m_2 \rangle \propto T^{\beta}$. The mean values $\langle \cdot \rangle$ are calculated from 100 disorder realizations and the shaded areas represent the statistical error. The dashed lines in (d) indicates $\beta = 1.5$ (top) and $\beta = 0.5$ (bottom) and the system energy for all realizations was $H = 10^{-4}$.

In Fig. 5.4(c), the time evolution of $\langle P \rangle$ reaches a maximum value and remains constant for both momentum (black curves) and displacement (magenta curves). The only difference being that momentum initial excitation yields slightly higher values of $\langle P \rangle$ when compared to the $\langle P \rangle$ reached for displacement initial excitations. This is due to the fact that more low frequency propagating modes are excited for the case of momentum initial excitation than with displacement initial excitation.

The time evolution of β [$\langle m_2 \rangle \propto T^{\beta}$] for the two initial conditions, saturates to $\beta = 1.5$ and $\beta = 0.5$, for momentum and displacement single site excitations respectively in Fig. 5.4(d). This is the expected result for the system since we have already shown the system to be practically a linear disordered harmonic chain (or linear disordered FPUT). It should be clear to the reader that qualitatively similar results are obtained for any excitation as given by Eq. (5.11) as long as the system is aligned. For this reason we shall not consider these DOFs in Section 5.3 since the system always remains linear when translational initial conditions are employed. This is a particularity of the structural geometry under consideration.

5.2.2.2 Rotational DOFs

We now turn our attention and focus on how the dynamics evolve under single site rotational excitations (both momentum and displacement) as given by Eq. 5.12.

$$P^{(\theta)}_{N/2}(0) = \sqrt{2\Gamma_{N/2}H}, \text{ or } \theta_{\frac{N}{2}}(0) = \mu, \tag{5.12}$$

where μ is real and can be altered to match the desired system energy $H = 10^{-4}$. The energy density profiles for both momentum and displacement [see Figs. 5.5(a) and (b)] rotational excitations show localized energy for times $T \geq 10^4$ after an initial phase of wave-packet spreading in contrast to the perpetual wave-packet spreading shown observed for the FPUT model [Figs. 5.4(a) and (b)]. Momentum initial excitations lead to enhanced wave-packet spreading inside the localization volume in comparison to displacement excitations again due to the differences in the initially excited modes of the system.

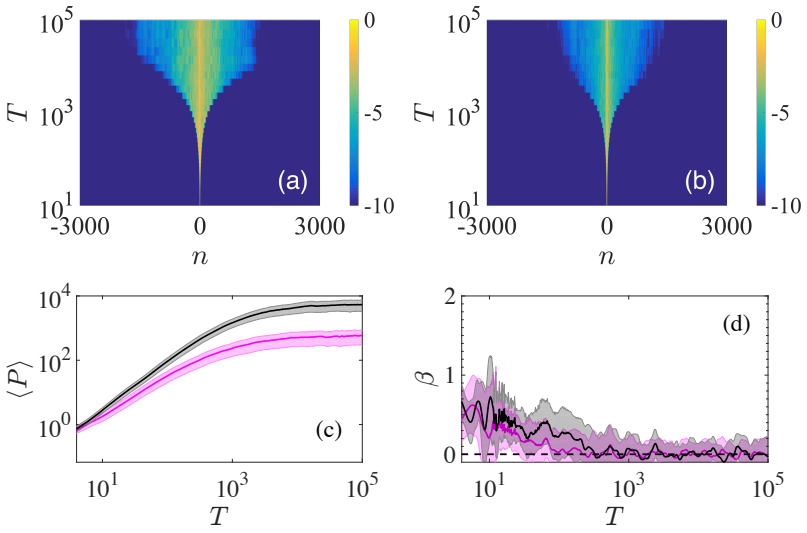

Fig. 5.5. Similar to Fig. 5.4 but for rotational excitations.

The average participation number $\langle P \rangle$ for both the translational and the rotational excitations converge to a finite value [see Fig. 5.5(c)]. However, we can get confirmation of no further energy spreading from the time evolution of $\langle m_2 \rangle$ which saturates to a constant finite value after $T \gtrsim 4 \times 10^3$ as shown by the exponent of $\langle m_2 \rangle$ in Fig. 5.5(d) as expected for a linear disordered KG chain; this exponent, as estimated from the relation $\langle m_2 \rangle \propto T^{\beta}$, scales as $\beta = 0$ [see Fig. 5.5](d)] showing that the LEGO chain behaves as a 1D linear disordered KG chain.

5.3 Disordered nonlinear system

Having considered the behavior of the system in the linear limit, we further study the fully nonlinear system as described by Eqs. (5.2) and (5.3). The system clearly has geometric nonlinearity due to the trigonometric terms (sines and cosines). Before proceeding further, we reiterate that single site initial translational momentum $[P^{(u)}_{N/2}]$ or displacement $[U_{N/2}]$ excitations do not induce a nonlinear response. Furthermore, it must be brought to the attention of the reader that when the rotational DOFs couple the translational DOFs, the coupling is always nonlinear. This is due to the absence of linear terms in the power series expansion of the cosine terms in Eq. (5.2).

5.3.1 Energy transport

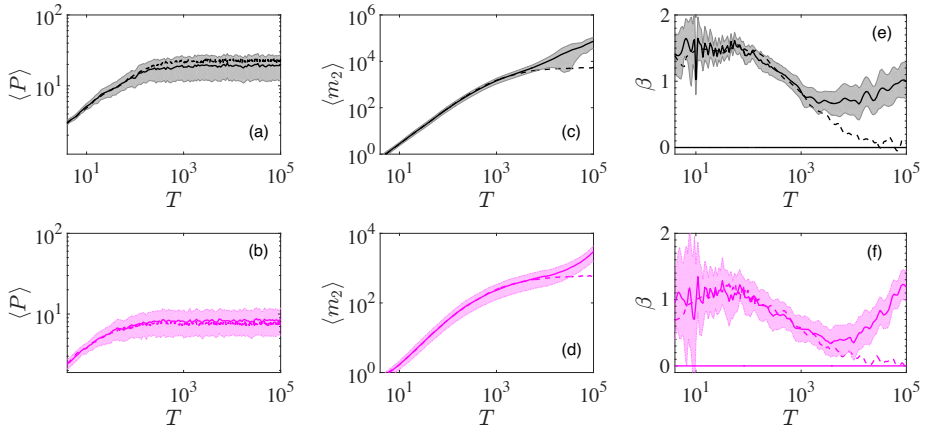

Fig. 5.6. (a) Time evolution of $\langle P \rangle$, (c) $\langle m_2 \rangle$ and (e) β for single site rotational momentum excitations. The corresponding results for single site rotational displacement excitations are shown in (b), (d) and (f). The mean values $\langle \cdot \rangle$ are computed from 100 disorder realizations and the shaded areas represent the statistical error. The dashed lines show results for the linearized equations and the system energy for all realizations was $H = 10^{-8}$. The horizontal lines in (e) and (f) indicate $\beta = 0$.

We start by exciting the rotational degrees of freedom with a sufficiently small energy ($H = 10^{-8}$) so that the system is in the weakly nonlinear regime. We show the results in Fig. 5.6 where the nonlinear effects are clearly playing a significant role for $T \gtrsim 10^3$ even though the system energy is very small. This is highlighted by the comparison with the linear case indicated by the dashed lines in Fig. 5.6. The time evolution of $\langle P \rangle$ after integrating both the nonlinear [Eqs. (5.2) and (5.3)] and the linear [Eqs. (5.6) and (5.7)] equations of motion reaches a constant value. However, the time evolution of $\langle m_2 \rangle$ does not behave in a similar manner. In fact, $\langle m_2 \rangle$ starts to deviate from from the linear behavior for $T \gtrsim 10^3$. Although energy spreading is usually attributed to chaotic behavior, the dynamics is still regular (as we show below).

In Figs. 5.6(a) and (b), the constant values reached during the evolution of the system for both excitations could be anticipated since, even for the uncoupled system, both DOFs reach a finite $\langle P \rangle$. The power law dependence of $\langle m_2 \rangle \propto T^{\beta}$ is further depicted by Figs. 5.6(c) and (d) and the estimation of the exponent of β depicted in Figs. 5.6(e) and (f). Due to nonlinearity, although weak, $T \gtrsim 10^3$, the exponent starts to grow and does not appear to reach a constant value. A similar behavior where β does not acquire an asymptotic value was reported in Ref. [55] for the β-FPUT model. In our case, we may attribute this phenomenon to the combination of FPU-like and KG-like modes which the system supports.

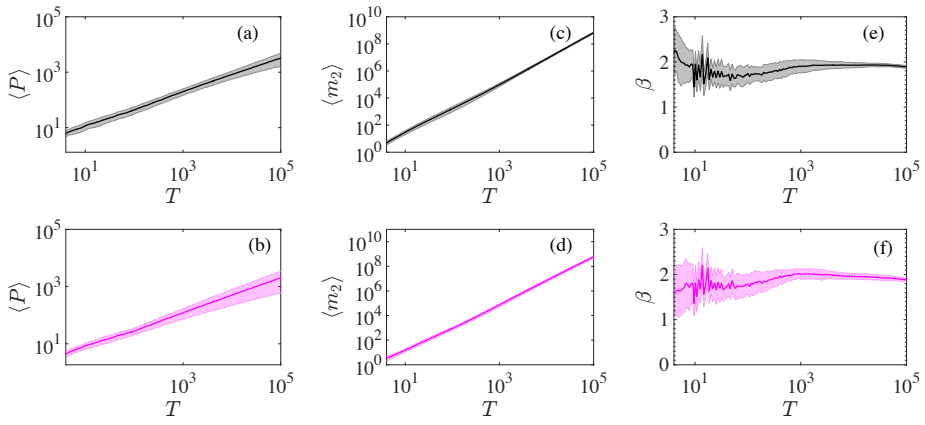

Fig. 5.7. (a)-(f) Similar to Fig. 5.6. The system energy was $H \approx 5.66 \times 10^{-3}$ for all results.

We now consider the disordered system for sufficiently strong nonlinearity at energy $H \approx 5.66 \times 10^{-3}$. In terms of rotations, this is equivalent to a rotation of 30°. At this energy, system's nonlinearity is much stronger to such an extent that the usual underlying signatures of the linear FPUT model already observed in Fig. 5.4(c) and is no longer replicated when one follows the time evolution of $\langle P \rangle$. In Figs. 5.7(a) and (b), $\langle P(T) \rangle$ does not reach a finite value but rather shows a time dependency for both rotational momenta and displacements. Similarly, in Figs. 5.7(c) and (d), the time evolution of $\langle m_2 \rangle$ shows superdiffusive spreading which is almost near ballistic ($\beta \lesssim 2$) as shown by the estimation of the exponent β in Figs. 5.7(e) and (f). We find this result quite interesting since here the nonlinearity is strong enough in order to bring the system to ballistic behavior (in contrast to the FPUT and the KG). In fact the only other example to our knowledge where a ballistic behavior is observed is for the discontinuous nonlinearity of a disordered granular chain [85, 79].

5.3.2 Chaotic behavior of the system

Since the system under study is nonlinear, it is worthwhile to also investigate the chaoticity of the system using one of the most commonly used chaos indicators, the mLE, Λ, which is calculated from the so-called variational equations [103] after utilizing the standard method [58, 59]. The mLE can be used to discriminate between regular and chaotic motions and typically $\Lambda = 0$ for regular orbits and $\Lambda > 0$ for chaotic orbits. The magnitude of the mLE can also be used as a measure of the chaoticity: larger mLE values imply more chaotic behaviors.

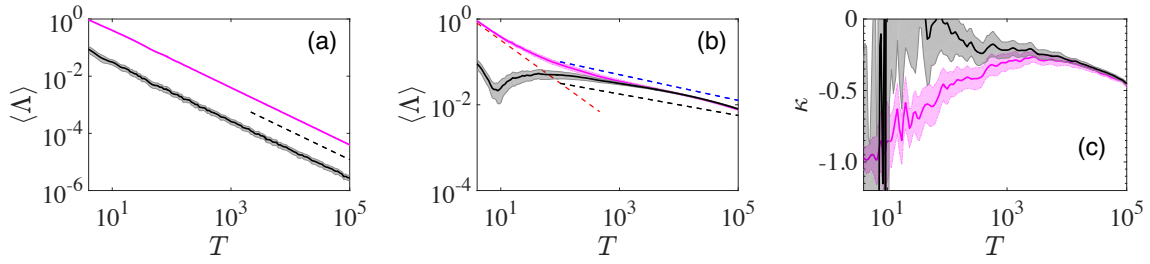

Fig. 5.8. Time evolution of $\langle\Lambda\rangle$ for (a) the near linear regime and (b) nonlinear regime with rotational initial excitations. Time evolution of the exponent κ estimated through the power law $\langle\Lambda\rangle \propto T^{\kappa}$. The system energy was $H = 10^{-8}$ [panel (a)] and $H \approx 5.66 \times 10^{-3}$ [panels (b)-(c)]. The magenta and black curves show results with rotational displacement and momentum respectively.

First we discuss the chaoticity of the system in the weakly nonlinear regime with $H = 10^{-8}$ for the two initial conditions. As depicted in Figs. 5.8(a), the two excitations appear to exhibit regular dynamics in the weakly nonlinear regime for the simulation period, since the mLE follows the power law $\langle\Lambda\rangle \propto T^{-1}$. This signifies that, even though the system is not chaotic, the nonlinearity influences the energy spreading as already shown in Fig. 5.6.

We continue studying the chaotic behavior of the system by increasing the nonlinearity strength and this is achieved by using an energy of $H \approx 5.66 \times 10^{-3}$. In terms of rotations, this is equivalent to a rotation of 30°. At energy $H \approx 5.66 \times 10^{-3}$, the system shows strong nonlinearity which is sufficient to study the chaoticity of the system. The lattice size is kept sufficiently large such that the energy density profile does not reach the ends of the lattice. The curves in Figs. 5.8(b) and (c) show the time evolution of $\langle\Lambda\rangle$ and the exponent κ for the two excitations which in a general sense, show three distinct epochs.

The earliest transient stage is dominated by regular dynamics although this period is very brief. It is more clearer for displacement initial excitations as compared to momentum excitations as shown by how the two curves in Fig. 5.8(b) relate to the red dashed line which shows a slope of -1. After a second transient stage the mLE for both initial conditions converge to a similar behavior for $T \gtrsim 10^3$. In fact, beyond this time the mLE is still going to zero but with a slope different than -1. In particular, for the total time of integration, the exponent of the mLE is found to be $\kappa \approx -0.3$. This value appears to be close to the corresponding asymptotic values for the 1D DNLS equation and the KG model [71, 35]. These slopes are indicated by the blue and black dashed lines in Fig. 5.8(b) corresponding to -0.25 and -0.3. These two numbers indicate a weak and strong chaos behavior respectively.

For the latter systems, it was shown that such a behavior of $\langle\Lambda\rangle$ is due to the fact that the chaoticity of the system decreases due to the energy spreading. This is explained by noting that the portion of chaotic spots in the lattice becomes smaller and smaller

as more degrees of freedom are excited. Consequently, the mLE, which is a global variable, is decreasing to zero.

However although in the aforementioned works the slope of the mLE reached an asymptotic value, this is not the case for our model. In order to test that our model features this decreasing chaotic behavior or it falls back to regular dynamics we need simulations for much longer times.

5.4 Summary and conclusions

In this chapter, we have considered wave propagation and chaotic behavior in a disordered architected mechanical structure. The linear limit of the mechanical structure shows two distinct behaviors corresponding to the FPUT and KG models for the translational and rotational DOFs respectively. For both cases, we recover the well known results regarding the behavior of m_2 under the effect of disorder. We studied the system in two other regimes, namely the weakly nonlinear and strongly nonlinear regimes by choosing the appropriate initial excitation to be in the near linear regime. This is achieved by first being as close as possible to the linear regime and then gradually increasing the energy excitations so as to be more and more nonlinear.

Due to the geometry of the structure, the two degrees of freedom are coupled nonlinearly. Additionally, for this particular model (aligned structure), it is only by initial rotations that the two degrees of freedom can be coupled. As such, we use initial rotations of different amplitudes to study the energy transfer in the presence of disorder. In the weakly nonlinear regime we observe that although the system does not exhibition chaos, the energy transfer different from the linear case due to nonlinearity. In fact, the evolution of the second energy moment shows non saturated behavior and its exponent is varying. However, in the strongly nonlinear case, the system exhibits a quite fast (almost ballistic) energy spreading. Regarding chaoticity, although the results show no clear asymptotic behavior, the corresponding mLE signals a gradually decreasing chaos similar to what is found in other nonlinear disorder lattices.

Chapter 6
General Conclusions

In this thesis, we have studied and reported how elastic waves propagate in disordered 1D granular chains and related phononic crystals as well as in flexible architected structures from a theoretical and numerical point of view. For these structures we considered disorder in either the masses or the spring coupling constants. These structures present an opportunity to study rich wave dynamics due to several aspects such as the presence of several degrees of freedom per lattice site, the tunability of the nonlinearity and the possibility to incorporate disorder. This work is devoted to the study of elastic wave propagation through heterogeneous structures by first modeling the corresponding physical system, studying the homogeneous case and then adding to complexity by considering disorder and nonlinearity.

The wave dynamics of the structures can be tuned by a specific parameter such as, the pre-compression force in the case of granular chains. For the phononic crystal, the shear stiffness is utilized as the tuning parameter whilst in the case of the architected deformable structures, the physical geometry of the structure was utilized to alter the dispersion relation. In the case of the 1D disordered granular chain, by changing the initial energy excitation from sufficiently small to sufficiently high values, we were able to traverse from the weakly nonlinear regime to the strongly nonlinear regime for a fixed pre-compression force. The granular chain which is nonlinear also presents an opportunity to study the chaotic behavior of the system. By tuning the phononic structure in a similar manner as what is done with granular crystals, the system is able to support transversal/rotational propagation modes, zero energy modes and different wave propagation characteristics for single site initial conditions. Similarly, the deformable architected structure, can be tuned to reveal diverse dispersion characteristics such as coupled translational/rotational modes or completely decoupled modes.

For 1D disordered granular crystals, we showed the evolution of an initially localized mode to be categorized into three stages as we excite the mode with increasing amplitude. For the first stage, the mode remains localized with no chaotic behavior, the second stage involves localized but chaotic dynamics whilst the final stage involves delocalization of the mode, chaotic behavior and energy equipartition. We also established that the discontinuous nonlinearity in the case of the granular chain greatly aids energy equipartition. The results of the linear disordered phononic micropolar lattice showed excitation dependent asymptotic wave propagation characteristics. In

fact, the phononic crystal showed both superdiffussive and subdiffusive wave-packet spreading depending on the initial single site excitation. We also attributed some of the wave propagation characteristics to spatially extended modes close to the band gap (*quasi-extended modes*). The energy spreading for the phononic lattice consists of a propagating part (at the leading front of the wave-packet) and a localized part (around the excitation point). The propagating part was found to be dominated by transversal motions for any choice of initial condition. Conversely, for the localized part, it is found to be either dominated by rotational or transversal motion depending on the initial conditions. To illustrate the tunability of the system, the limiting case of vanishing bending force is found to be similar to a linear 1D KG lattice which exhibits AL and thus no energy spreading.

The linear limit of the aligned 1D flexible and deformable structure made of LEGO bricks revealed two distinct dynamical behaviors. The system resembles an FPUT-like lattice for translations and a KG-like lattice for rotations. In fact, in the linear limit, the two motions are decoupled. By using rotations as initial conditions, we are able to excite both degrees of freedom and also see nonlinear phenomena. In fact, a weakly nonlinear regime is identified where the system is not chaotic but exhibits nonlinearity induced energy spreading. This spreading does not saturate to an asymptotic power law. On the other hand, in the strongly nonlinear limit, an almost ballistic energy transport is achieved even though the system presents a quite unique chaotic behavior different from the DNLS and the KG models.

In this thesis we have found that disordered elastic lattices offer new insights regarding the interplay between disorder and nonlinearity. Following our results on the energy equipartition in finite disorder granular lattices, we believe that more detailed investigation is essential towards understanding the observed phenomena. A natural question arising is why the Hertzian model's nonlinearity is able to mix the linear modes much more efficiently than the FPUT model? In general, the idea of ergodicity breaking in nonlinear systems is still an open question. Also one could ask if is possible to observe such equipartition experimentally? Of course such a task is difficult most probably due to the presence of losses, thus further investigation is needed to study equipartition in the presence of losses.

In the same spirit, equipartition of finite polarized nonlinear lattices (e.g., which include rotations) opens another interesting direction. In particular one could try to find out if by tuning the coupling between the degrees of freedom the timescales to energy equipartition can be altered and controlled? In fact, Following a plethora of different architected lattices that have been built over the years, many different models can be sought in this direction (e.g., origami inspired structures).

A quite different direction that arises by the results of this thesis is based on the importance of the rotational waves coupled with the translations. In particular, of great interest is the study of compact flat bands and their corresponding compact modes. Such modes are able to localize energy (as Anderson modes) but they appear

to be very robust under disorder. They offer a great tool of energy storage which is not sensitive to perturbations. One could first design elastic lattices in known geometries that support flat bands. Thereafter, aiming for more realistic description, the study of the effect of additional degrees of freedom (e.g., rotation) maybe be investigated. If (or when) flat bands persists under such more realistic descriptions, this will bring the use of flat bands one step closer towards applications.

Bibliography

[1] P.W. Anderson, Phys. Rev. **109**, 1492 (1958).

[2] B. Kramer and A. MacKinnon, Rep. Prog. Phys. **56**, 1469 (1993).

[3] F. Evers and A.D. Mirlin, Rev. Mod. Phys. **80**, 1355 (2008).

[4] L. Sanchez-Palencia, and M. Lewenstein, Nat. Phys. **6**, 87 (2010).

[5] V.A. Hopkins, L.C. Krysac, and J.D. Maynard, Phys. Rev. B **58**, 11377 (1998).

[6] S.A. Gredeskul and Y.S. Kivshar, Phys. Rep. **216**, 1 (1992).

[7] R. Knapp, G. Papanicolaou, and B. White, Lect. Notes Math. **2146** (1989).

[8] M. Sayar, M.C. Demirel, and A.R. Atilgan, J. Sound Vib. **205**, 372 (1997).

[9] R. Knapp, G. Papanicolaou, and B. White, J. Stat. Phys. **63**, 567 (1991).

[10] P. Devillard, F. Dunlop, and B. Souillard, J. Fluid Mech. **186**, 521 (1988).

[11] M.J. McKenna, R.L. Stanley, and J.D. Maynard, Phys. Rev. Lett. **69**, 1807 (1992).

[12] M.J. McKenna, J. Keat, J. Wang, and J.D. Maynard, Physica B **194**, 1039 (1994).

[13] V.A. Hopkins, J. Keat, G.D. Meegan, T. Zhang, and J.D. Maynard, Phys. Rev. Lett. **76**, 1102 (1996).

[14] Y. Lahini, A. Avidan, F. Pozzi, M. Sorel, R. Morandotti, D.N. Christodoulides, and Y. Sidelberg, Phys. Rev. Lett. **100**, 013906 (2008).

[15] D.L Shepelyansky, Phys. Rev. Lett. **70**, 1787 (1993).

[16] F. Allein, V. Tournat, V. Gusev, and G. Theocharis, Phys. Rev. Appl. **13**, 024023 (2020).

[17] B. Deng, P. Wang, Q. He, V. Tournat, and K. Bertoldi, Nat. Comm. **9**, 1 (2018).

[18] D.S. Wiersma, P. Bartolini, A. Lagendijk, and R. Righini, Nature (London) **390**, 671 (1997).

[19] T. Schwartz, G. Bartal, S. Fishman, and M. Segev, Nature (London) **446**, 52 (2007).

[20] C. Fort, L. Fallani, V. Guarrerra, J.E. Lye, M. Modugno, D.S. Wiersma, and M. Inguscio, Phys. Rev. Lett. **95**, 170410 (2005).

[21] D. Clément, A.F. Varon, M. Hugbart, J.A. Retter, P. Bouyer, L. Sanchez-Palencia, D.M. Gangardt, G.V. Shlyapnikov, and A. Aspect, Phys. Rev. Lett. **95**, 170409 (2005).

[22] J. Billy, V. Josse, Z. Zuo, A. Bernard, B. Hambrecht, P. Lugan, D. Clément, L. Sanchez-Palencia, P. Bouyer, and A. Aspect, Nature (London) **453**, 891 (2008).

[23] G. Roati, C. D'Errico, L. Fallani, M. Fattori, C. Fort, M. Zaccanti, G. Modugno, M. Modugno, and M. Inguscio, Nature (London) **453**, 895 (2008).

[24] S.S. Kondov, W.R. McGehee, J.J. Zirbel, and B. DeMarco, Science **334**, 66 (2011).

[25] F. Jendrzejewski, A. Bernard, K. Mueller, P. Cheinet, V. Jose, M. Piraud, L. Pezzé, L. Sanchez-Palencia, and A. Aspect, Nat. Phys. **8**, 398 (2012).

[26] H. Hu, A. Strybulevych, J.H. Page, S. Skipetrov, and B.A. van Tiggelen, Nat. Phys. **4**, 945 (2008).

[27] M. Filoche and S. Mayboroda, Proc. Natl. Acad. Sci. **109**, 14761 (2012).

[28] E. Fermi, J. Pasta, and S. Ulam, *Los Alamos report* LA-1940 (1955).

[29] M. Onorato, L. Vozella, D. Proment, and Y.V. Lvov, Proc. Natl. Acad. Sci. **112**, 4208 (2015).

[30] A.S. Pikovsky, and D.L. Shepelyansky, Phys. Rev. Lett. **100**, 094101 (2008).

[31] G. Kopidakis, S. Komineas, S. Flach, and S. Aubry, Phys. Rev. Lett. **100**, 084103 (2008).

[32] Ch. Skokos, D.O. Krimer, S. Komeneas, and S. Flach, Phys. Rev. E **79**, 056211 (2009).

[33] S. Flach, D.O. Krimer, and Ch. Skokos, Phys. Rev. E **102**, 024101 (2009).

[34] Ch. Skokos, I. Gkolias, and S. Flach, Phys. Rev. Lett. **111**, 064101 (2013).

[35] B. Senyange, B. Many Manda, and Ch. Skokos, Phys. Rev. E **98**, 052229 (2018).

[36] I. Vakulchyk, M.V. Fistul, and S. Flach, Phys. Rev. Lett. **122**, 040501 (2019).

[37] E. Kim, A.J. Martínez, S.E. Phenisee, P.G. Kevrekidis, M.A. Porter, and J. Yang, Nat. Comm. **9**, 1 (2018).

[38] K. Sun, A. Souslov, X. Mao, and T.C. Lubensky, Proc. Natl. Acad. Sci. **109**, 12369 (2012).

[39] C.L. Kane and T.C. Lubensky, Nature Phys. **10**, 39 (2014).

[40] J. Paulose, B.G. Chen, and V. Vitelli, Nature Phys. **11**, 153 (2015).

[41] P. Wang, L. Lu, and K. Bertoldi, Phys. Rev. Lett. **115**, 104302 (2015).

[42] F. Allein, V. Tournat, V.E. Gusev, and G. Theocharis, Extr. Mech. Lett. **12**, 65 (2017).

[43] F. Allein, Phd thesis, Le Mans Université, 2017.

[44] P. Wang, F. Casadei, S. Shan, J.C. Weaver, and K. Bertoldi, Phys. Rev. Lett. **113**, 014301 (2014).

[45] B. Deng, J.R. Raney, V. Tournat, and K. Bertoldi, Phys. Rev. Lett. **118**, 2014102 (2017).

[46] E. Hairer, C. Lubich, and G. Wanner, *Geometric Numerical Integration* (Springer, New York, 2002), Vol. 31.

[47] C. Runge, Math. Ann. **46**, 167 (1895).

[48] W. Kutta, Z. Math. Phys. **46**, 435 (1901).

[49] H. Yoshida, Phys. Lett. A **150**, 262 (1990).

[50] S. Blanes, F. Casas, A. Farrés, J. Laskar, J. Makazaga, and A. Murua, Appl. Numer. Math. **68**, 58 (2013).

[51] B. Senyange and Ch. Skokos, Europhys. J. Spec. Top. **227**, 625 (2018).

[52] C. Danieli, B. Many Manda, T. Mithun, and Ch. Skokos, Math. Eng. **1**, 447 (2019).

[53] S. Flach, Lect. Notes Math. **2146**, 1 (2015).

[54] P.K. Datta and K. Kundu, Phys. Rev. B **51**, 6287 (1995).

[55] S. Lepri, R. Schilling, and S. Aubry, Phys. Rev. E **82**, 056602 (2010).

[56] W.S. Cleveland and S.J. Devlin, J. Am. Stat. Assoc. **83**, 596 (1988).

[57] W.S. Cleveland, J. Am. Stat. Assoc. **74**, 829 (1979).

[58] G. Benettin, G. Galgani, A. Giorgilli, and J.-M. Strelcyn, Meccanica **15**, 21 (1980).

[59] Ch. Skokos, Lect. Notes Phys. **790**, 63 (2010).

[60] Ch. Skokos and E. Gerlach, Phys. Rev. E **82**, 036704 (2010).

[61] E. Gerlach and Ch. Skokos, Discrete Cont. Dyn. Syst. Supp. **2011**, 475 (2011).

[62] E. Gerlach, S. Eggl, and Ch. Skokos, Int. J. Bifurcat. Chaos **22**, 1250216 (2012).

[63] K.R. Allen and J. Ford, Phys. Rev. **176**, 1046 (1968).

[64] R.J. Rubin and W.L. Greer, J. Math. Phys. **12**, 1686 (1971).

[65] P. Dutta and S.K. Sinha, Phys. Rev. Lett. **47**, 50 (1981).

[66] M.B. Plenio, J. Eisert, J. Dreissig, and M. Cramer, Phys. Rev. Lett. **94**, 060503 (2005).

[67] P.L. Christiansen, Y.B. Gaididei, M. Johansson, and K.Ø. Rasmussen, Phys. Rev. B **55**, 5759 (1997).

[68] L.J. Maczewsky, K. Wang, A.A. Dovgiy, A.E. Miroshnichenko, A. Moroz, M. Ehrhardt, M. Heinrich, D.N. Christodoulides, A. Szameit, and A.A. Sukhorukov, Nature Photonics. **14**, 76 (2020).

[69] L. Vázquez, L. Streit, and V.M. Pérez-García, *Nonlinear Klein-Gordon and Schrödinger Systems: Theory and Applications* (World Scientific, New York, 1996).

[70] P.G. Kevrekidis, K.Ø. Rasmussen, and A.R. Bishop, Int. J. Mod. Phys. B **15**, 2833 (2001).

[71] B. Many Manda, B. Senyange, and Ch. Skokos, Phys. Rev. E **101**, 032206 (2020).

[72] T. Horota, and K. Ishii, Prog. Theor. Phys. Supp. **53**, 77 (1973).

[73] K. Ishii, Prog. Theo. Phys. **45**, 1713 (1971).

[74] Y.S. Kivshar, and M. Peyrard, Phys. Rev. A **46**, 3198 (1992).

[75] Y.S. Kivshar, Phys. Rev. E **48**, 4132 (1993).

[76] M. Johansson, Physica D **216**, 62 (2006).

[77] D.J. Thouless, Phys. Rep. **13**, 93 (1974).

[78] M.V. Ivanchenko, T.V. Laptyeva, and S. Flach, Phys. Rev. B **89**, 060301 (2014).

[79] A.J. Martínez, P.G. Kevrekidis, and M.A. Porter, Phys. Rev. E **93**, 022902 (2016).

[80] I. García-Mata and D.L. Shepelyansky, Phys. Rev. E **79**, 026205 (2009).

[81] M.I. Molina, Phys. Rev. B **58**, 12547 (1998).

[82] E. Lucioni, B. Deissler, L. Tanzi, G. Roati, M. Zaccanti, M. Modugno, M. Larcher, F. Dalfovo, M. Inguscio, and G. Modugno, Phys. Rev. Lett. **106**, 230403 (2011).

[83] A. Ngapasare, G. Theocharis, O. Richoux, Ch. Skokos and V. Achilleos Phys. Rev. E **99**, 032211 (2019).

[84] K.L. Johnson, *Contact Mechanics* (Cambridge University Press, Cambridge, 1985).

[85] V. Achilleos, G. Theocharis, and Ch. Skokos, Phys. Rev. E **93**, 022903 (2016).

[86] G. Theocharis, N. Boechler, and C. Daraio, Nonlinear Periodic Phononic Structures and Granular Crystals, *Acoustic Metamaterials and Phononic Crystals* (Springer Berlin Heidelberg, 2013), pp. 217-251.

[87] M. Hillebrand, G. Kalosakas, A. Schwellnus, and Ch. Skokos, Phys. Rev. E **99**, 022213 (2019).

[88] R. Livi, M. Pettini, S. Ruffo, M. Sparpaglione, and A. Vulpiani, Phys. Rev. A **31**, 1039 (1985).

[89] C.G. Goedde, A.J. Lichtenberg, and M.A. Lieberman, Physica D **59**, 200 (1992).

[90] C. Danieli, D.K. Campbell, and S. Flach, Phys. Rev. E **95**, 060202 (2017).

[91] A. Ngapasare, G. Theocharis, O. Richoux, Ch. Skokos and V. Achilleos, Phys. Rev. B **102**, 054201 (2020).

[92] H-Y. Xie, V.E. Kravtsov, and M. Müller, Phys. Rev. B **86**, 014205 (2012).

[93] X. Yu, and S. Flach, Phys. Rev. E **90**, 032910 (2014).

[94] H. Pichard, A. Duclos, J-P. Groby, V. Tournat and V.E. Gusev, Phys. Rev. E **89**, 013201 (2014).

[95] H. Yasuda, T Tachi, M. Lee, and J. Yang, Nat. Comm. **8**, 1 (2017).

[96] C.L. Randow, G.L. Gray, and F. Constanzo, Int. J. Solids Struct. **43**, 1253 (2006).

[97] A.K. Noor, Appl. Mech. Rev. **41**, 285 (1988).

[98] P.A. Deymier, K. Runge, N. Swinteck, and K. Muralidharan, C. R. Méc. **343**, 700 (2015).

[99] A.S.J. Suiker, A.V. Metrikine, and R. De Borst, Int. J. Solids Struct. **38**, 1563 (2001).

[100] M. Wagner, G. Zavt, J. Vazquez-Marquez, A. Lütze, Th. Mougios, G. Viliani, W. Frizzera, O. Pilla, and M. Montagna, Philos. Mag. B **65**, 273 (1992).

[101] P.L. Krapivsky and J.M. Luck, J. Stat. Mech. **2011**, P02031 (2011).

[102] P. Celli and S. Gonella, Appl. Phys. Lett. **107**, 081901 (2015).

[103] G. Contopoulos, L. Galgani, and A. Giorgilli, Phys. Rev. A **18**, 1183 (1978).

List of publications

Articles in international peer-reviewed journals

- A. Ngapasare, G. Theocharis, O. Richoux, Ch. Skokos and V. Achilleos. Chaos and Anderson localization in disordered classical chains : Hertzian versus Fermi-Pasta-Ulam-Tsingou models, Phys. Rev. E, **99** 032211 (2019).

- A. Ngapasare, G. Theocharis, O. Richoux, Ch. Skokos and V. Achilleos. Wave propagation in a strongly disordered 1D phononic lattice supporting rotational waves, Phys. Rev. B, **99** 032211 (2020).

- A. Ngapasare, G. Theocharis, O. Richoux, Ch. Skokos and V. Achilleos. Nonlinear rotational waves in architected structures, In Preparation.

DOCTORAT BRETAGNE SCIENCES LOIRE POUR L'INGENIEUR

Le Mans Université

Titre : Ondes mécaniques dans les structures désordonnées et non linéaires

Mot clés : Onde non linéaire, Réseau non linéaire, Localisation de Anderson, Structures mécaniques désordonnées, Chaos, Diffusion de l'energie

Résumé : Ce travail est consacré à l'étude théorique et numérique de la propagation des ondes élastiques dans les structures mécaniques désordonnées. L'objectif principal est d'étudier comment la localisation induite par le désordre est affectée par la non-linéarité et par la présence de mouvements de rotations. Nous étudions d'abord une chaîne granulaire finie et montrons que non seulement la localisation d'Anderson est rompue mais aussi que l'équipartition de l'énergie est réalisée grâce à la non-linéarité discontinue propre aux chaînes granulaires. De plus, nous étendons nos études à un réseau micropolaire qui supporte les ondes de rotation. Nous montrons que, dans la limite linéaire, la répartition de l'énergie est facilitée à la fois par des ondes étendues à basse fréquence et par un ensemble de modes quasi-étendus à haute fréquence. Nous identifions aussi un cas où l'énergie est complètement localisée en réglant la rigidité. Enfin, pour une chaîne LEGO architecturée non linéaire présentant un mouvement à la fois transversal et rotatif, nous étudions comment la non-linéarité rompt, dans ce système polarisé, la localisation d'Anderson. Il s'avère que la dynamique de ce système a un caractère unique qui ressemble à une combinaison des modèles Fermi-Pasta-Ulam-Tsingou et Klein-Gordon pour le comportement asymptotique et chaotique.

Title: Waves in disordered and nonlinear structures

Keywords: Nonlinear wave, Nonlinear lattice, Anderson localization, Mechanical disordered structures, Chaos, Energy spreading

Abstract: This work is devoted to the theoretical and numerical study of elastic wave propagation in disordered mechanical structures. The main goal is to investigate how the localization induced by disorder is affected by nonlinearity and by the presence of rotational motion. First we study a finite granular chain and show that not only Anderson localization is broken but also energy equipartition is achieved due to the discontinuous nonlinearity which is particular to granular chains. Furthermore, we extend our studies to a micropolar lattice that supports rotational waves. We show that in the linear limit the energy spreading is facilitated both by low frequency extended waves and a set of high frequency quasiextended modes. Also, we identify a case where energy is completely localized by tuning the stiffness. Finally, for a nonlinear architected LEGO chain featuring both transverse and rotational motion we study how nonlinearity breaks Anderson localization in this polarized system. The dynamics is found to have a unique character resembling a combination of the Fermi-Pasta-Ulam-Tsingou and Klein-Gordon models regarding the asymptotic dynamical behavior and chaoticity.